Two-Dimensional Bernstein-Greene-Kruskal Modes in a Magnetized Plasma with Kinetic Effects from Electrons and Ions

By

Han Tang, B.S.

A Thesis Submitted in Partial Fulfillment of the Requirements

for the Degree of

Master of Science

in

Physics

University of Alaska Fairbanks

May 2020

APPROVED:

Dr. Chung-Sang Ng, Committee Chair
Dr. Peter Delamere, Committee Member
Dr. David Newman, Committee Member
Dr. Renate Wackerbauer, Chair
Department of Physics
Dr. Kinchel C. Doerner, Dean
College of Natural Science & Mathematics
Dr. Michael Castellini,
Dean of the Graduate School

Abstract

Electrostatic structures are observed in various of space environments including the auroal acceleration region, the solar wind region and the magnetosphere. The Bernstein-Greene-Kruskal (BGK) mode, one of the non-linear solutions to the Vlasov-Poisson system, is a potential explanation to these phenomena. Specifically, two dimensional (2D) BGK modes can be constructed through solving the Vlasov-Poisson-Ampère system with the assumption of a uniform ion background. This thesis discusses the existence and features of the 2D BGK modes with kinetic effects from both electrons and ions. Specifically, we construct electron or ion BGK modes with finite temperature ratio between ions and electrons. More general cases, the electron-ion 2D BGK mode with the participation of both non-Boltzmann electron and ion distributions are constructed and analyzed as well.

Contents

List of Figures

Chapter 1

Introduction

The original BGK mode is a class of one dimensional (1D) nonlinear steady-state solutions of the Vlasov-Poisson equations [Bernstein et al., 1957]. Since the BGK mode was first mentioned in 1957, there have been many studies about the 1D BGK mode [Hutchinson, 2017]. Other wave modes, for example, the Van Kampen modes [Van Kampen, 1955] can be seen as the small amplitude approximation of BGK modes [Gurnett and Bhattacharjee, 2017]. Generally speaking, the 1D BGK mode can be constructed with two different approaches, through specifying the expression of the distribution function or the electric potential of the system. Afterwards, a differential equation will be constructed and by solving the differential equation, important properties such as number densities, electric potentials, and distribution functions that reveals the physical picture of the system can be derived. This scenario is introduced in certain textbooks [Gurnett and Bhattacharjee, 2017, Nicholson, 1983, Swanson, 2003].

Three dimensional features of plasma solitary waves observed in space that cannot be explained by the 1D BGK mode become one of the main motivations to study BGK modes in higher dimensions [Cattell et al., 1999, Ergun et al., 1998, Franz et al., 1998, Franz et al., 2005]. For example, the electrostatic solitary waves occured in the auroral ionosphere discussed in [Ergun et al., 1998] possesses electric field component perpendicular to the background magnetic field. The strength of the perpendicular component is comparable with that of the parallel component. The electric field in a 1D BGK mode has the parallel component only, thus the

observation cannot be interpreted by the 1D BGK mode. Simulation results also suggests BGK modes that exist in higher dimensions [Oppenheim et al., 1999, Singh, 2000, Singh et al., 2000].

Many solutions of 2D and 3D BGK modes have been found. With strong background magnetic field, the charged particles are constrained to move along the magnetic field, and thereby the 3D BGK mode constructed based on this assumption reduces to a 1D BGK problem [Chen, 2002, Chen and Parks, 2002]. It is proved that a distribution function depending only on the energy, i.e. of the form $f = f(E)$, where $E = mv^2/2 - e\phi$ is the energy, cannot be a solution of a 2D or 3D BGK mode that is localized (electric field tends to zero far away from the center) [Ng and Bhattacharjee, 2005]. Thus, to illustrate the exact 2D/3D BGK mode, the distribution function has to depend on other physical properties. For instance, 3D BGK modes in a localized spherically symmetric potential for an unmagnetized plasma can exist with a distribution function that depends on energy and angular monetum [Ng and Bhattacharjee, 2005]. With finite magnetic field, cylindrical symmetric 2D BGK modes can also be constructed [Ng et al., 2006, Ng, 2020]. The distribution function under such a case is related to the energy and the canonical angular momentum.

Specifically, [Ng, 2020] demonstrated that electrostatic structures of kinetic flux ropes can be constructed through the 2D BGK modes. An example of kinetic flux rope is shown in Figure 1.1. This construction is noticeably signifcant as electrostatic structures are observed in various regions of space plasma and the kinetic flux rope can be a potential explanation to those phenomena. The construction of the 2D BGK mode starts from assuming the velocity distribution function as a function of the total energy, the $\hat{z}$-component of the canonical angular momentum, and the $\hat{z}$-component of the canonical momentum. Three equations, the Vlasov Equation, the Poisson's Equation and the Ampère's Law are used to develop the 2D BGK modes. With the presence of a finite magnetic field, three coupled non-linear ordinary differential equations with respect to the electric potential, the vertical component of the vector potential, and the tangential component of the vector potential are derived. The simulation results presented proves that the flux rope solutions can be solved through a kinetic perspective, which is very different from flux rope solutions found in magnetohydrodynam-

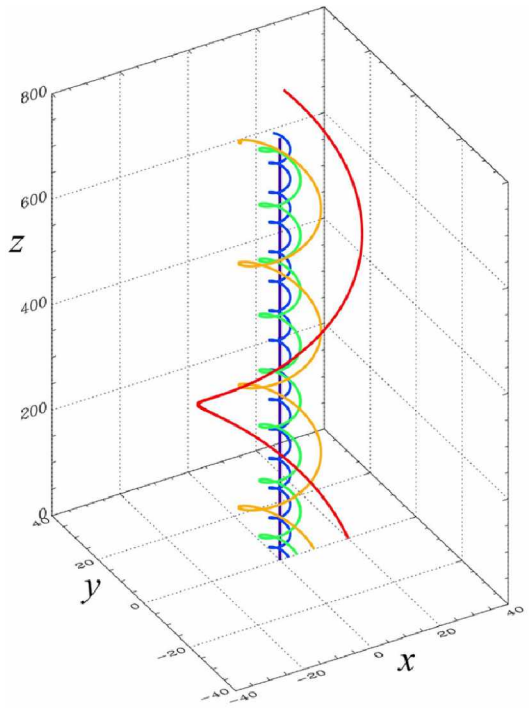

Figure 1.1: An example of kinetic flux ropes constructed by the electron 2D BGK mode. Five magnetic field lines drawn in different colors, going through y = z = 0, x = 0, 2.5, 5, 10, 20 d_e , which is 200 λ_D. The parameters and initial values used in the electron 2D BGK mode are $h = 0.99$, $k = 1 \times 10^{-5}$, $\xi = 1$, $\beta_e = 0.005$, $A_{z0} = 1$, and $B_{z0} = 0.00293$ [Ng, 2020].

ics. Note that small scale kinetic structures in the magnetosphere have been observed by the Magnetospheric Multiscal Mission (MMS) [Balikhin et al., 2012, Fu et al., 2012, Ge et al., 2011, Gershman et al., 2016, Goodrich et al., 2016, Ji et al., 2014, Sun et al., 2012, Sundberg et al., 2015, Zhima et al., 2015]. Also, non-Maxwellian particle distributions are observed in collisionless plasmas [Leubner, 2004, Livadiotis and McComas, 2009, Vasyliunas, 1968] 2D BGK modes might be part of the reasons behind those phenomena.

Despite the discoveries made in [Ng, 2020], several topics remains unexplored. Solutions to the flux ropes were only found based on the assumption of a uniform ion density. One situation that justifies such an assumption is when the temperature ratio between ions and electrons is very large. However, whether the solution will exist universally under different temperature ratios, and how the solution will change remain important questions to be answered. Moreover, the case where the ion velocity distribution is non-Boltzmann and the electron velocity distribution is Boltzmann has not been studied. Furthermore, how to construct solutions when both electron

and ion distributions are non-Boltzmann has not been demonstrated either. These ideas are the motivations of this thesis.

This thesis contains five major parts. Chapter one introduces the background and history of the 1D BGK mode, and the motivations of studying the 2D BGK mode. The second chapter starts from the Vlasov-Poisson-Ampère system and derives the three coupled second order non-linear differential equations. Also, important physical properties like number densities, bulk velocities, current densities, and temperatures of electrons and ions are shown in chapter two. The third chapter explains initial and boundary conditions of the ordinary differential equations derived in chapter two. With the boundary conditions deduced, a 2D BGK simulator based on the adaptive stepsize Runge Kutta method is also presented in this chapter. Simulation results and analysis of three different cases, the electron BGK mode, the ion BGK mode, and the electron-ion BGK mode that answer the motivations mentioned in the previous paragraph are given in chapter four. Conclusions and summaries are given in chapter five. Details of derivations that are not covered in chapter two can be found in the Appendix.

Chapter 2

Basic Theory

In this chapter, we discuss the basic theory on constructing 2D BGK mode solutions in a magnetized plasma. The velocity distribution functions for ions and electrons are assumed to satisfy the Vlasov Equation. The normalization and the coordinate system used are introduced in Sections 2.1 and 2.2. The details of velocity distribution functions and the physical meanings of all the parameters are introduced in Section 2.3. Number densities are calculated from integrating velocity distribution functions with respect to velocities, and the first differential equation of the system could be constructed by substituting ion and electron number densities into the Poisson Equation. These processes are explained in Section 2.4. In Section 2.5, velocity distribution functions and the Ampère's Law are used to generate the second and third differential equations. In the last section, Section 2.6, two significant physical properties, bulk velocities and temperatures of particles, are computed through calculating the 1^{st} and the 2^{nd} moments of the velocity distribution functions.

2.1 Basic Setup and Nondimensionalization

Fundamental equations, the Vlasov equation, which is also referred to as "the Collisonless Boltzmann equation", and the Poisson equation, which describes the electric potential field generated by the plasma can be written as follows:

$$\frac{\partial f_s}{\partial t} + \mathbf{v} \cdot \frac{\partial f_s}{\partial \mathbf{r}} + \frac{q_s}{m_s}(\mathbf{E} + \mathbf{v} \times \mathbf{B}) \cdot \frac{\partial f_s}{\partial \mathbf{v}} = 0, \tag{2.1}$$

$$\boldsymbol{\nabla}^2 \psi = -\frac{1}{\varepsilon_0} \sum_s q_s \int d\mathbf{v} f_s = -\frac{e}{\varepsilon_0} \left[\sum_{i=2}^{N} Z_i \int d\mathbf{v} f_i - \int d\mathbf{v} f_e \right]. \tag{2.2}$$

In Equation 2.1, the subscript $s = 1, 2, 3, ..., N (N \geqslant 2)$ stands for the species of the ions or electron ($s = 1$). The function $f_s = f_s(\mathbf{r}, \mathbf{v}, t)$ is the distribution function of the corresponding species. The charge in one particle of the species s is represented by $q_s = Z_s e$, where Z_s is the atmoic number with $Z_1 = -1$. Other physical quantities, m_s the mass of the ion, t the time, $\mathbf{v}$ the velocity of a particle, $\mathbf{r}$ the position vector, $\mathbf{E}$ the electric field, and $\mathbf{B}$ the magnetic field are denoted by common notations.

In the second equation, we have the electric potential ψ, the electric charge carried by a single proton e, and the vacuum permittivity $\varepsilon_0 = 8.8 \times 10^{-12}\ \mathrm{F} \cdot \mathrm{m}^{-1}$. In this thesis, for simplicity, we only consider a plasma composed of electrons and one species of ions, with $Z_e = -1$ and $Z_i = 1$. Also, since we are looking for steady-state solutions, all quantities are time-independent. As a result, the first term of the Vlasov equation vanishes. The Vlasov-Poisson system now has a simpler form

$$\mathbf{v} \cdot \frac{\partial f_e}{\partial \mathbf{r}} - \frac{e}{m_e}(\mathbf{E} + \mathbf{v} \times \mathbf{B}) \cdot \frac{\partial f_e}{\partial \mathbf{v}} = 0, \tag{2.3}$$

$$\mathbf{v} \cdot \frac{\partial f_i}{\partial \mathbf{r}} + \frac{e}{m_i}(\mathbf{E} + \mathbf{v} \times \mathbf{B}) \cdot \frac{\partial f_i}{\partial \mathbf{v}} = 0, \tag{2.4}$$

$$\boldsymbol{\nabla}^2 \psi = -\frac{e}{\varepsilon_0} \int d^3 v (f_i - f_e). \tag{2.5}$$

We normalize all three equations through these relations

$$\begin{aligned} &\mathbf{r} = \lambda \bar{\mathbf{r}},\ \mathbf{v} = v_e \bar{\mathbf{v}},\ \psi = \frac{n_{0e} e \lambda^2}{\varepsilon_0} \bar{\psi},\ f_e = \frac{n_{0e}}{v_e^3} \bar{f}_e,\ f_i = \frac{n_{0i}}{v_e^3} \bar{f}_i, \\ &\mathbf{E} = -\boldsymbol{\nabla}\psi = -\frac{n_{0e} e \lambda}{\varepsilon_0} \bar{\boldsymbol{\nabla}} \bar{\psi} = \frac{n_{0e} e \lambda}{\varepsilon_0} \bar{\mathbf{E}},\ \mathbf{B} = \frac{n_{0e} e \lambda}{\varepsilon_0 v_e} \bar{\mathbf{B}}, \end{aligned} \tag{2.6}$$

where v_e is the background electron thermal velocity, and $\lambda = v_e/\omega_{pe} = (v_e/e)\sqrt{\varepsilon_0 m_e/n_{0e}}$ is the Debye length. All the dimensionless quantities are labeled with a top bar. Substituting all the normalization relations into the Vlasov-Poisson system, we have

$$\bar{\mathbf{v}} \cdot \frac{\partial \bar{f}_e}{\partial \bar{\mathbf{r}}} - (\bar{\mathbf{E}} + \bar{\mathbf{v}} \times \bar{\mathbf{B}}) \cdot \frac{\partial \bar{f}_e}{\partial \bar{\mathbf{v}}} = 0, \tag{2.7}$$

$$\bar{\mathbf{v}} \cdot \frac{\partial \bar{f}_i}{\partial \bar{\mathbf{r}}} + \frac{m_e}{m_i}(\bar{\mathbf{E}} + \bar{\mathbf{v}} \times \bar{\mathbf{B}}) \cdot \frac{\partial \bar{f}_i}{\partial \bar{\mathbf{v}}} = 0, \tag{2.8}$$

$$\bar{\boldsymbol{\nabla}}^2 \bar{\psi} = \int d\bar{\mathbf{v}} \Big(\bar{f}_e - \bar{f}_i \Big). \tag{2.9}$$

2.2 Coordinate System

Since we will look for a BGK mode solution with cylindrical symmetry we assume that the electric potential depends only on one dimension, $\psi = \psi(\rho)$, where ρ is the radial coordinate in the cylindrical coordinate system. The Vlasov equation expressed explicitly in cylindrical coordinates with cylindrical symmetry can be obtained by a coordinate transformaion from Cartesian coordaintes. In other words, we are going to change the coordinate system from (x, y, z, v_x, v_y, v_z) to $(\rho, \phi, z, v_\rho, v_\phi, v_z)$. The steady state Vlaosv equation can be rewritten as

$$v_x \frac{\partial f}{\partial x} + v_y \frac{\partial f}{\partial y} + v_z \frac{\partial f}{\partial z} + a_x \frac{\partial f}{\partial x} + a_y \frac{\partial f}{\partial y} + a_z \frac{\partial f}{\partial z} = 0. \tag{2.10}$$

The relations between two coordinate systems are:

$$\rho = \sqrt{x^2 + y^2},\ \phi = \arctan\left(\frac{y}{x}\right),\ y = \rho \sin\phi,\ x = \rho \cos\phi,\ z = z, \tag{2.11}$$

$$v_x = v_\rho \cos\phi - v_\phi \sin\phi,\ v_y = v_\rho \sin\phi + v_\phi \cos\phi,$$

$$v_\rho = v_x \cos\phi + v_y \sin\phi,\ v_\phi = -v_x \sin\phi + v_y \cos\phi,\ v_z = v_z. \tag{2.12}$$

Substitute all the terms, the Vlasov equation can be rewritten as

$$\begin{aligned}0 =& v_\rho \frac{\partial f}{\partial \rho} + \frac{v_\phi}{\rho}\frac{\partial f}{\partial \phi} + v_z \frac{\partial f}{\partial z} \\ &+ \left(\frac{v_\phi^2}{\rho} + a_x \cos\phi + a_y \sin\phi\right)\frac{\partial f}{\partial v_\rho} + \left(-\frac{v_\phi v_\rho}{\rho} - a_x \sin\phi + a_y \cos\phi\right)\frac{\partial f}{\partial v_\phi} + a_z \frac{\partial f}{\partial v_z}. \end{aligned} \tag{2.13}$$

The electric and magnetic fields with cylindrical symmetry can be found by $\mathbf{E} = -\boldsymbol{\nabla}\psi = -d\psi/d\rho\hat{\rho}$ and $\mathbf{B} = \boldsymbol{\nabla}\times\mathbf{A} = \boldsymbol{\nabla}\times[A_\phi\hat{\phi} + A_z\hat{z}] = -dA_z/d\rho\hat{\phi} + (1/\rho)d(\rho A_\phi)/d\rho\hat{z}$. For electrons, the last three term becomes

$$\begin{aligned}&\left(a_x\cos\phi + a_y\sin\phi\right)\frac{\partial f}{\partial v_\rho} + \left(-a_x\sin\phi + a_y\cos\phi\right)\frac{\partial f}{\partial v_\phi} + a_z\frac{\partial f}{\partial v_z} \\ &= \mathbf{a}\cdot\boldsymbol{\nabla}_\mathbf{v} f = -\frac{e}{m_e}(\mathbf{E} + \mathbf{v}\times\mathbf{B})\cdot\boldsymbol{\nabla}_\mathbf{v} f \\ &= \frac{e}{m_e}\frac{d\psi}{d\rho}\frac{\partial f_e}{\partial v_\rho} - \frac{e}{m_e}\left\{\left[\frac{v_\phi}{\rho}\frac{d}{d\rho}(\rho A_\phi) + v_z\left(\frac{dA_z}{d\rho}\right)\right]\frac{\partial f_e}{\partial v_\rho} - \left[\frac{v_\rho}{\rho}\frac{d}{d\rho}(\rho A_\phi)\right]\frac{\partial f_e}{\partial v_\phi} - \left(v_\rho\frac{dA_z}{d\rho}\right)\frac{\partial f_e}{\partial v_z}\right\}. \end{aligned} \tag{2.14}$$

Together, we have the Vlasov equation for electron under cylindrical coordinate is

$$\begin{aligned}v_\rho\frac{\partial f_e}{\partial \rho} + \left\{\frac{e}{m_e}\left[\frac{d\psi}{d\rho} - \frac{v_\phi}{\rho}\frac{d(\rho A_\phi)}{d\rho} - v_z\left(\frac{dA_z}{d\rho}\right)\right] + \frac{v_\phi^2}{\rho}\right\}\frac{\partial f_e}{\partial v_\rho} \\ - \left[\frac{v_\rho v_\phi}{\rho} - \frac{ev_\rho}{m_e}\frac{d(\rho A_\phi)}{\rho d\rho}\right]\frac{\partial f_e}{\partial v_\phi} + \frac{ev_\rho}{m_e}\frac{dA_z}{d\rho}\frac{\partial f_e}{\partial v_z} = 0, \end{aligned} \tag{2.15}$$

and through a similar method we can derive the ion equation,

$$\begin{aligned}v_\rho\frac{\partial f_i}{\partial \rho} + \left\{-\frac{eZ_i}{m_i}\left[\frac{d\psi}{d\rho} - \frac{v_\phi}{\rho}\frac{d(\rho A_\phi)}{d\rho} - v_z\left(\frac{dA_z}{d\rho}\right)\right] + \frac{v_\phi^2}{\rho}\right\}\frac{\partial f_i}{\partial v_\rho} \\ - \left[\frac{v_\rho v_\phi}{\rho} + \frac{eZ_i v_\rho}{m_i}\frac{d(\rho A_\phi)}{\rho d\rho}\right]\frac{\partial f_i}{\partial v_\phi} - \frac{eZ_i v_\rho}{m_i}\frac{dA_z}{d\rho}\frac{\partial f_i}{\partial v_z} = 0. \end{aligned} \tag{2.16}$$

2.3 Forms of The Distribution Functions

2.3.1 Mathematical form

As we discussed in the previous sections, a distribution function of the form $f = f(w)$ cannot be a solution to localized 2D or 3D BGK mode. If we can write a distribution function as a function of conserved quantities, the distribution function will automatically satisfy the Vlasov equation. Other conserved quantities in a cylindrically symmetric system include the axial components of the canonical angular momentum and canonical linear momentum. Thus the distributions will have the following form:

$$\bar{f}_e = \bar{f}_e(\bar{w}_e, \bar{l}_e, \bar{p}_e), \quad \bar{f}_i = \bar{f}_i(\bar{w}_i, \bar{l}_i, \bar{p}_i). \tag{2.17}$$

The independent variables in the formulas above are defined as follows

$$\begin{aligned}
&\bar{w}_e = \frac{\bar{v}^2}{2} - \bar{\psi}, \quad \bar{w}_i = \frac{\bar{v}^2}{2} + \zeta\bar{\psi}, \\
&\bar{l}_e = 2\bar{\rho}(\bar{v}_\phi - \bar{A}_\phi), \quad \bar{l}_i = 2\bar{\rho}(\bar{v}_\phi + \zeta\bar{A}_\phi), \\
&\bar{p}_e = \bar{v}_z - \bar{A}_z, \quad \bar{p}_i = \bar{v}_z + \zeta\bar{A}_z,
\end{aligned} \tag{2.18}$$

where $\bar{w}$ represents the total energy (kinetic and electric potential energy), $\bar{l}$ is the z-component of the canonical angular momentum times two, and $\bar{p}$ is the z-component of the canonical momentum. The quantity ζ is defined as $\zeta = Z_i/M_i$, where $M_i \equiv m_i/m_e$.

Since there are many possible solutions under this form, we cannot solve the equations in an abstract manner, it is necessary to choose specific forms. The velocity distribution functions will therefore be assumed to have the following forms

$$\begin{aligned}
&\bar{f}_e(\bar{w}_e, \bar{l}_e, \bar{p}_e) = (2\pi)^{-3/2} e^{-\bar{w}_e}(1 - h_{0e} e^{-\bar{k}_e \bar{l}_e^2 - \bar{\xi}_e \bar{p}_e^2}), \\
&\bar{f}_i(\bar{w}_i, \bar{l}_i, \bar{p}_i) = (2\pi\tau)^{-3/2} e^{-\bar{w}_i/\tau}(1 - h_{0i} e^{-\bar{k}_i \bar{l}_i^2 - \bar{\xi}_i \bar{p}_i^2}).
\end{aligned} \tag{2.19}$$

The subscripts "e" and "i" in the equations correspondingly represents for electrons and ions.

The first pair of parameters h_{0e} and h_{0i} can be regarded as the "valves" of the equations. If $h_{0e/i} = 0$, the distribution functions then reduce to Boltzmann distributions. Since the Boltzmann distribution alone is not a localized solution for the 2D/3D BGK mode, we must have $h_{0e} \neq 0$, or $h_{0i} \neq 0$. Also, $k_{e/i}$ and $\xi_{e/i}$ have to be positive to keep distributions finite. Since we are looking for solution localized in the radial direction, the electric potential goes to zero when the radial distance goes to infinity ($\lim_{\rho\to\infty} \psi = 0$). Finally, the value of $h_{0e/i}$ has to be less than one. Otherwise because of the proporty of exponential functions, the distribution will become negative in some part of the phase space which is not allowed by definition.

The roles played by the canonical momentum $p_{e/i}$ and the canonical angular momentum $l_{e/i}$ are controlled correspondingly by the other two pairs of parameters $\xi_{e/i}$ and $k_{e/i}$.

The last parameter that only appears in the second distribution function is τ. The parameter is defined as the square of the ratio between background (far away) ion thermal velocity and electron thermal velocity ($\tau = v_i^2/v_e^2$). When the value of τ is large, ions move a lot faster than electrons and thus can be regarded as having a uniform density. With smaller τ ions become more and more important. In space plasma physics, τ is usually of the order of magnitude of 10^{-4}.

Since the electron and ion velocity could also be written as $v_e^2 = \beta_e^2 c^2$ and $v_i^2 = \beta_i^2 c^2$, where c is the speed of light ($\beta_s = v_s/c$), the parameter τ could also be expressed as $\tau = \beta_i^2/\beta_e^2$. This formula indicates if τ and β_e are given, the value of β_i is also fixed.

2.3.2 Electron BGK mode with finite ion temperature

There are nine different parameters in ion and electron velocity distribution functions: h_{0e}, h_{0i}, k_e, k_i, ξ_e, ξ_i, β_e, β_i and τ. Changing each of them might generate a different solution. Therefore, in order to obtain some basic physical properties of solutions within such a large parameter space, we will concentrate our efforts on a few cases where only a few paramenters are varied. In this thesis, three cases will be discussed: (1) electron BGK mode with finite ion temperature, (2) ion BGK mode with finite electron temperature, and (3) some special cases of the electron-ion BGK modes.

The electron BGK mode with finite ion temperature is defined when ion velocity distribution is completely Boltzmann, in other words, the value of h_{0i} is zero. Since $h_{0i} = 0$, the values of other two parameters in the ion velocity distribution, k_i, and ξ_i, will not affect the final result of the distribution function. Hence, in this case the choice of k_i and ξ_i are not relevant to the solution of the equations.

So far the theories are non-relativistic and so the thermal velocity of electron should be small. In numerical simulations, the default value of β_e is $\beta_e = 10^{-5}$ and β_i can be computed through $\beta_i^2 = \tau\beta_e^2$. Therefore, only the values of h_{0e}, k_e, ξ_e and τ will affect the solutions to the differential equations.

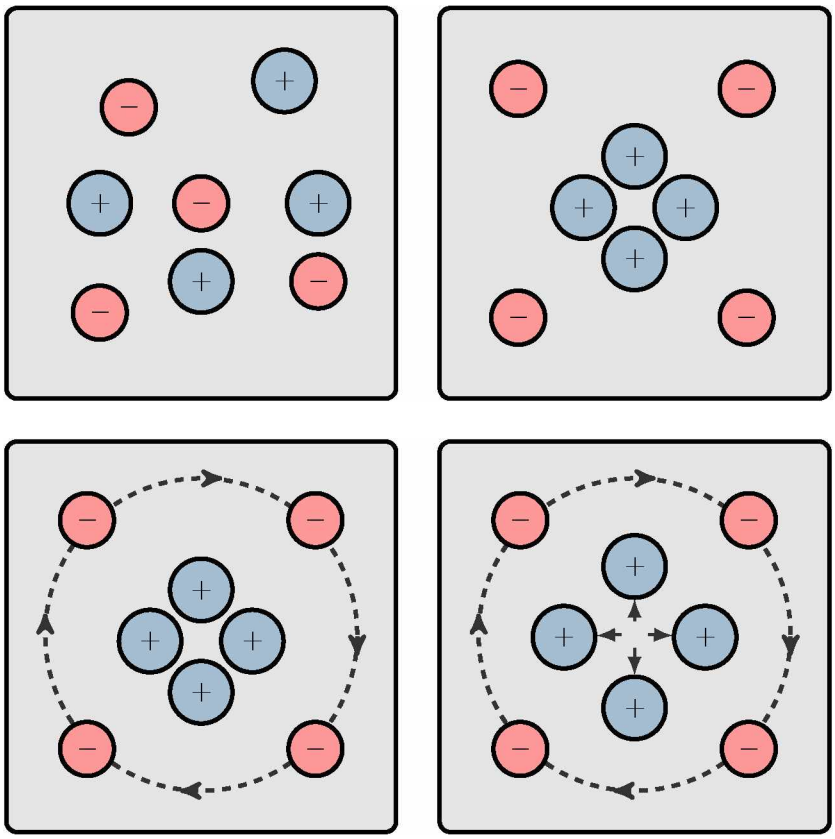

Figure 2.1: The electron BGK mode with finite ion temperature when h_{0e} is positive. The upperleft diagram shows the original quasi-neutral plasma environment. In the upperright diagram the electrons are taken out of the central region. In order to maintain the system, let the electrons rotate around the center clockwise, shown in the lowerleft diagram. Finally, in the lowerright diagram the ions are pushed away from the center by the positive electric potential caused by the lack of the electrons.

The "electron BGK mode with finite ion temperature" case could be further split into two sub-categories: (1) When h_{0e} is positive ($0 < h_{0e} < 1$) (shown in Figure 2.1), and (2) when h_{0e} is

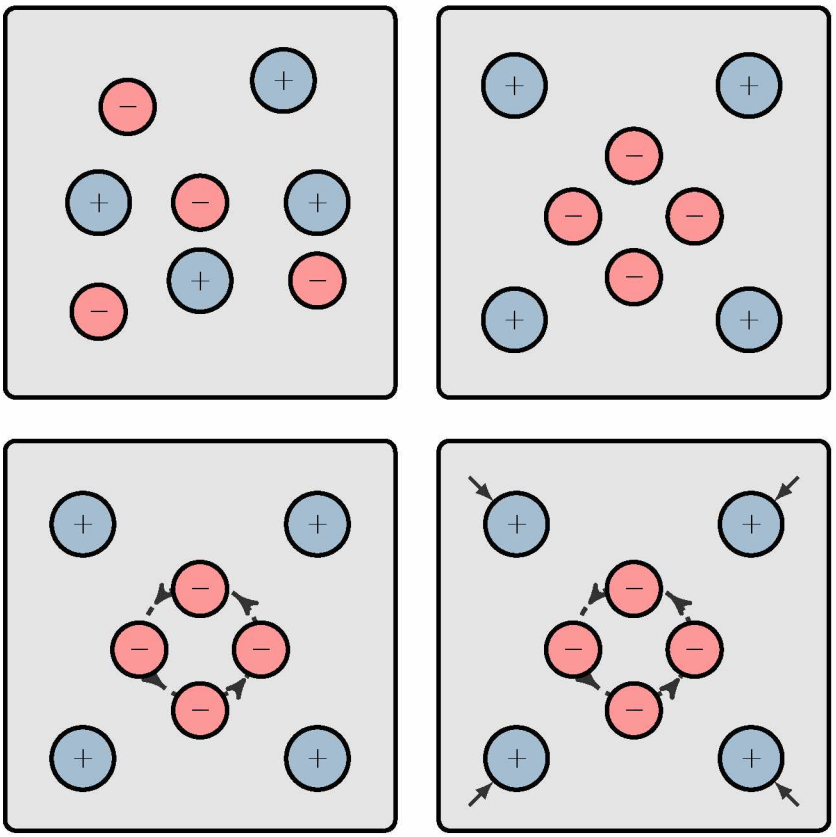

Figure 2.2: The electron BGK mode with finite ion temperature when h_{0e} is negative. The upperleft diagram shows the original quasi-neutral plasma environment. In the upperright diagram the electrons are squeezed into the central region. In order to maintain the system, let the electrons rotate around the center counterclockwise, shown in the lowerleft diagram. Finally, in the lowerright diagram the ions are attracted to the center by the negative electric potential created by the electrons.

negative (shown in Figure 2.2). The physical meaning behind the first case is: some electrons are taken out of the central region. As a result, the central region will have positive electric potentials because of the lack of electrons. The parameter k_e which characterizes the angular momentum effect in the equation must have a non-zero value. Electrons not taken out preferentially rotate around the center of the region in order to sustain the equilibrium. Becuase of the rotation, the $\hat{\phi}$ component of electron velocity should have a local maximum and non-zero current must also exist.

Instead of taking out electrons, we could also put electrons into the central region. The situation corresponds to the second category of the electron BGK mode with finite ion temperature where the parameter h_{0e} is negative. Electric potential is negative in the central region and converges to a higher constant magnitude at infinity. With other parameters unchanged from

the $h_{0e} > 0$ case, the $\hat{\phi}$ component of velocity should rotate around the center with the opposite direction. In summary, for $h_{0e} > 0$, electrons rotates around the central region, causing a positive electric potential in the central area and a magnetic bump; for $h_{0e} < 0$, electrons rotates around the central region with the opposite orientation, causing a negative electric potential in the central area and a magnetic hole. The direction of rotation depends on the direction of the initial magneitc field $\mathbf{B}_{0z}$.

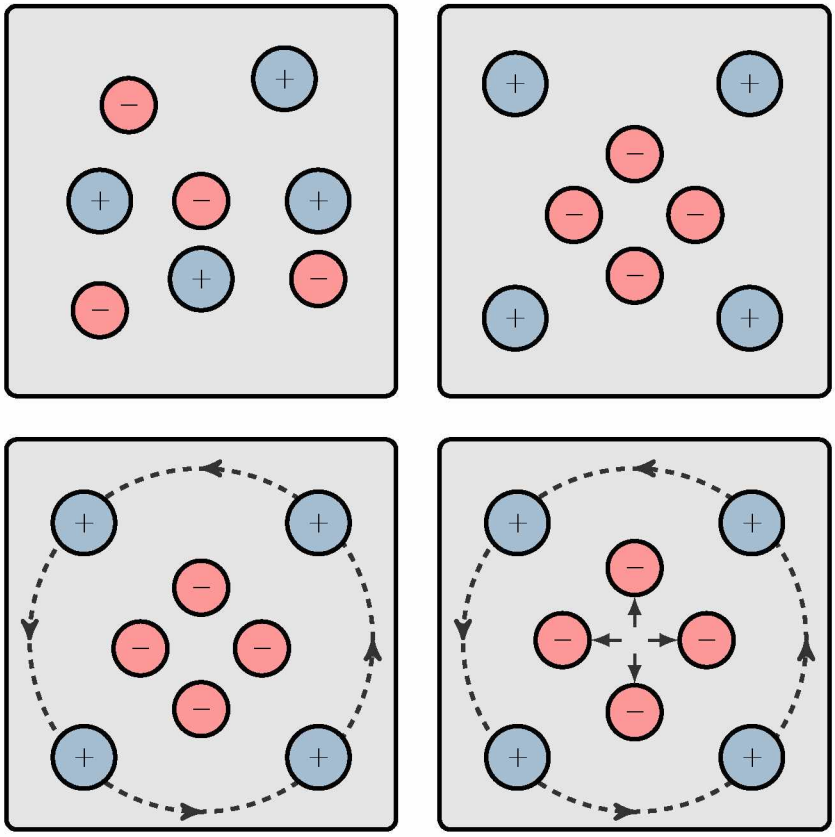

Figure 2.3: The ion BGK mode with finite electron temperature when h_{0i} is positive. The upperleft diagram shows the original quasi-neutral plasma environment. In the upperright diagram the ions are taken out of the central region. In order to maintain the system, let the ions rotate around the center counterclockwise, shown in the lowerleft diagram. Finally, in the lowerright diagram the electrons are pushed away from the center by the positive electric potential created by the lack of ions.

2.3.3 Ion BGK mode with finite electron temperature

The ion BGK mode with finite electron temperature is defined when electron velocity distribution is completely Boltzmann. The mode is constructed oppositely from the setup of an

electron BGK mode. Since electron velocity distribution is Boltzmann, $h_{0e} = 0$, and the choice of k_e and ξ_e are not relevant to the solution of the equations.

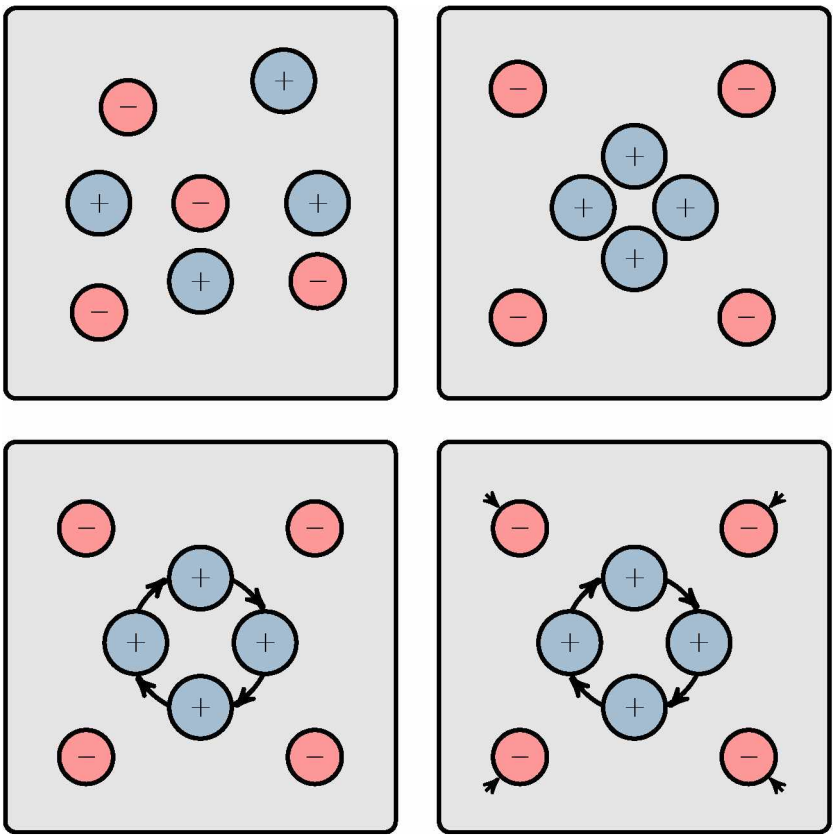

Figure 2.4: The ion BGK mode with finite electron temperature when h_{0i} is negative. The upperleft diagram shows the original quasi-neutral plasma environment. In the upperright diagram the ions are squeezed into the central region. In order to maintain the system, let the ions rotate around the center clockwise, shown in the lowerleft diagram. Finally, in the lowerright diagram the electrons are attracted to the center by the positive electric potential created by the ions in the center.

Similar to the electron BGK mode, the ion BGK mode is also constructed within the non-relativistic regime and thus $\beta_i = v_i/c$ is much less than one. In this case, β_e is given by $\beta_e^2 = \beta_i^2/\tau$, and so only the values of h_{0i}, k_i, ξ_i and τ will affect the solutions to the differential equations.

The "ion BGK mode with finite electron temperature" case could also be divided into two sub-categories: (1) When h_{0i} is positive ($0 < h_{0i} < 1$, shown in Figure 2.3), and (2) when h_{0i} is negative (shown in Figure 2.4). The ion particles are taken out of the central region in the first case. The central region will be lack of positive particles and therefore the electric potential in the central region will be negative. The non-zero parameter k_i will lead to the rotation of ions around the center of the region thus the equilibrium is satisfied. The rotation of ions also casues

a local maximum of the ϕ component of ion velocity and non-zero current. The negative electric potential in the central region will push electrons out of the region. Thus the number densities of both electrons and ions are less than their corresponding background densities. In other words, electron and ion density holes will appear under such this case.

For the second case the ions are put into the central region. The extra ions in the central region will cause a positive electric potential. The positive electric potential will decrease and converge to zero as distance goes to infinity. To maintain the equilibrium, the ions will rotate around the center in the opposite direction as compared with the positive h_{0i} case. Again, a non-zero current will be formed by the rotation of ions.

2.4 The Number Density and The First ODE

2.4.1 Number densities: $\bar{n}_e$ and $\bar{n}_i$

The first ordinary differential equation is derived from the Poisson equation. In cylindrical coordinate, the Poisson equation can be rewritten as

$$\frac{1}{\bar{\rho}}\frac{d}{d\bar{\rho}}\left(\bar{\rho}\frac{d\bar{\psi}}{d\bar{\rho}}\right) = \int d^3\bar{v}(\bar{f}_e - \bar{f}_i) = \bar{n}_e - \bar{n}_i, \tag{2.20}$$

where $\bar{n}_e$ and $\bar{n}_i$ are dimensionless number density for electrons and ions

$$\begin{aligned}
\bar{n}_e &= \int_{-\infty}^{\infty} d\bar{v}_z \int_{-\infty}^{\infty} d\bar{v}_\rho \int_{-\infty}^{\infty} d\bar{v}_\phi \left[\bar{f}_e\left(\frac{\bar{v}^2}{2} - \bar{\psi}, 2\bar{\rho}(\bar{v}_\phi - \bar{A}_\phi), \bar{v}_z - \bar{A}_z\right)\right], \\
\bar{n}_i &= \int_{-\infty}^{\infty} d\bar{v}_z \int_{-\infty}^{\infty} d\bar{v}_\rho \int_{-\infty}^{\infty} d\bar{v}_\phi \left[\bar{f}_i\left(\frac{\bar{v}^2}{2} + \zeta\bar{\psi}, 2\bar{\rho}(\bar{v}_\phi + \zeta\bar{A}_\phi), \bar{v}_z + \zeta\bar{A}_z\right)\right].
\end{aligned} \tag{2.21}$$

Using the forms given by Equation 2.19, we have

$$\begin{aligned}
\bar{n}_e &= \exp[\bar{\psi}(\bar{\rho})]\left[1 - \frac{h_{0e}}{\sqrt{(1+8\bar{k}_e\bar{\rho}^2)(1+2\bar{\xi}_e)}}\exp\left(-\frac{4\bar{k}_e\bar{\rho}^2\bar{A}_\phi^2}{1+8\bar{k}_e\bar{\rho}^2} - \frac{\bar{\xi}_e\bar{A}_z^2}{1+2\bar{\xi}_e}\right)\right], \\
\bar{n}_i &= \exp\left[-\frac{\zeta\bar{\psi}(\bar{\rho})}{\tau}\right]\left[1 - \frac{h_{0i}}{\sqrt{(1+8\bar{k}_i\tau\bar{\rho}^2)(1+2\tau\bar{\xi}_i)}}\exp\left(-\frac{4\bar{k}_i\bar{\rho}^2\zeta^2\bar{A}_\phi^2}{1+8\bar{k}_i\tau\bar{\rho}^2} - \frac{\bar{\xi}_i\zeta^2\bar{A}_z^2}{1+2\tau\bar{\xi}_i}\right)\right].
\end{aligned} \tag{2.22}$$

The details of these two integrations are attached in the Appendix. Some of the terms within these equations will frequently appear in the derivations below. For the purpose of convenience, they are replaced by simplier notations, with "t_e" standing for "terms related to electrons" and "t_i" standing for "terms related to ions".

$$
\begin{aligned}
&t_{\mathrm{e}1} = 2\bar{\xi}_e, \quad t_{\mathrm{e}2} = \bar{A}_z^2\xi_e, \quad t_{\mathrm{e}3} = 8\bar{\rho}^2\bar{k}_e, \quad t_{\mathrm{e}4} = 4\bar{\rho}^2\bar{A}_\phi^2\bar{k}_e,\\
&t_{\mathrm{i}1} = 2\tau\bar{\xi}_i, \quad t_{\mathrm{i}2} = \zeta^2\bar{A}_z^2\bar{\xi}_i, \quad t_{\mathrm{i}3} = 8\bar{\rho}^2\tau\bar{k}_i, \quad t_{\mathrm{i}4} = 4\zeta^2\bar{\rho}^2\bar{A}_\phi^2\bar{k}_i,\\
&\Omega_e = h_{0e}[(t_{\mathrm{e}1}+1)(t_{\mathrm{e}3}+1)]^{-1/2}\exp\bigg(-\frac{t_{\mathrm{e}4}}{t_{\mathrm{e}3}+1}-\frac{t_{\mathrm{e}2}}{t_{\mathrm{e}1}+1}\bigg),\\
&\Omega_i = h_{0i}[(t_{\mathrm{i}1}+1)(t_{\mathrm{i}3}+1)]^{-1/2}\exp\bigg(-\frac{t_{\mathrm{i}4}}{t_{\mathrm{i}3}+1}-\frac{t_{\mathrm{i}2}}{t_{\mathrm{i}1}+1}\bigg).
\end{aligned}
\tag{2.23}
$$

Thus the number density can be rewritten by a simpler form:

$$
\boxed{\bar{n}_e = \frac{n_e}{n_{e0}} = \exp(\bar{\psi})(1-\Omega_e)} \tag{2.24}
$$

$$
\boxed{\bar{n}_i = \frac{n_i}{n_{i0}} = \exp\bigg(-\frac{\zeta\bar{\psi}}{\tau}\bigg)(1-\Omega_i)} \tag{2.25}
$$

2.4.2 The 1st ODE

Now substitute expressions of $\bar{n}_e$ and $\bar{n}_i$ into the RHS of the Poisson Equation to obtain the first ordinary differential equation

$$
\begin{aligned}
\frac{1}{\bar{\rho}}\frac{d}{d\bar{\rho}}\bigg(\bar{\rho}\frac{d\bar{\psi}}{d\bar{\rho}}\bigg) = {}&\exp[\bar{\psi}(\bar{\rho})]\bigg[1-\frac{h_{0e}}{\sqrt{(1+8\bar{k}_e\bar{\rho}^2)(1+2\bar{\xi}_e)}}\exp\bigg(-\frac{4\bar{k}_e\bar{\rho}^2\bar{A}_\phi^2}{1+8\bar{k}_e\bar{\rho}^2}-\frac{\bar{\xi}_e\bar{A}_z^2}{1+2\bar{\xi}_e}\bigg)\bigg]\\
&-\exp\bigg[-\frac{\zeta\bar{\psi}(\bar{\rho})}{\tau}\bigg]\bigg[1-\frac{h_{0i}}{\sqrt{(1+8\bar{k}_i\tau\bar{\rho}^2)(1+2\tau\bar{\xi}_i)}}\exp\bigg(-\frac{4\bar{k}_i\bar{\rho}^2\zeta^2\bar{A}_\phi^2}{1+8\bar{k}_i\tau\bar{\rho}^2}-\frac{\bar{\xi}_i\zeta^2\bar{A}_z^2}{1+2\tau\bar{\xi}_i}\bigg)\bigg].
\end{aligned}
\tag{2.26}
$$

or,

$$
\boxed{\bar{\psi}'' + \frac{\bar{\psi}'}{\bar{\rho}} = \exp(\bar{\psi})(1-\Omega_e) - \exp\bigg(-\frac{\zeta\bar{\psi}}{\tau}\bigg)(1-\Omega_i)}. \tag{2.27}
$$

2.5 The 2nd and 3rd ODE

The non-zero charge desntiy and flow volocity will lead to a finite current density. Through the Ampère's law we can compute the self-consistent magnetic field $\mathbf{B}$ by

$$\nabla \times \mathbf{B} = \mu_0 e \int d^3v \Big(f_i - f_e \Big) \mathbf{v}, \tag{2.28}$$

or, dimensionlessly

$$\overline{\nabla} \times \overline{\mathbf{B}} = \beta_e^2 \int d^3\bar{\mathbf{v}} (\bar{f}_i - \bar{f}_e) \bar{\mathbf{v}}, \tag{2.29}$$

where $\beta_e^2 = v_e^2/c^2$. Since the theory in this thesis is under the non-relativistic assumption, the value of β_e^2 should be much less than one ($\beta_e^2 \ll 1$). The RHS of the equation can be integrated through a similar method as in the previous section. The details, again, are attached in the Appendix. The LHS could also be further expanded if we decompose magnetic field $\bar{\mathbf{B}}$ into its ϕ component and z component. Since the electric field is a function of ρ only, the magnetic field depends only on ρ as well ($\bar{B}_\phi = \bar{B}_\phi(\rho)$, $\bar{B}_z = \bar{B}_z(\rho)$). The result is

$$\overline{\nabla} \times \overline{\mathbf{B}} = -\hat{\phi} \frac{d}{d\bar{\rho}} \left[\frac{1}{\bar{\rho}} \frac{d}{d\bar{\rho}} (\bar{\rho} \bar{A}_\phi) \right] - \hat{z} \frac{1}{\bar{\rho}} \frac{d}{d\bar{\rho}} \left(\bar{\rho} \frac{d\bar{A}_z}{d\bar{\rho}} \right).$$

The Ampère law implies that with a non-zero ϕ component of the electron or ion velocity, magnetic field under the equilibrium would be different from the original background magnetic field. Therefore, a local extremum will exist in the central region. If the electrons rotate around the center clockwise, or the ions rotate around the center counterclockwise the magnetic field in the center will be enhanced. A magnetic "bump" will appear under such cases. If the electrons rotate around the center counterclockwise or the ions rotate the center clockwise, a magnetic "dent" or a magnetic "hole" would occur.

Now the equation derived from the Ampère's law can be rewritten as two equations, one for the ϕ component and the other for the z component, which are the second and the third ODE:

$$\frac{1}{\bar{\rho}}\frac{d}{d\bar{\rho}}\left(\bar{\rho}\frac{d\bar{A}_z}{d\bar{\rho}}\right) = -\frac{2\beta_e^2\bar{A}_z\bar{\xi}_e h_{0e}}{\sqrt{1+8\bar{\rho}^2\bar{k}_e}(1+2\bar{\xi}_e)^{3/2}}\exp\left[\bar{\psi}-\frac{\bar{A}_z^2\bar{\xi}_e}{1+2\bar{\xi}_e}-\frac{4\bar{\rho}^2\bar{k}_e\bar{A}_\phi^2}{1+8\bar{\rho}^2\bar{k}_e}\right] - \frac{2\beta_i^2\zeta\bar{A}_z\bar{\xi}_i h_{0i}}{\sqrt{1+8\bar{\rho}^2\tau\bar{k}_i}(1+2\tau\bar{\xi}_i)^{3/2}}\exp\left[-\frac{\zeta\bar{\psi}}{\tau}-\frac{4\bar{\rho}^2\bar{k}_i\zeta^2\bar{A}_\phi^2}{1+8\bar{\rho}^2\tau\bar{k}_i}-\frac{\zeta^2\bar{\xi}_i\bar{A}_z^2}{1+2\tau\bar{\xi}_i}\right], \quad (2.30)$$

and

$$\frac{d}{d\bar{\rho}}\left[\frac{1}{\bar{\rho}}\frac{d}{d\bar{\rho}}(\bar{\rho}\bar{A}_\phi)\right] = -\frac{8\bar{\rho}^2\beta_e^2\bar{A}_\phi\bar{k}_e h_{0e}}{(1+8\bar{\rho}^2\bar{k}_e)^{3/2}\sqrt{1+2\bar{\xi}_e}}\exp\left[\bar{\psi}-\frac{4\bar{k}_e\bar{A}_\phi^2\bar{\rho}^2}{1+8\bar{k}_e\bar{\rho}^2}-\frac{\bar{A}_z^2\bar{\xi}_e}{1+2\bar{\xi}_e}\right] - \frac{8\bar{\rho}^2\beta_i^2\zeta\bar{A}_\phi\bar{k}_i h_{0i}}{(1+8\bar{\rho}^2\tau\bar{k}_i)^{3/2}\sqrt{1+2\tau\bar{\xi}_i}}\exp\left[-\frac{\zeta\bar{\psi}}{\tau}-\frac{\zeta^2 4\bar{\rho}^2\bar{k}_i\bar{A}_\phi^2}{1+8\bar{\rho}^2\tau\bar{k}_i}-\frac{\zeta^2\bar{A}_z^2\bar{\xi}_i}{1+2\tau\bar{\xi}_i}\right]. \quad (2.31)$$

where $\beta_i = v_i/c$. Simplify the equations above by notations defined previously, the two equations become

$$\boxed{\bar{A}_z^{''}+\frac{\bar{A}_z^{'}}{\bar{\rho}} = -\bar{A}_z\beta_e^2\left[\frac{t_{e1}\Omega_e}{1+t_{e1}}\exp(\bar{\psi})+\frac{\zeta t_{i1}\Omega_i}{1+t_{i1}}\exp\left(-\frac{\zeta\bar{\psi}}{\tau}\right)\right]} \quad (2.32)$$

$$\boxed{\bar{A}_\phi^{''}+\frac{\bar{A}_\phi^{'}}{\bar{\rho}}-\frac{\bar{A}_\phi}{\bar{\rho}^2} = -\bar{A}_\phi\beta_e^2\left[\frac{t_{e3}\Omega_e}{1+t_{e3}}\exp(\bar{\psi})+\frac{\zeta t_{i3}\Omega_i}{1+t_{i3}}\exp\left(-\frac{\zeta\bar{\psi}}{\tau}\right)\right]} \quad (2.33)$$

2.6 Bulk Velocities and Temperatures

2.6.1 Bulk velocities: $\langle\bar{\mathbf{v}}\rangle_e$ and $\langle\bar{\mathbf{v}}\rangle_i$

The bulk velocity for type s is defined as the 1st moment of velocity distribution functions divided by the corresponding number density:

$$\langle\mathbf{v}\rangle_s = \frac{\int_{-\infty}^{\infty}\mathbf{v}f_s(\mathbf{v})d^3v}{\int_{-\infty}^{\infty}f_s(\mathbf{v})d^3v} = \frac{1}{n_s}\int_{-\infty}^{\infty}\mathbf{v}f_s(\mathbf{v})d^3v. \quad (2.34)$$

To make it dimensionless, bulk velocity is normalized by electron velocity

$$\langle\bar{\mathbf{v}}\rangle_s = \frac{\langle\mathbf{v}\rangle_s}{v_e} = \frac{1}{v_e n_s}\int_{-\infty}^{\infty}\mathbf{v}f_s(\mathbf{v})d^3v. \tag{2.35}$$

Explicitly, for electrons, the dimensionless bulk velocity is

$$\begin{aligned}\langle\bar{\mathbf{v}}\rangle_e &= \frac{\langle\mathbf{v}\rangle_e}{v_e} = \frac{\int d^3v f_e\mathbf{v}}{v_e n_e}\\ &= -\frac{2h_{0e}\left[\dfrac{4\bar{\rho}^2\bar{A}_\phi\bar{k}_e\hat{\phi}}{1+8\bar{\rho}^2\bar{k}_e}+\dfrac{\bar{A}_z\bar{\xi}_e\hat{z}}{1+2\bar{\xi}_e}\right]\exp\left(-\dfrac{4\bar{\rho}^2\bar{A}_\phi^2\bar{k}_e}{1+8\bar{\rho}^2\bar{k}_e}-\dfrac{\bar{A}_z^2\bar{\xi}_e}{1+2\bar{\xi}_e}\right)}{\sqrt{1+8\bar{\rho}^2\bar{k}_e}\sqrt{1+2\bar{\xi}_e}-h_{0e}\exp\left(-\dfrac{4\bar{\rho}^2\bar{A}_\phi^2\bar{k}_e}{1+8\bar{\rho}^2\bar{k}_e}-\dfrac{\bar{A}_z^2\bar{\xi}_e}{1+2\bar{\xi}_e}\right)},\end{aligned} \tag{2.36}$$

and the bulk velocity for ions is

$$\begin{aligned}\langle\bar{\mathbf{v}}\rangle_i &= \frac{\langle\mathbf{v}\rangle_i}{v_e} = \frac{\int d^3v f_i\mathbf{v}}{v_e n_i}\\ &= \frac{2h_{0i}\tau\zeta\left[\dfrac{4\bar{k}_i\bar{\rho}^2\bar{A}_\phi}{1+8\bar{k}_i\tau\bar{\rho}^2}\hat{\phi}+\dfrac{\bar{\xi}_i\bar{A}_z}{1+2\bar{\xi}_i\tau}\hat{z}\right]\exp\left(-\dfrac{4\zeta^2\bar{k}_i\bar{\rho}^2\bar{A}_\phi^2}{1+8\bar{k}_i\tau\bar{\rho}^2}-\dfrac{\zeta^2\bar{\xi}_i\bar{A}_z^2}{1+2\bar{\xi}_i\tau}\right)}{\sqrt{1+8\bar{k}_i\tau\bar{\rho}^2}\sqrt{1+2\bar{\xi}_i\tau}-h_{0i}\exp\left[-\dfrac{4\bar{k}_i\bar{\rho}^2\bar{A}_\phi^2}{1+8\bar{k}_i\tau\bar{\rho}^2}-\dfrac{\bar{\xi}_i\bar{A}_z^2}{1+2\bar{\xi}_i\tau}\right]}.\end{aligned} \tag{2.37}$$

With substitutions constructed in Section 2.4, the expressions can be simplified to the following form

$$\boxed{\langle\bar{\mathbf{v}}\rangle_e = \left(-\frac{\hat{\phi}\bar{A}_\phi t_{e3}}{1+t_{e3}}-\frac{\hat{z}\bar{A}_z t_{e1}}{1+t_{e1}}\right)\frac{\Omega_e}{1-\Omega_e}} \tag{2.38}$$

$$\boxed{\langle\bar{\mathbf{v}}\rangle_i = \left(\frac{\hat{\phi}\bar{A}_\phi t_{i3}}{1+t_{i3}}+\frac{\hat{z}\bar{A}_z t_{i1}}{1+t_{i1}}\right)\frac{\zeta\Omega_i}{1-\Omega_i}} \tag{2.39}$$

2.6.2 Average temperatures: $\overline{T}_e$ and $\overline{T}_i$

The average energy for particle s is defined as

$$E_s = \frac{3}{2}k_B T_s = \frac{\displaystyle\int_{-\infty}^{\infty}\frac{1}{2}m_s\mathbf{u}_s^2 f_s(\mathbf{v})d^3v}{\displaystyle\int_{-\infty}^{\infty}f_s(\mathbf{v})d^3v} = \frac{1}{n_s}\int_{-\infty}^{\infty}\frac{1}{2}m_s u_s^2 f_s(\mathbf{v})d^3v \tag{2.40}$$

where u_s is the difference between velocity and bulk velocity ($\mathbf{u}_s = \mathbf{v} - \langle \mathbf{v} \rangle_s$). Normalize the right hand side of the equation

$$\begin{aligned}
\frac{3}{2} k_B T_s &= \frac{1}{n_s} \int_{-\infty}^{\infty} \frac{1}{2} m_s u_s^2 f_s(\mathbf{v}) d^3 v \\
&= \frac{v_e^2}{\bar{n}_s} \int_{-\infty}^{\infty} \frac{1}{2} m_s (\bar{\mathbf{v}} - \langle \bar{\mathbf{v}} \rangle_s)^2 \bar{f}_s(\bar{\mathbf{v}}) d^3 \bar{v} \\
&= \frac{1}{3} \left(\frac{3 k_B T_{s0}}{2} \right) \left[\frac{1}{\bar{n}_s} \int_{-\infty}^{\infty} \bar{v}^2 \bar{f}_s d^3 \bar{v} - \langle \bar{\mathbf{v}} \rangle_s^2 \right],
\end{aligned} \tag{2.41}$$

or

$$T_s = \frac{T_{s0}}{3} \left[\frac{1}{\bar{n}_s} \int_{-\infty}^{\infty} \bar{v}^2 \bar{f}_s d^3 \bar{v} - \langle \bar{\mathbf{v}} \rangle_s^2 \right], \tag{2.42}$$

where T_{s0} is the background temperature. The dimensionless temperature is defined as the quotient between temperature and background temperature. For electrons and ions, the corresponding dimensionless temperatures are

$$\begin{aligned}
\bar{T}_e &= \frac{T_e}{T_{e0}} = \frac{1}{3} \left[\frac{1}{\bar{n}_e} \int_{-\infty}^{\infty} \bar{v}^2 \bar{f}_e(\bar{\mathbf{v}}) d^3 \bar{v} - \langle \bar{\mathbf{v}} \rangle_e^2 \right], \\
\bar{T}_i &= \frac{T_i}{T_{i0}} = \frac{1}{3\tau} \left[\frac{1}{\bar{n}_i} \int_{-\infty}^{\infty} \bar{v}^2 \bar{f}_i(\bar{\mathbf{v}}) d^3 \bar{v} - \langle \bar{\mathbf{v}} \rangle_i^2 \right],
\end{aligned} \tag{2.43}$$

or,

$$\boxed{\bar{T}_e = \frac{T_e}{T_{e0}} = -\frac{2}{3} \frac{\Omega_e h_{0e}^2}{(1-\Omega_e)^2} \frac{\left(-\dfrac{\hat{\phi} \bar{A}_\phi t_{e3}}{1+t_{e3}} + \dfrac{\hat{z} \bar{A}_z t_{e1} \beta_e^2}{1+t_{e1}} \right)^2}{\sqrt{1+t_{e1}} \sqrt{1+t_{e3}}} + \frac{3 - \left[1 + \dfrac{\bar{A}_z^2 t_{e1}^2}{(1+t_{e1})^2} + \dfrac{1}{1+t_{e1}} + \dfrac{\bar{A}_\phi^2 t_{e3}^2}{(1+t_{e3})^2} + \dfrac{1}{1+t_{e3}} \right]}{3(1-\Omega_e)}} \tag{2.44}$$

$$\boxed{\bar{T}_i = \frac{T_i}{T_{i0}} = -\frac{2}{3} \frac{\zeta^2 \Omega_i h_{0i}^2}{(1-\Omega_e)^2} \frac{\left(-\dfrac{\hat{\phi} \bar{A}_\phi t_{i3}}{1+t_{i3}} + \dfrac{\hat{z} \bar{A}_z t_{i1} \beta_e^2}{1+t_{i1}} \right)^2}{\sqrt{1+t_{i1}} \sqrt{1+t_{i3}}} + \frac{3 - \left[1 + \dfrac{\zeta^2 \bar{A}_z^2 t_{i1}^2}{\tau(1+t_{i1})^2} + \dfrac{1}{1+t_{i1}} + \dfrac{\zeta^2 \bar{A}_\phi^2 t_{i3}^2}{\tau(1+t_{i3})^2} + \dfrac{1}{1+t_{i3}} \right]}{3(1-\Omega_i)}} \tag{2.45}$$

2.7 Summary

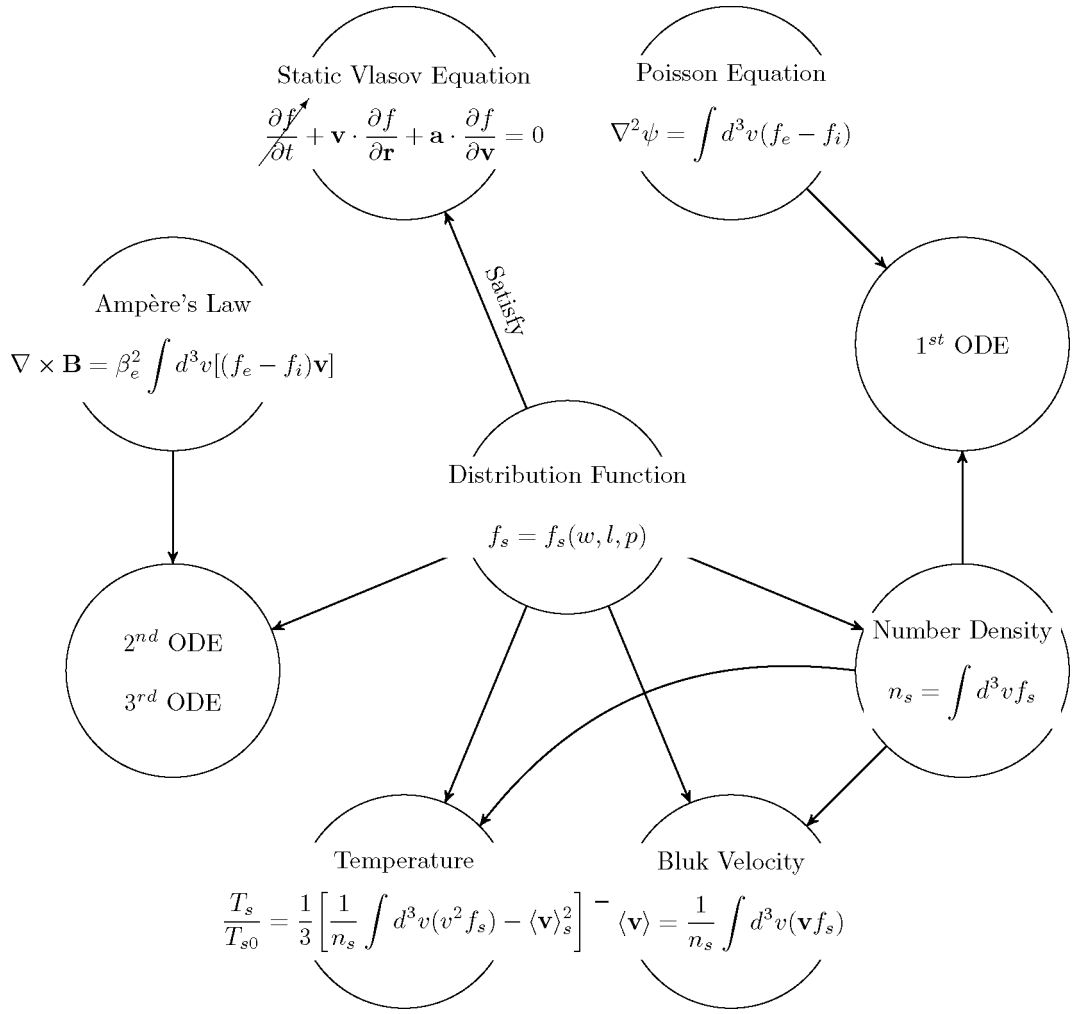

Since most of the analysis in this paper will be dimensionless, it is not necessary to emphasis all the dimensionless quantities with a top bar, the top bars will be removed in this section and all subsequent chapters. As illustrated in the flow chart above, with distribution functions that satisfies *Vlasov Equation*, the *Ampère's Law*, and the *Poisson equation*, three ordinary differential equations are solved and three pairs of physical quantities are then calculated. The three equations are:

$$\psi^{''} + \frac{\psi^{'}}{\rho} = \exp(\psi)(1-\Omega_e) - \exp\Big(-\frac{\zeta\psi}{\tau}\Big)(1-\Omega_i) \tag{2.46}$$

$$A_z^{''} + \frac{A_z^{'}}{\rho} = -A_z\beta_e^2\Big[\frac{t_{e1}\Omega_e}{1+t_{e1}}\exp(\psi) + \frac{\zeta t_{i1}\Omega_i}{1+t_{i1}}\exp\Big(-\frac{\zeta\psi}{\tau}\Big)\Big] \tag{2.47}$$

$$A_\phi^{''} + \frac{A_\phi^{'}}{\rho} - \frac{A_\phi}{\rho^2} = -A_\phi\beta_e^2\Big[\frac{t_{e3}\Omega_e}{1+t_{e3}}\exp(\psi) + \frac{\zeta t_{i3}\Omega_i}{1+t_{i3}}\exp\Big(-\frac{\zeta\psi}{\tau}\Big)\Big], \tag{2.48}$$

and the three pairs of physical properties are (1) number densities for electrons and ions, (2) average velocities for electrons and ions, and (3) temperatures for electrons and ions. They are:

$$\frac{n_e}{n_{e0}} = \exp(\psi)(1-\Omega_e), \quad \frac{n_i}{n_{i0}} = \exp\Big(-\frac{\zeta\psi}{\tau}\Big)(1-\Omega_i) \tag{2.49}$$

$$\langle\mathbf{v}\rangle_e = \Big(-\frac{\hat{\phi}A_\phi t_{e3}}{1+t_{e3}} - \frac{\hat{z}A_z t_{e1}}{1+t_{e1}}\Big)\frac{\Omega_e}{1-\Omega_e} \tag{2.50}$$

$$\langle\mathbf{v}\rangle_i = \Big(\frac{\hat{\phi}A_\phi t_{i3}}{1+t_{i3}} + \frac{\hat{z}A_z t_{i1}\beta_e^2}{1+t_{i1}}\Big)\frac{\zeta\Omega_i}{1-\Omega_i} \tag{2.51}$$

$$\begin{aligned}\frac{T_e}{T_{e0}} = &-\frac{2}{3}\frac{\Omega_e h_{0e}^2}{(1-\Omega_e)^2}\frac{\Big(-\frac{\hat{\phi}A_\phi t_{e3}}{1+t_{e3}} + \frac{\hat{z}A_z t_{e1}\beta_e^2}{1+t_{e1}}\Big)^2}{\sqrt{1+t_{e1}}\sqrt{1+t_{e3}}} \\ &+ \frac{3-\Big[1+\frac{A_z^2 t_{e1}^2}{(1+t_{e1})^2} + \frac{1}{1+t_{e1}} + \frac{A_\phi^2 t_{e3}^2}{(1+t_{e3})^2} + \frac{1}{1+t_{e3}}\Big]}{3(1-\Omega_e)}\end{aligned} \tag{2.52}$$

$$\begin{aligned}\frac{T_i}{T_{i0}} = &-\frac{2}{3}\frac{\zeta^2\Omega_i h_{0i}^2}{(1-\Omega_e)^2}\frac{\Big(-\frac{\hat{\phi}A_\phi t_{i3}}{1+t_{i3}} + \frac{\hat{z}A_z t_{i1}\beta_e^2}{1+t_{i1}}\Big)^2}{\sqrt{1+t_{i1}}\sqrt{1+t_{i3}}} \\ &+ \frac{3-\Big[1+\frac{\zeta^2 A_z^2 t_{i1}^2}{\tau(1+t_{i1})^2} + \frac{1}{1+t_{i1}} + \frac{\zeta^2 A_\phi^2 t_{i3}^2}{\tau(1+t_{i3})^2} + \frac{1}{1+t_{i3}}\Big]}{3(1-\Omega_i)},\end{aligned} \tag{2.53}$$

where

$$\begin{aligned}&t_{\rm e1} = 2\xi_e, \quad t_{\rm e2} = A_z^2\xi_e, \quad t_{\rm e3} = 8\rho^2 k_e, \quad t_{\rm e4} = 4\rho^2 A_\phi^2 k_e, \\ &t_{\rm i1} = 2\tau\xi_i, \quad t_{\rm i2} = \zeta^2 A_z^2\xi_i, \quad t_{\rm i3} = 8\rho^2\tau k_i, \quad t_{\rm i4} = 4\zeta^2\rho^2 A_\phi^2 k_i, \\ &\Omega_e = h_{0e}[(t_{\rm e1}+1)(t_{\rm e3}+1)]^{-1/2}\exp\Big(-\frac{t_{\rm e4}}{t_{\rm e3}+1} - \frac{t_{\rm e2}}{t_{\rm e1}+1}\Big), \\ &\Omega_i = h_{0i}[(t_{\rm i1}+1)(t_{\rm i3}+1)]^{-1/2}\exp\Big(-\frac{t_{\rm i4}}{t_{\rm i3}+1} - \frac{t_{\rm i2}}{t_{\rm i1}+1}\Big).\end{aligned} \tag{2.54}$$

Chapter 3

Numerical Methods

Numerical methods of solving this system of differential equations rely on either initial conditions or boundary conditions. The initial conditions and boundary conditions of electric potential ψ are derived in Section 3.1, and that of A_z and A_ϕ are deduced in Section 3.2 and Section 3.3. Then, a double precision initial condition method introduced in Section 3.4 is implemented to solve the system of equation numerically. All the initial conditions derived in Section 3.1 and 3.2 ($\psi(0)$, $\psi'(0)$, $A_z(0)$, $A'_z(0)$, $A_\phi(0)$, and $A'_\phi(0)$) will be used in this method. Snippets of codes are also presented to assist interpreting the algorithms.

3.1 Initial and Boundary Conditions for ψ

For convenience, the right hand sides of the differential equations are simplified and are named "RHS_1", "RHS_2", and "RHS_3" accordingly.

$$\psi^{''} + \frac{\psi^{'}}{\rho} = \exp(\psi)(1-\Omega_e) - \exp\left(-\frac{\zeta\psi}{\tau}\right)(1-\Omega_i) = \text{RHS}_1 \tag{3.1}$$

$$A_z^{''} + \frac{A_z^{'}}{\rho} = -A_z\beta_e^2\left[\frac{t_{e1}\Omega_e}{1+t_{e1}}\exp(\psi) + \frac{\zeta t_{i1}\Omega_i}{1+t_{i1}}\exp\left(-\frac{\zeta\psi}{\tau}\right)\right] = \text{RHS}_2, \tag{3.2}$$

$$A_\phi^{''} + \frac{A_\phi^{'}}{\rho} - \frac{A_\phi}{\rho^2} = -A_\phi\beta_e^2\left[\frac{t_{e3}\Omega_e}{1+t_{e3}}\exp(\psi) + \frac{\zeta t_{i3}\Omega_i}{1+t_{i3}}\exp\left(-\frac{\zeta\psi}{\tau}\right)\right] = \text{RHS}_3 \tag{3.3}$$

3.1.1 Initial conditions for ψ

When ρ approaches zero, Eq.(3.1) implies

$$\psi(\rho \to 0) - \psi_0 = \frac{1}{4}\rho^2 \mathrm{RHS}_1(0), \tag{3.4}$$

or,

$$\psi \xrightarrow{\rho \to 0} \psi(0) + \left\{ \exp[\psi(0)][1 - \Omega_e(0)] - \exp\left[-\frac{\zeta\psi(0)}{\tau} \right][1 - \Omega_i(0)] \right\} \frac{\rho^2}{4} \tag{3.5}$$

where $\mathrm{RHS}_1(0)$ is the right hand side of the first differential equation at $\rho = 0$ with $\psi = \psi_0$, $A_z = A_{z0}$, and $A_\phi = A_{\phi 0}$.

Explicitly the relationship is

$$\begin{aligned}
\psi(\rho \to 0) &= \psi_0 + \frac{\rho^2}{4}\left[\exp(\psi)(1 - \Omega_e) - \exp\left(-\frac{\zeta\psi}{\tau} \right)(1 - \Omega_i) \right]_{\psi=\psi_0, A_z=A_{z0}, A_\phi=A_{\phi 0}} \\
&= \psi_0 + \frac{\rho^2}{4}\left[-\frac{h_{0e}}{\sqrt{2\xi_e + 1}} \exp\left(\psi_0 - \frac{A_{z0}^2 \xi_e}{2\xi_e + 1} \right) \right. \\
&\quad \left. + \frac{h_{0i}}{\sqrt{2\tau\xi_i + 1}} \exp\left(\psi_0 - \frac{A_{z0}^2 \zeta^2 \xi_i}{2\tau\xi_i + 1} \right) - \exp\left(-\frac{\zeta\psi_0}{\tau} \right) + \exp(\psi_0) \right].
\end{aligned} \tag{3.6}$$

The electrical potential should be cylindrically symmetric, thus $d\psi_0/d\rho = 0$. If a "electric potential bump" exists, electric potential should be a non-negative value near $\rho = 0$, then $\psi_0 > 0$. The value of $\psi_{0\max}$ could be determined by requiring $d^2\psi_0/d\rho^2 < 0$ in order for a localized solution to exist, and thus

$$\begin{aligned}
&\left[-\frac{h_{0e}}{\sqrt{2\xi_e + 1}} \exp\left(\psi_0 - \frac{A_{z0}^2 \xi_e}{2\xi_e + 1} \right) \right. \\
&\quad \left. + \frac{h_{0i}}{\sqrt{2\tau\xi_i + 1}} \exp\left(\psi_0 - \frac{A_{z0}^2 \zeta^2 \xi_i}{2\tau\xi_i + 1} \right) - \exp\left(-\frac{\zeta\psi_0}{\tau} \right) + \exp(\psi_0) \right] < 0.
\end{aligned} \tag{3.7}$$

That leads to the top boundary of ψ_0,

$$\psi_{0\max} = -\frac{\tau}{\zeta+\tau}\ln\left[-\frac{h_{0e}}{\sqrt{2\xi_e+1}}\exp\left(-\frac{A_{z0}^2\xi_e}{2\xi_e+1}\right)+\frac{h_{0i}}{\sqrt{2\tau\xi_i+1}}\exp\left(-\frac{A_{z0}^2\zeta^2\xi_i}{2\tau\xi_i+1}\right)+1\right]. \tag{3.8}$$

Therefore the initial range of ψ_0 is

$$\boxed{0<\psi_0<-\frac{\tau}{\zeta+\tau}\ln\left[-\frac{h_{0e}}{\sqrt{2\xi_e+1}}\exp\left(-\frac{A_{z0}^2\xi_e}{2\xi_e+1}\right)+\frac{h_{0i}}{\sqrt{2\tau\xi_i+1}}\exp\left(-\frac{A_{z0}^2\zeta^2\xi_i}{2\tau\xi_i+1}\right)+1\right]} \tag{3.9}$$

If a "electric potential hole" exists, then the initial range of ψ_0 is,

$$\boxed{0>\psi_0>-\frac{\tau}{\zeta+\tau}\ln\left[-\frac{h_{0e}}{\sqrt{2\xi_e+1}}\exp\left(-\frac{A_{z0}^2\xi_e}{2\xi_e+1}\right)+\frac{h_{0i}}{\sqrt{2\tau\xi_i+1}}\exp\left(-\frac{A_{z0}^2\zeta^2\xi_i}{2\tau\xi_i+1}\right)+1\right]} \tag{3.10}$$

The second derivative of ψ could be computed by taking the second derivative of equation (3.6)

$$\psi''(\rho\to 0)=\lim_{\rho\to 0}\frac{\psi'(\rho\to 0)-\psi_0'}{\rho} \tag{3.11}$$

Explicitly,

$$\boxed{\psi_0''=\frac{1}{2}\left[\exp(\psi_0)(1-\Omega_{e0})-\exp\left(-\frac{\zeta\psi_0}{\tau}\right)(1-\Omega_{i0})\right]} \tag{3.12}$$

3.1.2 The asymptotic line of $\psi(\rho\to\infty)$

In the previous subsection all three initial conditions of ψ: ψ_0, ψ_0', and ψ_0'' are discussed. Our solutions, the asymptotic behavior at large ρ is also required. Electrical potential is required to be zero when radial distance apporaches infinity to have a localized structure. Thus the boundary condition of ψ at infinity is

$$\psi(\rho\to\infty)=0. \tag{3.13}$$

Specifically, an asymptotic expression of ψ can be derived. For large value of ρ, $\Omega_e \to 0$ and $\Omega_i \to 0$, since A_ϕ is proportional to ρ asymptotically as we will show in Subsection 3.3.2. The first differential equation becomes

$$\psi'' + \frac{\psi'}{\rho} = \exp(\psi) - \exp\left(-\frac{\zeta\psi}{\tau}\right) \approx k^2\psi, \tag{3.14}$$

where $k^2 = 1 + \zeta/\tau$ is a constant. The form above is known as the modified Bessel function and the solution is

$$\psi(\rho \to \infty) = \psi_\infty K_0(k\rho) = \psi_\infty \sqrt{\frac{\pi}{2k\rho}} \exp(-k\rho) \tag{3.15}$$

where ψ_∞ is a constant. The derivative of ψ at inifinty could also be computed

$$\psi'(\rho \to \infty) = -\psi_\infty \sqrt{\frac{\pi}{2k\rho}} \left[\frac{1}{2\rho} + k\right] \exp(-k\rho) \tag{3.16}$$

3.2 Boundary Conditions for A_z

3.2.1 Initial conditions for A_z

The initial conditions for A_z can be computed through similar processes. By integrating the second ordinary differential equation twice, the equation becomes

$$\int_0^\rho \frac{1}{\rho} d\rho \int_0^\rho \rho d\rho \left(A_z^{''} + \frac{A_z^{'}}{\rho}\right) = \int_0^\rho \frac{1}{\rho} d\rho \int_0^\rho d\rho \left[\frac{d}{d\rho}\left(\rho \frac{dA_z}{d\rho}\right)\right] = A_z(\rho) - A_z(0) = A_z(\rho) - A_{z0}, \tag{3.17}$$

which leads to a similar expression

$$A_z\Big|_{\rho\to 0} - A_{z0} = A_z(\rho \to 0) - A_{z0} = \frac{1}{4}\rho^2(\mathrm{RHS2}_0). \tag{3.18}$$

Again the subscript "0" here indicates all the expresion is evaulated at $\psi = \psi_0$, $A_z = A_{z0}$, and $A_\phi = A_{\phi 0}$. Explicitly,

$$A_z(\rho \to 0) = A_{z0}\left\{1 - \frac{\rho^2\beta_e^2}{4}\left[\frac{t_{e10}\Omega_{e0}}{1+t_{e10}}\exp(\psi_0) + \frac{\zeta t_{i10}\Omega_{i0}}{1+t_{i10}}\exp\left(-\frac{\zeta\psi_0}{\tau}\right)\right]\right\}. \tag{3.19}$$

Thus the initial value of A_z is an arbitrary number. It is one of the input values in the numerical process

$$\boxed{A_z(\rho \to 0) = A_{z0}.} \tag{3.20}$$

The initial derivative of A_z is zero by the symmetry of ϕ component of magnetic field

$$\boxed{A'_{z0} = \frac{dA_z(0)}{d\rho} = 0.} \tag{3.21}$$

The second derivative of A_z could be derived by substituting A_{z0} and A'_{z0} into the second differential equation. For small ρ, the second differential equation becomes

$$A_z^{''}(\rho \to 0) + \frac{A_z^{'}}{\rho}(\rho \to 0) = -A_z\beta_e^2\left[\frac{t_{e10}\Omega_{e0}}{1+t_{e10}}\exp(\psi_0) + \frac{\zeta t_{i10}\Omega_{i0}}{1+t_{i10}}\exp\left(-\frac{\zeta\psi_0}{\tau}\right)\right] = -k_z^2 A_z, \tag{3.22}$$

where,

$$k_z^2 = \beta_e^2\left[\frac{t_{e10}\Omega_{e0}}{1+t_{e10}}\exp(\psi_0) + \frac{\zeta t_{i10}\Omega_{i0}}{1+t_{i10}}\exp\left(-\frac{\zeta\psi_0}{\tau}\right)\right]. \tag{3.23}$$

The equation reduced to a bessel function ($A''_z + A'_z/\rho = -k_z^2 A_z$) at small ρ, and the solution has the form

$$A_z(\rho \to 0) = A_{z0}J_0(k_z\rho) \approx \left(1 - \frac{k_z^2\rho^2}{4}\right)A_{z0}. \tag{3.24}$$

The second derivative of A_{z0} could also be computed

$$\boxed{A''_{z0} = -\frac{k_z^2 A_{z0}}{2}}. \tag{3.25}$$

3.2.2 The asymptotic line of $A_z(\rho \to \infty)$

When ρ is large, the relationship derived from equation (3.21) still holds

$$\begin{aligned} A_z\Big|_{\rho=\infty} - A_{z0} &= -\ln(\rho)\left[\int_0^\infty \rho d\rho(\text{RHS2})\right] + \int_0^\infty d\rho\rho[\ln(\rho)(\text{RHS2})] \\ \Rightarrow A_z(\rho \to \infty) &= A_{z0} - \ln(\rho)\left[\int_0^\infty \rho d\rho(\text{RHS2})\right] + \int_0^\infty d\rho\rho[\ln(\rho)(\text{RHS2})]. \end{aligned} \tag{3.26}$$

The two definite integrals converge and the answers of them could be called "C_1" and "C_2". The asymptotic line of A_z is

$$A_z(\rho \to \infty) = C_1 \ln(\rho) + C_2. \tag{3.27}$$

The constant "C_1" could be related to $\hat{\phi}$ component of magnetic field. Noticed that in cylindrical coordinate, since vector potential depends on the radial distance ρ only, the magnetic field could be written as

$$\mathbf{B} = \nabla \times \mathbf{A} = -\frac{\partial A_z}{\partial \rho}\hat{\phi} + \frac{1}{\rho}\left[\frac{\partial(\rho A_\phi)}{\partial \rho}\right]\hat{z}. \tag{3.28}$$

The asymptotic behaviour of B_ϕ when ρ approaches inifinity is

$$B_\phi(\rho \to \infty) = -\frac{\partial}{\partial \rho}[C_1 \ln(\rho) + C_2] = -\frac{C_1}{\rho}. \tag{3.29}$$

Thus C_1 could be computed from the $\hat{\phi}$ component of magnetic field at large ρ. This formula is used as an initial guess of A_z in an iteration method to be introduced in Section 3.4.

3.3 Boundary Conditions for A_ϕ

3.3.1 Initial condition for A_ϕ

Again, a similar process will be implemented for computing the boundary conditions of A_ϕ. The result is slightly different since the left hand side is different.

$$\frac{1}{\rho}\int_0^\rho \rho d\rho \int_0^\rho d\rho\left(A''_\phi + \frac{A'_\phi}{\rho} - \frac{A_\phi}{\rho}\right) = \frac{1}{\rho}\int_0^\rho d\rho\rho\left[\frac{1}{\rho}\frac{d(\rho A_\phi)}{d\rho}\right]_0^\rho = A_\phi(\rho) - 2\frac{dA_{\phi 0}}{d\rho}, \tag{3.30}$$

where we have used the fact that $A_\phi(0) = 0$ by the requirement of a non-singular magnetic field, and that

$$\left[\frac{1}{\rho}\frac{d(\rho A_\phi)}{d\rho}\right]_0^\rho = \left(\frac{A_\phi}{\rho} + \frac{dA_\phi}{d\rho}\right) - \left(\frac{A_\phi}{\rho} + \frac{dA_\phi}{d\rho}\right)_{\rho=0}. \tag{3.31}$$

The first term can be combined as $d(\rho A_\phi)/(\rho d\rho)$. Since it is known that $A_{\phi 0} = 0$,

$$\left.\frac{dA_\phi}{d\rho}\right|_{\rho=0} = \lim_{\rho\to 0}\frac{A_\phi - A_{\phi 0}}{\rho - 0} = \lim_{\rho\to 0}\frac{A_\phi - 0}{\rho - 0} = \lim_{\rho\to 0}\frac{A_\phi}{\rho} = \left.\frac{A_\phi}{\rho}\right|_{\rho=0} \tag{3.32}$$

Thus equation (3.34) could be further simplified into the following form

$$\left[\frac{1}{\rho}\frac{d(\rho A_\phi)}{d\rho}\right]_0^\rho = \frac{d(\rho A_\phi)}{\rho d\rho} - 2\left.\frac{dA_\phi}{d\rho}\right|_{\rho=0} = \frac{d(\rho A_\phi)}{\rho d\rho} - 2\frac{dA_{\phi 0}}{d\rho}. \tag{3.33}$$

Then, it can be shown that the initial condition of A_ϕ is of the form of

$$A_\phi(\rho\to 0) = \frac{dA_{\phi 0}}{d\rho}\rho + \frac{1}{5!}\frac{d^5 A_{\phi 0}}{d\rho^5}\rho^5 + O(\rho^6). \tag{3.34}$$

From equation (3.31), the $\hat{z}$ component of magnetic field is

$$B_z(\rho\to 0) = 2\frac{dA_{\phi 0}}{d\rho} + \frac{6}{5!}\frac{d^5 A_{\phi 0}}{d\rho^5}\rho^4 \approx B_{z0}, \tag{3.35}$$

or,

$$\boxed{\frac{dA_{\phi 0}}{d\rho} = \frac{B_{z0}}{2}} \tag{3.36}$$

3.3.2 Asymptotic line of $A_\phi(\rho \to \infty)$

At large ρ the asymptotic line of A_ϕ is

$$\begin{aligned} A_\phi(\rho \to \infty) &= \left[\frac{dA_{\phi 0}}{d\rho}\rho - \frac{1}{\rho}\int_0^\rho \rho d\rho \int_0^\rho d\rho(\text{RHS3})\right]_{\rho\to\infty} \\ &= \left[\frac{dA_{\phi 0}}{d\rho} - \frac{1}{2}\int_0^\infty d\rho(\text{RHS3})\right]\rho. \end{aligned} \tag{3.37}$$

The $\hat{z}$ component of magnetic field could also be determined

$$B_z \xrightarrow{\rho\to\infty} B_{z0} - \int_0^\infty J_\phi d\rho \equiv B_{z\infty} \tag{3.38}$$

where $B_{z\infty}$ is a constant.

3.4 The Implementation of Algorithms

3.4.1 Adaptive stepsize runge kutta method

The three coupled second order ordinary differential equations could be rearranged into six coupled first order ordinary differential equations. The original differential equations can be writen as

$$\begin{aligned} \psi'' + \frac{\psi'}{\rho} &= \text{RHS}_1, \\ A_z'' + \frac{A_z'}{\rho} &= \text{RHS}_2, \\ A_\phi'' + \frac{A_\phi'}{\rho} - \frac{A_\phi}{\rho^2} &= \text{RHS}_3. \end{aligned} \tag{3.39}$$

where "RHS" are the corresponding right hand sides of the equations. Let $\rho = x$, $\psi = y_1$, $\psi' = y_2$, $A_z = y_3$, $A'_z = y_4$, $A_\phi = y_5$, and $A'_\phi = y_6$, the three equations now become

$$\begin{aligned}
y'_1(x) &= y_2(x) \\
y'_2(x) &= \mathrm{RHS}_1 - \frac{y_2(x)}{x} \\
y'_3(x) &= y_4(x) \\
y'_4(x) &= \mathrm{RHS}_2 - \frac{y_4(x)}{x} \\
y'_5(x) &= y_6(x) \\
y'_6(x) &= \mathrm{RHS}_3 - \frac{y_6(x)}{x} + \frac{y_5(x)}{x^2}.
\end{aligned} \tag{3.40}$$

Keep in mind that the right hand sides "$\mathrm{RHS}_{1,2,3}$" are not constants, they are functions of x and $\mathbf{y} = (y_1, \cdots, y_6)$ as well ($\mathrm{RHS}_{1,2,3} = \mathrm{RHS}_{1,2,3}(x, \mathbf{y})$). Generally, we are looking for the numerical solutions to a system of equations in the following form

$$\mathbf{y}' = f(x, \mathbf{y}). \tag{3.41}$$

This type of ODE problems could be well handled through the adaptive stepsize Runge Kutta method offered by *Numerical Recipes* [Press et al., 1992]. The advantage of the algorithm is that for each step of the numerical integration, a forth order Runge Kutta method and a fifth order Runge Kutta method will be appplied simultaneously. The result from the 5th RK method will be considered as the "true" solution, and the difference between the 4th RK method and the 5th RK method will be used to adjust the stepsize of the numerical integration. If the difference is beyond a certain tolerance the stepsize will be reduced, and if the difference is negligible the stepsize will be enlarged.

3.4.2 Formula translations

The entire solver for the two dimensional BGK mode (which will be referred to as the BGK2D-solver in the following text) is implemented through modern Fortran. The whole program includes

four essential modules: (1) The numerical integration module that wraps the adaptive stepsize Runge Kutta method into a derived type, (2) The formula translation module that includes the six first order ODEs, (3) A core solver module that solves the system of equations for ψ, A_z, and A_ϕ, and (4) A full-fledged solver that outputs all the necessary information including number densities, magnetic fields, bulk velocities, currents, and temperatures of the system.

First of all, a module that defines the double-precision floating-point format is required. For the purpose of compatibility, it is recommended to use the intrinsic module `iso_fortran_env` and define the type `real64` as an integer parameter.

real.f90

```
module real_m
    use, intrinsic :: iso_fortran_env, only: real64
    implicit none
    integer, parameter :: real_t = real64
end module real_m
```

In order to apply the adaptive runge kutta method flexibly, an abstract derived-type `runge_kutta_t` is constructed. A derived type in Fortran is essentially a C++ class. By constructing a numerical method into a derived type one can easily apply the method by using the type from other modules or extending it to a new type. This is extremely useful since the adaptive stepsize Runge Kutta method is used multiple times in the solver with different initialization setups. The details of the subroutine `rkqs_sub` is not shown here but could be found in chapter 16 in *Numerical Recipes*.

runge_kutta.f90

```
module runge_kutta_m
    use real_m
    implicit none

    type, abstract, public :: runge_kutta_t
        real(real_t) :: eps
        real(real_t), dimension(:), pointer :: yscal
    contains
        procedure :: runge_kutta_init => runge_kutta_init_sub
        procedure :: rkck => rkck_sub
        procedure :: rkqs => rkqs_sub
        procedure(derivsx), deferred :: derivs
    end type

    abstract interface
```

```
        subroutine derivsx(this, x, y, dydx)
            use real_m
            import :: runge_kutta_t
            implicit none
            class(runge_kutta_t) :: this
            real(real_t), intent(in) :: x, y(:)
            real(real_t), intent(out) :: dydx(:)
        end subroutine derivsx
    end interface

    private :: runge_kutta_init_sub, rkck_sub, rkqs_sub

contains
    ...
end module runge_kutta_m
```

The construction of the system of the ODEs is practiced in the module `bgk2d_eqn.f90`. In the module, an extend user-derived type `bgk2d_eqn_t` is created. The advantage of writing the equations into an extend derived type is that all the properties of its parent type, which is the type `runge_kutta_t` are directly inherited. In other words, the Runge Kutta method is bounded to the system of the ODEs. As long as the equations are initialized, the Runge Kutta method will also be initialized and ready to be applied.

bgk2d_eqn.f90

```
module bgk2d_eqn_m
    use real_m
    use runge_kutta_m
    implicit none

    type, public, extends(runge_kutta_t) :: bgk2d_eqn_t
        real(real_t) :: zeta, tau, be2, h0_e, h0_i, xi_e, xi_i, k_e, k_i
    contains
        procedure :: eqn_init => eqn_init_sub
        procedure :: te => te_sub
        procedure :: ti => ti_sub
        procedure :: omega => omega_sub
        procedure :: rhs => rhs_sub
        procedure :: derivs => derivs_sub
    end type bgk2d_eqn_t

    private :: te_sub, ti_sub, omega_sub, rhs_sub, derivs_sub

contains

    ......

    subroutine derivs_sub(this, x, y, dydx)
        class(bgk2d_eqn_t) :: this
        real(real_t), intent(in) :: x, y(:)
```

```
        real(real_t), intent(out) :: dydx(:)
        real(real_t) :: rhs(3)

        call rhs_sub(this, x, y, rhs)
        dydx(1) = y(2)
        dydx(2) = rhs(1) - y(2) / x
        dydx(3) = y(4)
        dydx(4) = rhs(2) - y(4) / x
        dydx(5) = y(6)
        dydx(6) = rhs(3) - y(6) / x + y(5) / x**2
    end subroutine derivs_sub

end module bgk2d_eqn_m
```

3.4.3 The bisection method and the shooting method

The adaptive stepsize Runge Kutta method introduced could solve the set of differential equations mathematically. However, not all the solutions are physically possible. The solution of electric potential ψ must converge to zero at infinity ($\psi(\rho \to \infty) = 0$). The *shooting method* is used here to filter all the divergent solutions. In the case of "Electron BGK-mode with finite ion temperature" (discussed in Section 2.3.2), initial value of electric potential (ψ_0) lies between zero and $\psi_{0\max}$ (discussed in Section 3.1.1). When the maximum value of ψ_0 is used to integrate all equations the solution of ψ diverges and goes to infinity, and when the minimum value of ψ_0 is chosen the solution diverges and goes to negative infinity. Then, a middle value $\psi_{0\max}/2$ is used as ψ_0. If the solution integrated diverges to positive infinity, the initial value ψ_0 will be used as the next upper boundary, and if it diverges to negative infinity, it will be treated as the next lower boundary. This *bisection method* will be kept using until the solution of ψ converges to zero at large distance or a certain tolerance is reached. The diagram below shows the first four iterations of this method.

These ideas are included in module `eqn_solver_m` of the BGK2D-solver. The bisection method is implemented through the logical function `binary_search_sub`. In the function, two logical input variables `jud1` and `jud2` are used to determine whether the solution diverges to positive infinity or negative inifinity. If `jud1` is true, then the original "middle" value becomes the upper boundary. If `jud2` is true, then the original "middle" value becomes the lower boundary. The logical function is always `.true.` if one of the conditions is satisfied.

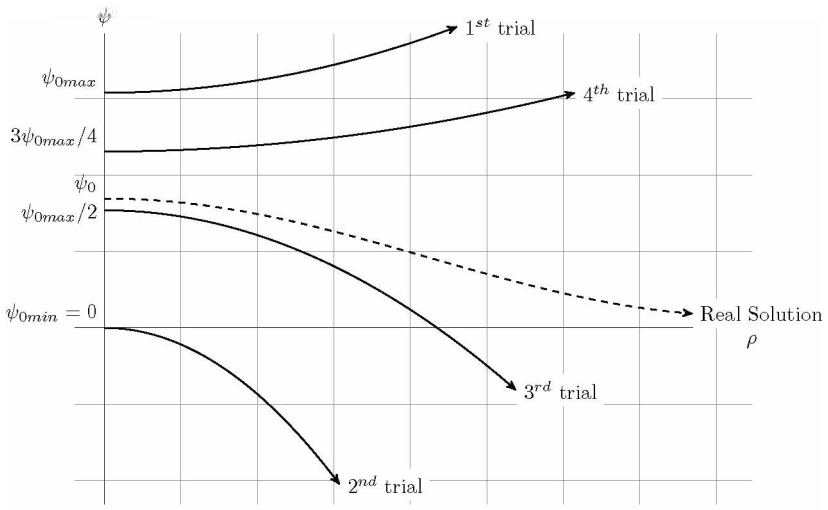

Figure 3.1: A demonstration of the first four trials of the numerical integration

The other subroutine `try_solve_sub` presented here is a wrapper of the adaptive stepsize Runge Kutta method and bisection method. The initial values of the ODEs (`y`) are generated through two subroutines `compute_y0_sub` and `compute_y1_sub`. For each iteration in the loop `loop_21`, the solver will integrate one step further, and the function `binary_search_sub` will judge whether the solution to the equation satisfies the converging requirement. If the maximum steps are reached or the solution indeed converges to a very small number, the iteration stops. The code snippet below demonstrates the derived type `eqn_solver_t`, the type bound function `binary_search_sub` and the type bound subroutine `try_solve_sub`. The other details of the module are less important and thus are not presented here.

eqn_solver.f90

```
module eqn_solver_m
    use real_m
    use bgk2d_eqn_m
    implicit none

    type, public :: eqn_solver_t
        real(real_t) :: zeta, tau, be2
        real(real_t) :: h0_e, h0_i, xi_e, xi_i, k_e, k_i
        real(real_t) :: b0, az0
        real(real_t) :: eps, x0, h0
        type(bgk2d_eqn_t), pointer :: bgk2d_eqn_p
    contains
        procedure :: eqn_init  => eqn_initialize_sub
        procedure :: try_slv   => try_solve_sub
        procedure :: quick_slv => quick_solve_sub
        procedure :: get_psi0  => compute_psi0_sub
```

```
    end type eqn_solver_t

    ......

contains

    ......

    logical function binary_search_sub(jud1, jud2, upper, lower, mid)
        logical, intent(in) :: jud1, jud2
        real(real_t), intent(inout) :: upper, lower, mid

        binary_search_sub = .false.
        if ( jud1 ) then
            upper = mid
            mid = 0.5_real_t * ( upper + lower )
            binary_search_sub = .true.
        else if ( jud2 ) then
            lower = mid
            mid = 0.5_real_t * ( upper + lower )
            binary_search_sub = .true.
        end if
    end function binary_search_sub

    subroutine try_solve_sub( &
        this, psi0_u, psi0_l, psi0, h, x, y, n, y0_out &
    )
        class(eqn_solver_t) :: this
        real(real_t), intent(inout) :: psi0, psi0_u, psi0_l
        real(real_t) :: h, x, y(neq)
        integer, intent(out) :: n
        real(real_t), intent(out), optional :: y0_out(neq)
        real(real_t) :: hdid, hnext, y0(neq), dydx(neq), psi0_old
        logical :: jud1, jud2, bin_srch
        real(real_t), parameter :: zero = tiny(0._real_t)

        loop_11: do
            psi0_old = psi0
            call compute_y0_sub(this, psi0, y0)
            call compute_y1_sub(this, y0, y)
            h = this%h0; x = this%x0
            n = 1
            loop_21: do
                call this%bgk2d_eqn_p%derivs( &
                    x, y, dydx &
                )
                call this%bgk2d_eqn_p%rkqs( &
                    y, dydx, x, h, hdid, hnext &
                )
                h = hnext

                call generate_condition_sub( &
                    this, psi0, y(1), jud1, jud2 &
                )
                bin_srch = binary_search_sub( &
                    jud1, jud2, psi0_u, psi0_l, psi0 &
```

```
                )
                if ( bin_srch ) exit loop_21
                n = n + 1
                if ( n > nmax - 1 ) exit loop_21
            end do loop_21
            if ( abs( psi0_old - psi0 ) < zero ) exit loop_11
        end do loop_11

        if ( present(y0_out) ) then
            call compute_y1_sub(this, y0, y0_out)
        end if
    end subroutine try_solve_sub
    ...
end module eqn_solver_m
```

Finally, a simple application to the BGK2d-solver is given in the code `text.f90` below. In order to numerically solve the equations, the parameters of the equations, namely `zeta`, `tau`, `be2`, `h0_e`, `h0_i`, `xi_e`, `xi_i`, `k_e`, `k_i`, and the initial values of the equations, `b_0`, `az0` have to be initialized first. Other numerical parameters, the initial independent variable `x0`, the initial stepsize `h0`, and the tolerance of truncation error `eps` are also assigned. Then the system of the equations could be numerically solved by calling the procedure `quick_slv` that is bounded to a pointer `eqn_solver_p` which points to a user-defined type `eqn_solver_t`.

test.f90

```
program test
    use real_m
    use bgk2d_solver_m
    implicit none

    real(real_t), parameter :: zeta = 5.4461702e-04_real_t
    real(real_t) :: be2  = 1.e-6_real_t
    real(real_t) :: b0   = 1._real_t,  az0  = 1._real_t
    real(real_t) :: xi_e = 0._real_t,  xi_i = 0._real_t
    type(eqn_solver_t), pointer :: eqn_solver_p

    test_01: block
        real(real_t) :: tau  = 1.e10_real_t
        real(real_t) :: h0_e = 0.1_real_t,  h0_i = 0._real_t
        real(real_t) :: k_e  = 1._real_t,   k_i  = 0._real_t
        real(real_t), parameter :: eps  = 1.e-16_real_t
        real(real_t) :: h0 = eps, x0 = eps
        real(real_t), dimension(nmax) :: hn, xn, yn(neq, nmax)
        integer :: n

        print *, "Test 01: Test try_solve_sub"
        allocate(eqn_solver_p)
        call eqn_solver_p%eqn_init( &
            zeta, tau, be2, &
```

```
            h0_e, h0_i, xi_e, xi_i, k_e, k_i, &
            b0, az0, eps, x0, h0 &
        )
        call eqn_solver_p%quick_slv(hn, xn, yn, n)

        print *, xn(n), yn(1, n), n
    end block test_01

end program test
```

Chapter 4

Numerical Results

Based on the theories derived from Chapter 2 and numerical methods developed from Chapter 3, numerical solutions of the equation set are demonstrated in this chapter. Three different cases: (1) The electron cases, (2) the ion cases, and (3) the electron-ion cases presented in this chapter. Each part will be analyzed with two different logics: case studies and parameter scans. A case study where all the parameters of the three differential equations (ζ, τ, h_{0e}, h_{0i}, ξ_e, ξ_i, k_e, and k_i) are fixed usually contains five portions: (1) An introduction to the parameter set and why the set is chosen; (2) Diagrams and explanations of the solutions to the ODEs; (3) Diagrams and explanations of the selected physical properties; (4) Explanations of contour plots of velocity distributions; and (5) A brief summary. A parameter scan where only one of all the parameters are variable includes three parts: (1) Explanation of the changing parameter; (2) diagrams of the parameter scan; and (3) Importance of the results.

4.1 Electron BGK Mode With Finite Ion Temperature

4.1.1 Reproduction of an ideal case

We will start this chapter by reproducing one of the cases in [Ng et al., 2006] under the assumption of a uniform ion background.

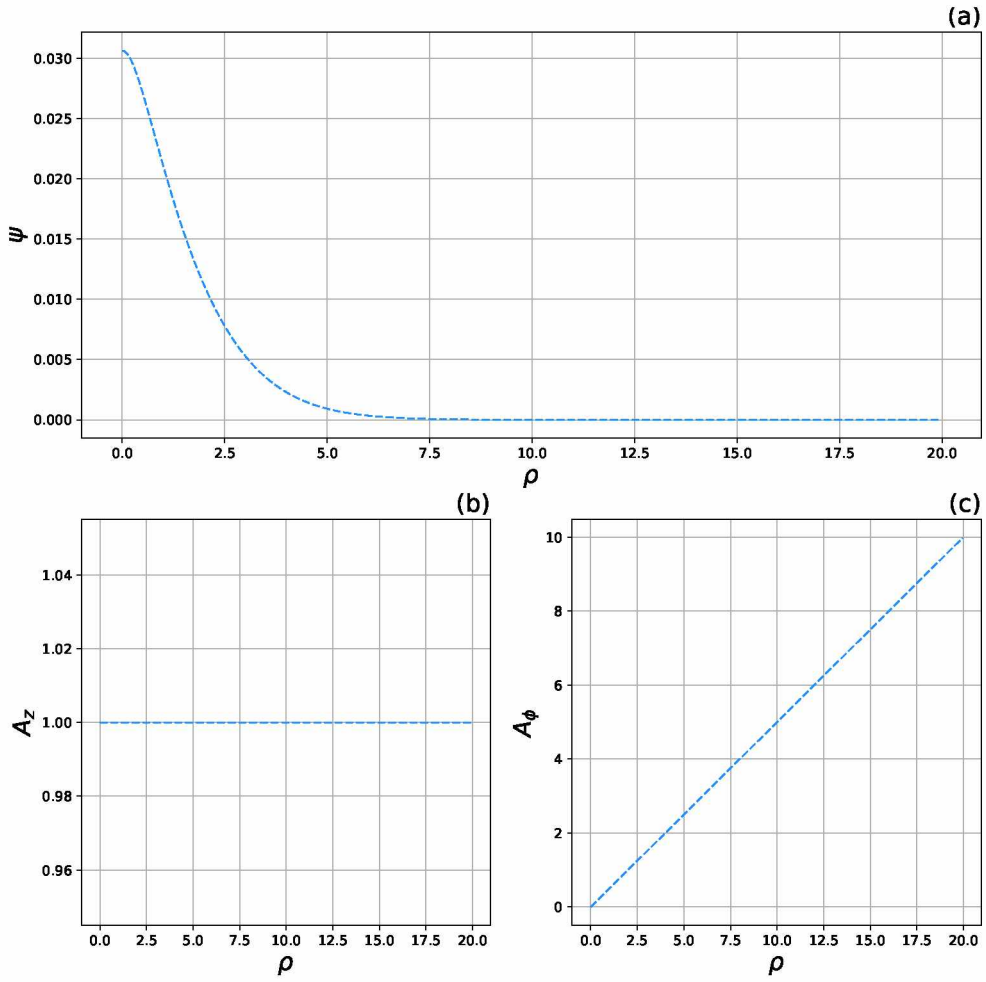

Figure 4.1: Numerical solution of (a) electric potential ψ, (b) $\hat{z}$ component of vector potential A_z, and (c) $\hat{\phi}$ component of vector potential A_ϕ with $h_{0e} = 0.1$, $k_e = 1$, $\xi_e = 0$, $h_{0i} = 0$, $k_i = 0$, $\xi_i = 0$, $\zeta = 1$, $\tau = 10^{10}$, $\beta_e = 10^{-5}$, $B_{z0} = 1$ and $A_{z0} = 1$.

First let us recall the electron and ion distribution functions derived in Chapter 2:

$$f_e(w_e, l_e, p_e) = (2\pi)^{-3/2} \exp(-w_e)[1 - h_{0e} \exp(-k_e l_e^2 - \xi_e p_e^2)], \tag{4.1}$$

$$f_i(w_i, l_i, p_i) = (2\pi\tau)^{-3/2} \exp(-w_i \zeta/\tau)[1 - h_{0i} \exp(-k_i l_i^2 - \xi_i p_i^2)]. \tag{4.2}$$

To recover a uniform ion background, the parameter τ, which is the square of the ratio between the thermal velocities of ions and electrons, must be a large number ($\tau = v_i^2/v_e^2 \gg 1$). The value of h_{0i} is set to be zero so that the contribution of ion kinetic effect is almost negligible. In such a case, the choice of k_i and ξ_i is irrelevant. The influence of electron velocity distribution to the

system is manifested. In the following part of this chapter, all the cases that $h_{0i} = 0$ are referred to as the "electron cases" and the cases when $h_{0e} = 0$ are called the "ion cases".

The diagram in Figure 4.1 demonstrates the solutions to the system of the ODEs. Except for the values of τ and h_{0i} mentioned in the previous paragraph, all the other parameters are set to be the same as in [Ng et al., 2006]. Notice here the quantities ψ, A_z, and A_ϕ are dimensionless as discussed before, and $\bar{A}_\phi$.

These solutions to the equations could be well explained by the "taken-out" scenario mentioned in Section 2.3. If the "center" is defined where $\rho = 0$ and the "central region" is the region where ρ is small. Electrons are missing in the central region. Without the negative charges, the electric potential ψ in the central region becomes positive. The potential decreases and converges to zero as radius ρ increases. Be aware that although it seems the electric potential converges to zero at around $\rho = 8$, it does not converge to zero until $\rho = \infty$. This phenomenon matches the asymptotic line of the electric potential derived in Chapter 3. Since no axial current density is given to the electrons ($\xi_e = 0$), the vector potential A_z remains the same. The value of A_ϕ is linear as the distance increases, which is also consistent with the relationship presented in Chapter 3.

Furthermore, significnat properties are also plotted (Figure 4.2) to explain the physical picture behind the solutions. Figure 4.2(a) shows the $\hat{z}$-component of magnetic field. The $\hat{z}$-component of the magnetic field at the origin (B_{z0}) is set to be one in this case. The scale of the change of the magnetic field is very small (in a magnitude of 10^{-8}) comparing to B_{z0}, using $\beta_e = 10^{-5}$. However a "bump" of magnetic field could still be easily observed from the diagram.

The density ratio of electrons (n_e/n_{e0}) is shown in part (b). A density hole in the central region is clearly seen and it matches the "taken-out" scenario. Aside from the density hole in the center, a density bump at approximately $\rho = 2.4$ showing where most of the electrons taken out are located. Since the electron rotate around the center, a non-zero $\hat{\phi}$ component of electron bulk velocity $v_{e\phi}$ at around $\rho = 2.4$ and a current density with opposite direction at the same location are also observed (Figure 4.2 (c) and (d)). The positive current density J_ϕ will enhance the magnetic field by Ampère's Law. This is consistent with the magnetic bump shown in part(a).

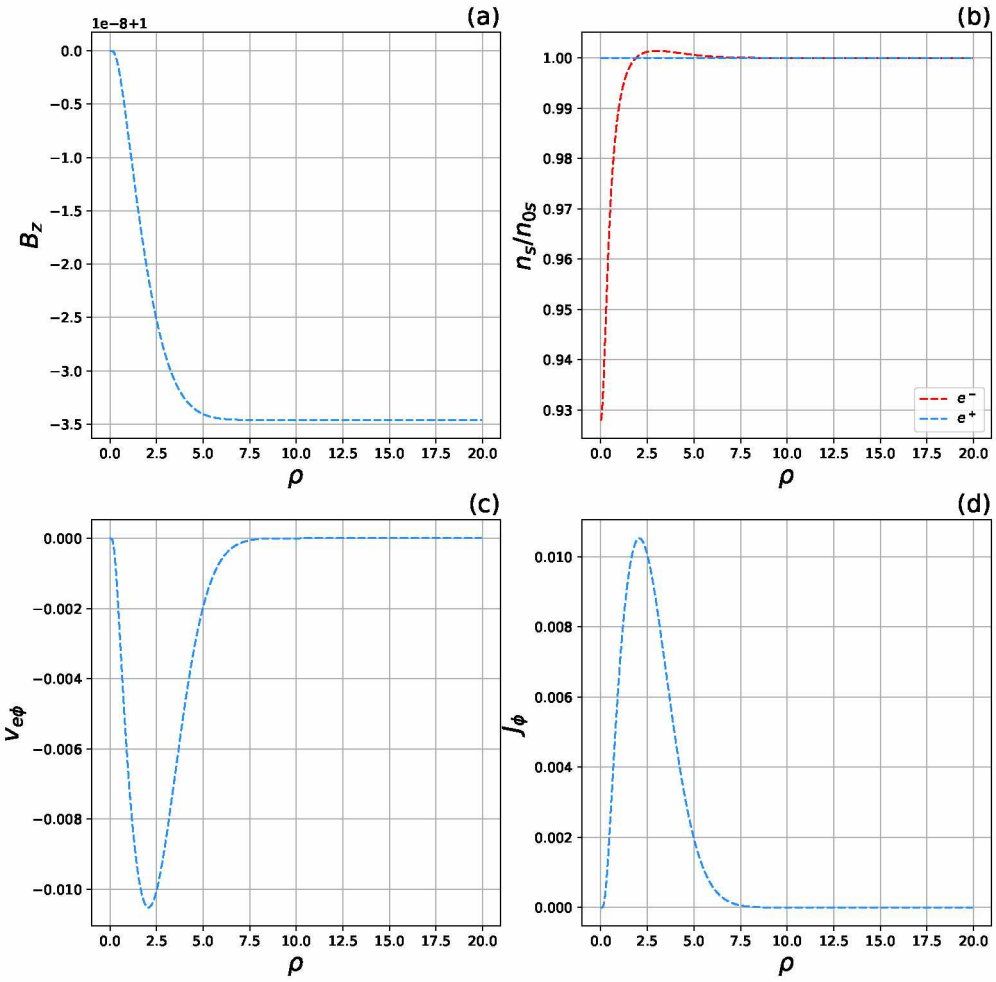

Figure 4.2: Numerical solution of (a) $\hat{z}$-component of magnetic field, (b) density ratio of electrons and ions, (c) $\hat{\phi}$ component of electron velocity, and (d) $\hat{\phi}$ component of current with $h_{0e} = 0.1$, $k_e = 1$, $\xi_e = 0$, $h_{0i} = 0$, $k_i = 0$, $\xi_i = 0$, $\zeta = 1$, $\tau = 10^{10}$, $B_{z0} = 1$ and $A_{z0} = 1$.

To check the consistency of the solutions, one more set of plots can be demonstrated. With a fixed radial velocity ($v_\rho \equiv$ const), a phase space contains v_ϕ, v_z and ρ could be constructed. For each set of (v_ϕ, v_z, ρ) there exists an electron and an ion velocity distribution function. Thus, by cutting the "cube" along different axes, three types of contour plots could be plotted.

Figure 4.3 is a demonstration of the contour plots. Part (a) is a cut at $\rho = 2.4$, where in Figure 4.2(d) the peak of current appears. If the electron velocity distribution function is a Boltzmann distribution, the contour plot of v_z vs. v_ϕ should be concentric circles. Clearly the contours ploted in part (a) are not concentric circles. The circles are "shrivelled" at around $v_\phi = 1.0$. The difference between this specific distribution function and the Boltzmann distribution function

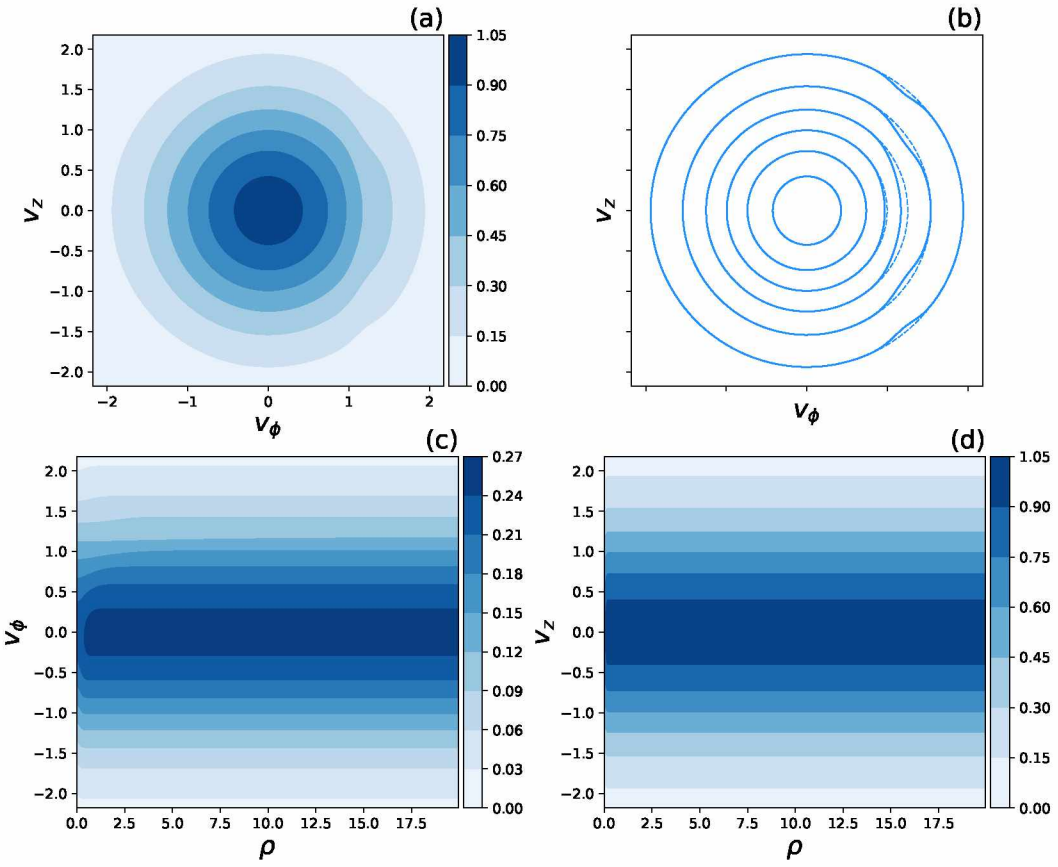

Figure 4.3: (a) Contour plot of the electron distribution function in the v_z-v_ϕ space at $\rho = 2.4$, (b) difference between (a) and the Boltzmann distribution function (represented by dashed lines), (c) contour plot in the v_ϕ-ρ space at $v_z = 2.4$, and (d) contour plot in the v_z-ρ space at $v_\phi = 10$. The color bar indicates the value of electron velocity distribution function.

is shown in part(b). This phenomenon could also be observed in part (c), where asymmetric distributions appear at around $\rho = 2.4$. These contour plots implies there are more electrons rotating around the center with a negative velocity. As a result, the bulk velocity of electrons should be negative in the ϕ direction. This is consistent with the results shown in Figure 4.2. Notice the $V_{e\phi}$ plotted in Figure 4.2 is the $\hat{\phi}$ component of the bulk velocity, yet the V_ϕ in Figure 4.3 is the $\hat{\phi}$ component of the velocity of a single particle.

4.1.2 An electron case with a positive h_{0e}

In the first subsection a very ideal case is analyzed. Let us move on and discuss a more realistic case. Before solving the system of ODEs there are few parameters required to be tuned.

Recall the definition of ζ from charpter two:

$$\zeta = \frac{m_e}{m_i} Z_i \tag{4.3}$$

where m_i and m_e are the mass of an ion and the mass of an electron. The value Z_i represents the atomic number of the ion. If only Hydrogen ions are considered, then $Z_i = 1$. The value of ζ could be calculated as $\zeta = m_e/m_i \approx 5.44617 \times 10^{-4}$. Thus, the parameter ζ can be considered as a constant and will be used in all the following case studies.

The value of τ is defined as $\tau = v_i^2/v_e^2$. It could be rewritten as a function of ζ:

$$\tau = \frac{v_i^2}{v_e^2} = \frac{m_e}{m_i} \frac{m_i v_i^2}{m_e v_e^2} = \zeta \frac{T_i}{T_e} \tag{4.4}$$

If electron temperature and ion temperature are equal to each other, it is obvious that $\tau = \zeta$.

Another important parameter that requires tweaking is $\beta_e^2 = v_e^2/c^2$. Since the equation systems is derived non-relativistically, the value of β_e has to be a lot less than one. In this specific case, β_e is chosen to be $\beta_e = 1 \times 10^{-5}$.

The solutions to this electron case are shown in the figure above (Figure 4.4). From a quick comparison with Figure 4.1 it is not difficult to tell the solutions of A_z and A_ϕ stays identical with different values of τ. The solutions of electric potential ψ are different. With smaller value of τ, the initial electric potential ψ_0 decreases and the electric potential tends to zero more rapidly.

The decrease of electric potential can be explained by the physical properties plotted in Figure 4.5. First of all, since the parameters that controls electrons (h_{0e}, k_e, ξ_e) are not changed, the electron velocity does not change with τ.

Currents are different. From part(c) the current of the $\tau = \zeta$ case is slightly smaller the large-τ case. Recall the equation of current: $J_\phi = n_e\langle v\rangle_{e\phi} - n_i\langle v\rangle_{i\phi}$. In this case, the ion velocity distribution is assumed to be Boltzmann. Thus the value h_{0e} is zero and the ion terms should not affect the final result. The electron density n_e is expressed as $n_e = \exp(\psi)(1 - \Omega_e)$. From part(a) of Figure 4.4, the potential of the small-τ case is always less than the potential of the large-τ case. This difference in potentials causes the difference in currents.

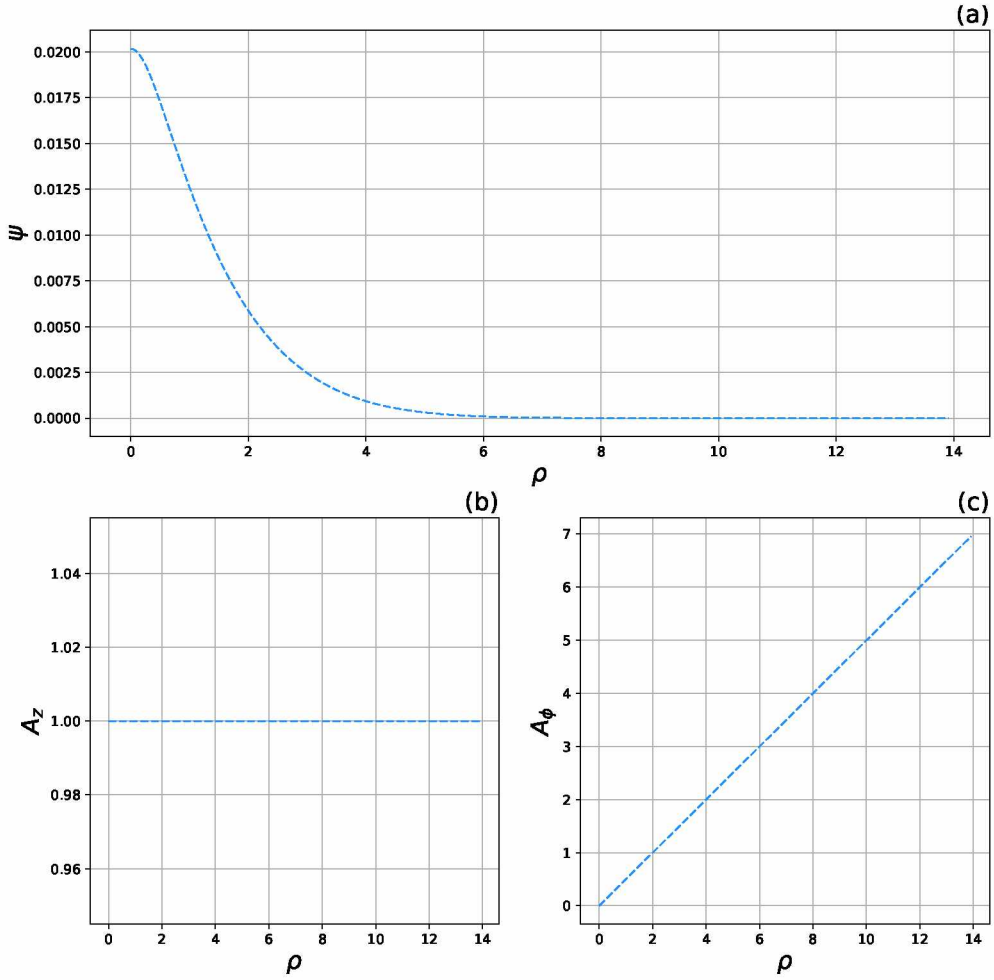

Figure 4.4: Numerical solution of (a) electric potential ψ, (b) $\hat{z}$ component of vector potential A_z, and (c) $\hat{\phi}$ component of vector potential A_ϕ with $h_{0e} = 0.1$, $k_e = 1$, $\xi_e = 0$, $h_{0i} = 0$, $k_i = 0$, $\xi_i = 0$, $\zeta \approx 5.46 \times 10^{-4}$, $\tau = \zeta$, $\beta_e = 10^{-5}$, $B_{z0} = 1$ and $A_{z0} = 1$.

The difference in electric potential could also be explained by number densities of electrons and ions. In the small-τ case, the ion thermal velocity decreases and thereby the ions are affected by the electric potential. As a result, not only the electrons but also the ions are dragged out of the central region. This causes an ion density hole (shown by the blue dashed line in part(b)). The lack of electrons enhances the positive electric potential, yet the lack of ions reduces this effect. Overall the electric potential is still positive, but less than the case where ion effect is neglected.

The physical picture here is clear. Electrons rotates around the center with a certain velocity and maintains an electron density hole in the central region. With the positive electric potential

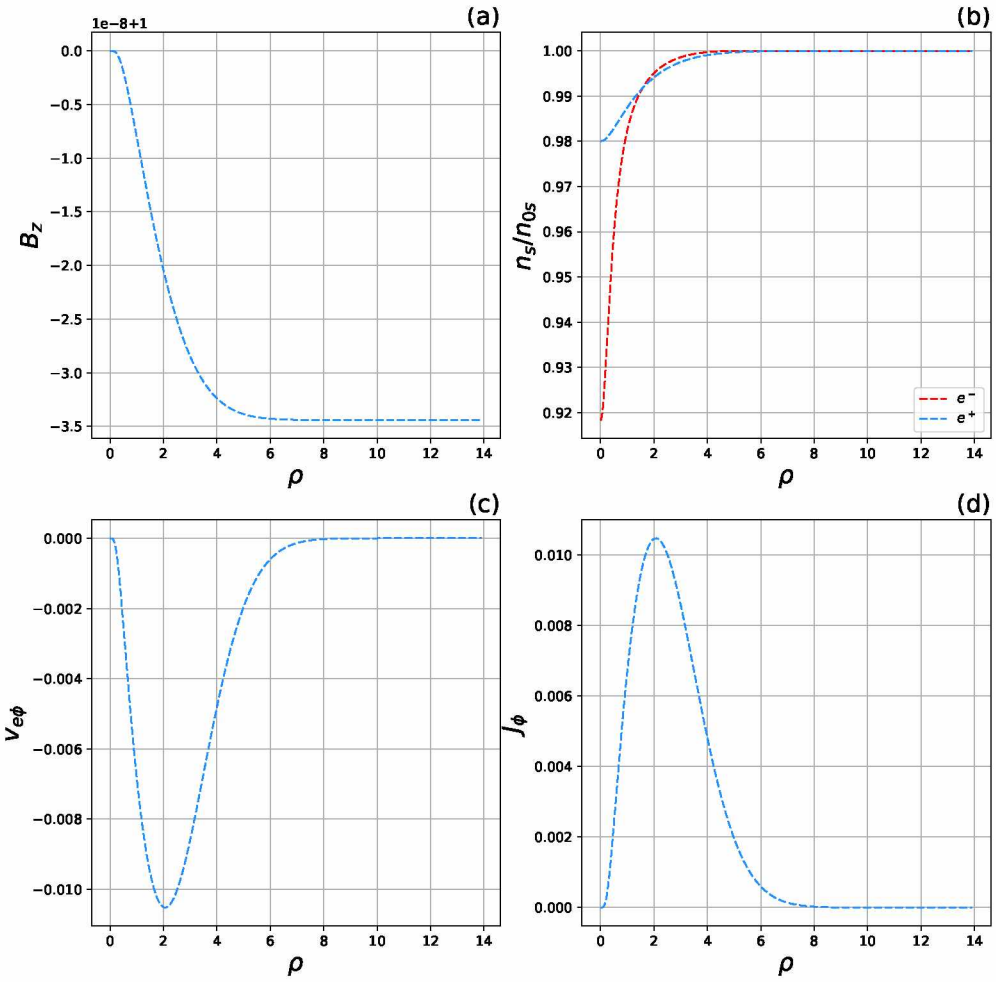

Figure 4.5: Numerical solution of (a) $\hat{z}$-component of magnetic field, (b) density ratio of electrons and ions, (c) $\hat{\phi}$ component of electron velocity, and (d) $\hat{\phi}$ component of current with $h_{0e} = 0.1$, $k_e = 1$, $\xi_e = 0$, $h_{0i} = 0$, $k_i = 0$, $\xi_i = 0$, $\zeta \approx 5.46 \times 10^{-4}$, $\tau = \zeta$, $B_{z0} = 1$ and $A_{z0} = 1$.

produced by lack of the electrons, ions also moves away from the center. As a result, the positive electric potential, the density hole of electrons, and the magnetic hole generated by the rotating electrons are all weakened because of the present of ions.

4.1.3 An electron case with a negative h_{0e}

In the second electron case, the value of h_{0e} is set to be a negative number. As discussed in Chapter 2, when h_{0e} is negative electrons are "put into" the center and roatate around the center in positive directions. The solutions to the system of ODEs are shown in Figure 4.7. This case is comparable with the case shown in Figure 4.1. The only different parameter is h_{0e}. In Figure

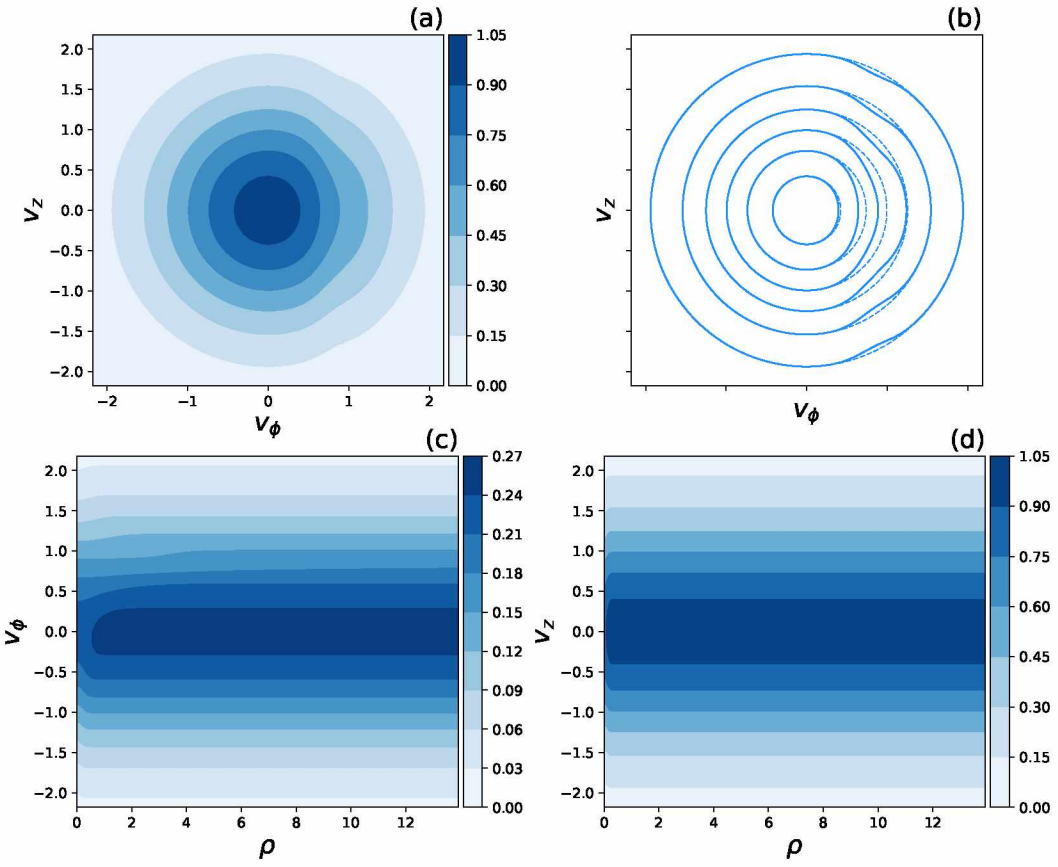

Figure 4.6: (a) Contour plot of the electron distribution function in the v_z-v_ϕ space at $\rho = 2.4$, (b) difference between (a) and the Boltzmann distribution function (represented by dashed lines), (c) contour plot in the v_ϕ-ρ space at $v_z = 2.4$, and (d) contour plot in the v_z-ρ space at $v_\phi = 10$. The color bar indicates the value of electron velocity distribution function.

4.1, $h_{0e} = 0.1$ and in Figure 4.7, $h_{0e} = -0.1$. Since extra electrons are put into the center, the electric potential is negative. The solution of A_z is still a constant. The value of A_ϕ is linear but with a different slope comparing to the case in Figure 4.1. All three solutions matches the asymptotic lines derived in Chapter 2.

Since electrons rotates clockwise, the magnetic field generated through Ampère's Law reduces the original magnetic field. A magnetic "hole" appears and can be easily observed in Figure 4.7(a). An electron density bump occurs in the center. The ions affected by the negative electric potential are gathered and result in an ion density bump but is smaller than the electron bump. These bumps are shown in part (b). The direction of the current generated by the clockwise rotating electrons must be counterclockwise as shown in part (c) and (d).

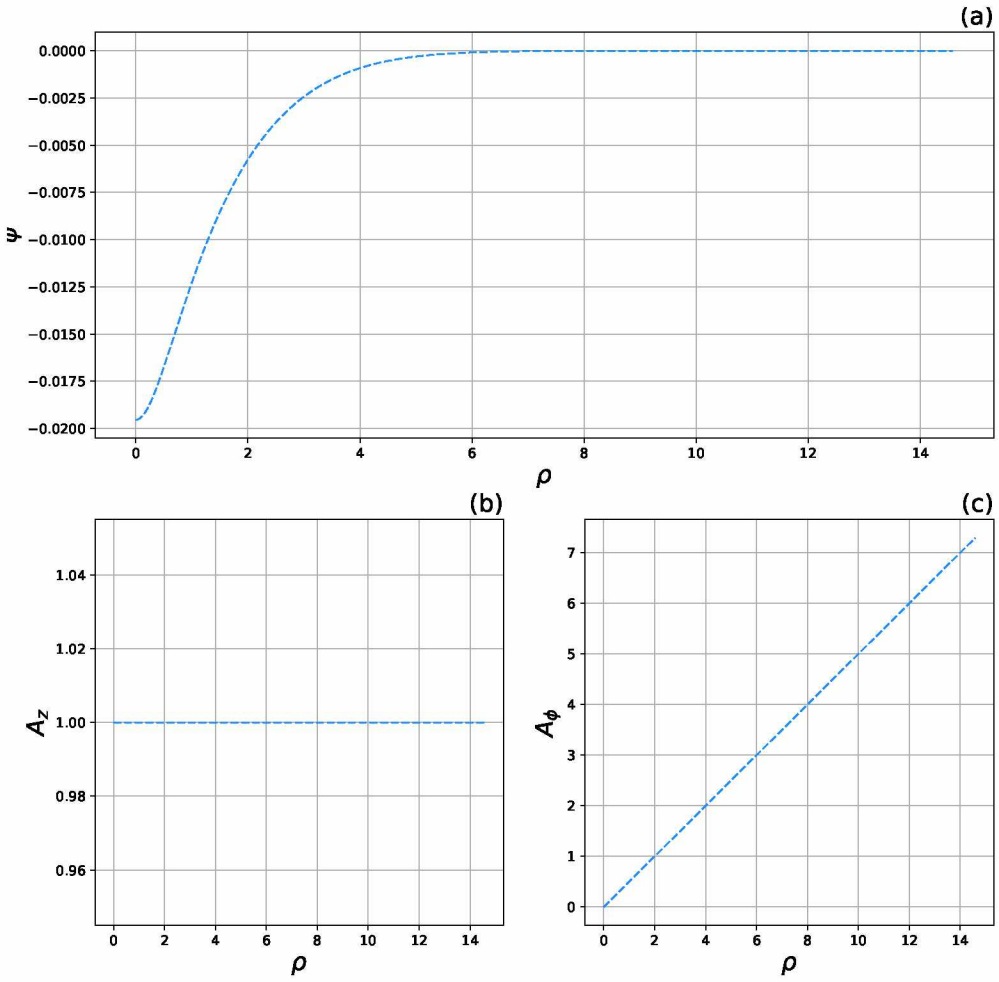

Figure 4.7: Numerical solution of (a) electric potential ψ, (b) $\hat{z}$ component of vector potential A_z, and (c) $\hat{\phi}$ component of vector potential A_ϕ with $h_{0e} = -0.1$, $k_e = 1$, $\xi_e = 0$, $h_{0i} = 0$, $k_i = 0$, $\xi_i = 0$, $\zeta \approx 5.46 \times 10^{-4}$, $\tau = \zeta$, $\beta_e = 10^{-5}$, $B_{z0} = 1$ and $A_{z0} = 1$.

The positive azimuthal flow velocity of electrons can also be seen in the contour plots shown in Figure 4.9. Different from the "shrinking" phenomenon observed in Figure 4.6, the contour lines swells from the Boltzmann contour lines, and that implies more electrons rotates around the center with a positive (clockwise) direction. This is also demonstrated in part (c). The distribution of v_ϕ is tilted to the positive side at approximately $\rho = 2$. These contour plots confirms the physical properties computed in Figure 4.8.

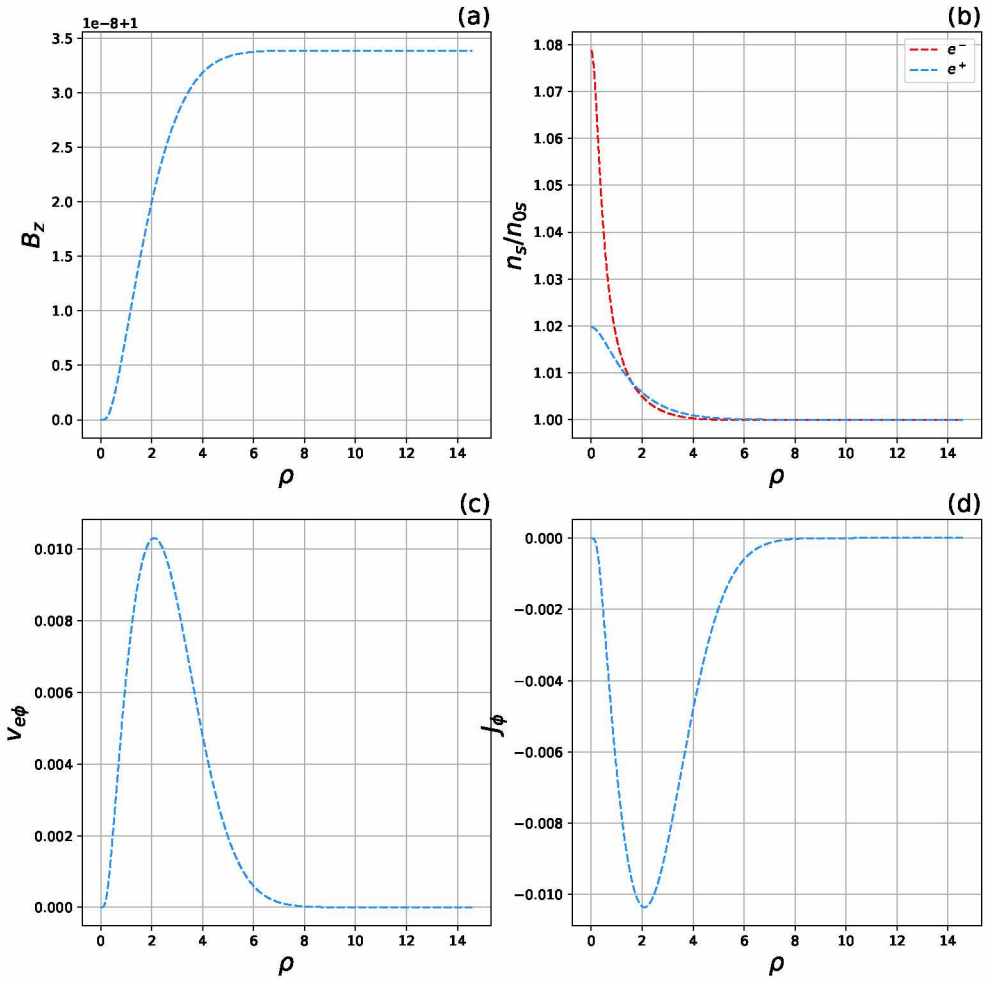

Figure 4.8: Numerical solution of (a) $\hat{z}$-component of magnetic field, (b) Density ratio of electrons and ions, (c) $\hat{\phi}$ component of electron velocity, and (d) $\hat{\phi}$ component of current with $h_{0e} = -0.1$, $k_e = 1$, $\xi_e = 0$, $h_{0i} = 0$, $k_i = 0$, $\xi_i = 0$, $\zeta \approx 5.46 \times 10^{-4}$, $\tau = \zeta$, $B_{z0} = 1$ and $A_{z0} = 1$.

4.1.4 Two parameter scans

Until now, an ideal case, an electron case with a positive h_{0e} and an electron case with a negative h_{0e} are analyzed. The solutions to the equations, physical properties and contour plots of distribution functions are presented. The solution of electric potential varies with different h_{0e} and τ. An intuitive question would be: are there upper or lower limits of τ for the solution of the system of the equations to exist? To answer this question, two parameter scans will be presented in this subsection: a parameter scan with h_{0e} and a parameter scan with τ.

As discussed in Chapter 2, the range of h_{0e} is $0 < h_{0e} < 1$ and $h_{0e} < 0$. The diagram shown in Figure 4.10 shows the change of initial electric potential (ψ_0) with respect to the value

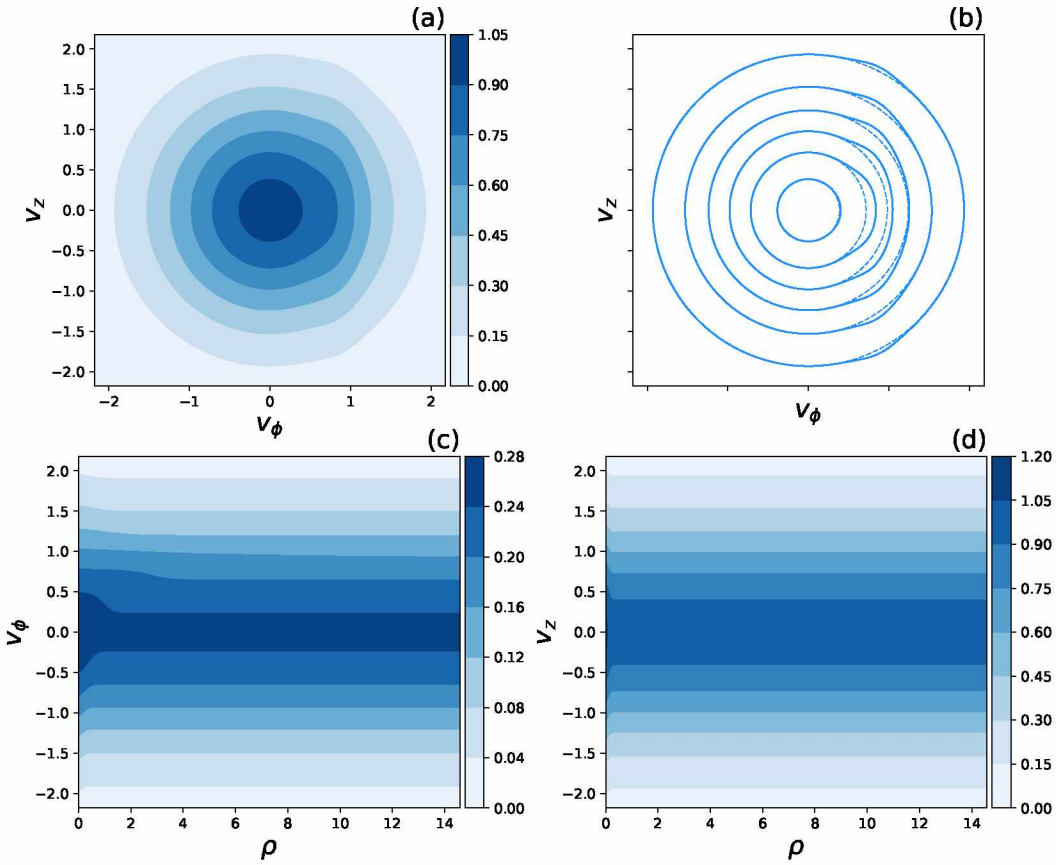

Figure 4.9: (a) Contour plot of the electron distribution function in the v_z-v_ϕ space at $\rho = 2$, (b) difference between (a) and the Boltzmann distribution function (represented by dashed lines), (c) contour plot in the v_ϕ-ρ space , and (d) contour plots in the v_z-ρ space. The color bar indicates the value of electron velocity distribution function.

of h_{0e}. Part(a) indicates the initial value of ψ at different values of h_{0e} and part(b) shows the corresponding ψ vs. ρ diagram. From the diagrams it is not difficult to conclude that as the value of h_{0e} increases the value of initial electric potential (ψ_0) also increase. In other words, ψ_0 and h_{0e} are postively correlated. The reason behind this phenomenon is also obvious. The smaller the value of h_{0e} is, the closer electron velocity distribution is to the Boltzmann distribution. Then there are less electrons "taken out" or "put in" and the corresponding electric potential "bump" or "dent" becomes smaller. However if the value of h_{0e} is larger, there will be more electrons "taken out", or "put in". The corresponding electric potential "bump" or "dent" will be larger as well.

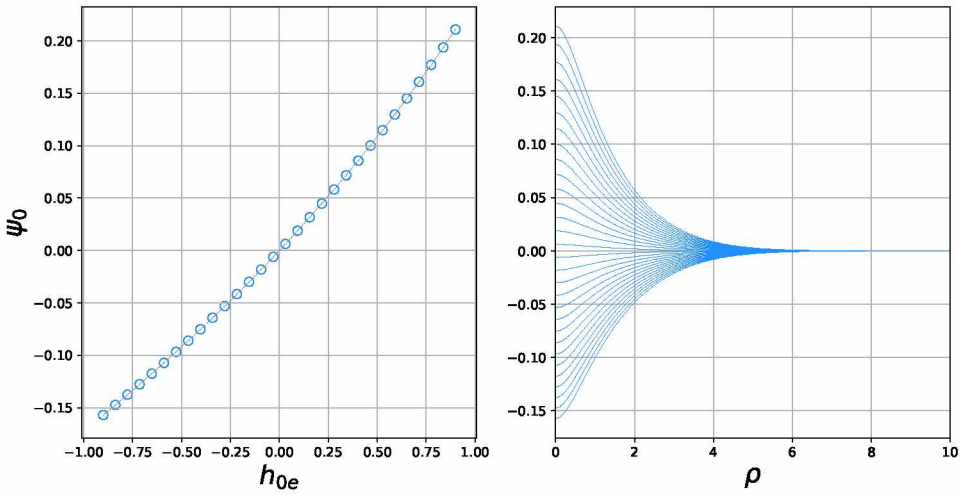

Figure 4.10: A parameter scan of h_{0e}: (a) Initial ψ vs. h_{0e} (plots on the left hand side), and (b) The corresponding solutions of ψ vs. ρ (plots on the right hand side) with $k_e = 1$, $\xi_e = 0$, $h_{0i} = 0$, $k_i = 0$, $\xi_i = 0$, $\zeta \approx 5.46 \times 10^{-4}$, $\tau = \zeta$, $\beta_e = 10^{-5}$, $B_{z0} = 1$ and $A_{z0} = 1$.

The second parameter scan is about the parameter τ. Changing the value of τ and changing the value of h_{0e} has an essential difference. Since τ is defined as $\tau = v_i^2/v_e^2$, changing the value of τ could be done by changing the value of v_i or v_e. If the value of v_e is changed, another parameter β_e, which is defined as $\beta_e = v_e/c$ would also be changed. The cases when h_{0e} is positive is shown in Figure 4.11 and the cases when h_{0e} is negative is shown in Figure 4.12. When h_{0e} is greater than zero, the initial electric potential (ψ_0) is positively related to the value of τ, and when h_{0e} is less than zero, the ψ_0 is negatively related to τ. For both positive$-h_{0e}$ and negative$-h_{0e}$ cases, the value of ψ_0 converges to zero when τ goes to zero, and converges to a constant when τ goes to infinity.

These two phenomena could be explained mathematically and physically. Mathematically the number density of ions can be expressed as

$$n_i \propto \exp\left(-\frac{e\psi}{k_B T_i}\right) = \exp\left(-\frac{2e\psi}{m_i v_i^2}\right). \tag{4.5}$$

Thus when the value of τ is high, ion velocity is relatively large comparing to electron velocity. The term $\frac{2e\psi}{m_i v_i^2}$ goes to zero and the normalized ion number density (n_i) goes to one. The electric potential effect (a "dent" or a "bump") is totally caused by electron velocity distribution. The

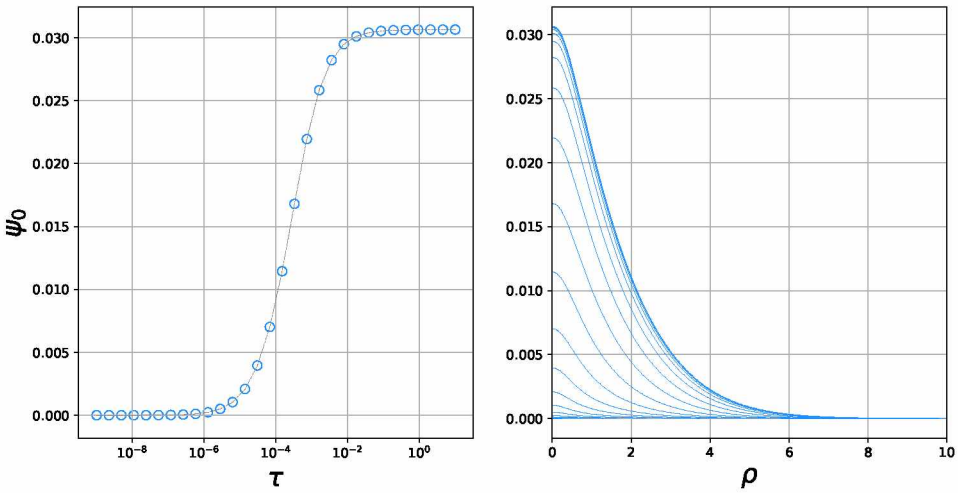

Figure 4.11: A parameter scan of τ when $h_{0e} = 0.1$: (a) The diagram of ψ_0 vs. τ, and (b) The corresponding ψ vs. ρ with $k_e = 1$, $\xi_e = 0$, $h_{0i} = 0$, $k_i = 0$, $\xi_i = 0$, $\zeta \approx 5.46 \times 10^{-4}$, $\beta_e = 10^{-5}$, $B_{z0} = 1$ and $A_{z0} = 1$.

physics behind it is that the high speed ions could be seen as a background and is not affected by the electric potential. Thus if $h_{0e} > 0$, the positive electric potential in the central region is generated purely by taking out electrons, and if $h_{0e} < 0$, the negative electric potential is purely generated by putting in electrons.

When the value of τ is lower, the ion thermal velocity is getting smaller. The electric potential effect (a "dent" or a "bump") is caused by the combined effect of ions and electrons. Physically what happens is if $h_{0e} > 0$ electrons are taken out of the center, the low speed ions are affected by the positive electric potential and move out of the center as well. Thus an electron density dent and a ion density dent both occurs in the center. Finally, the original positive electric potential is weakened and the initial electric potential (ψ_0) is lower than what it was when τ is large. If $h_{0e} < 0$, putting in electrons to the center causes the increase of ion as well. The negative electric potential formed by putting in electrons is weakened. Therefore, the initial electric potential converges to zero when τ goes to zero.

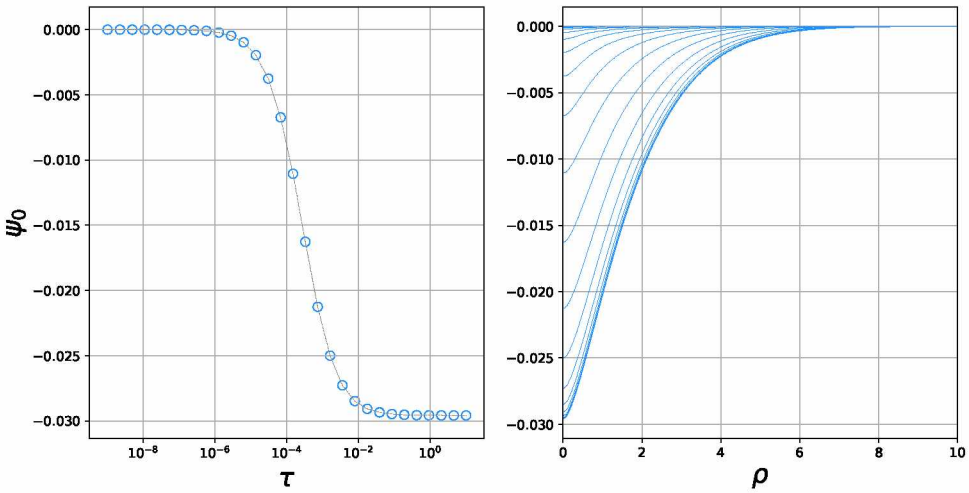

Figure 4.12: A parameter scan of τ when $h_{0e} = -0.1$: (a) The diagram of ψ_0 vs. τ, and (b) The corresponding ψ vs. ρ with $k_e = 1$, $\xi_e = 0$, $h_{0i} = 0$, $k_i = 0$, $\xi_i = 0$, $\zeta \approx 5.46 \times 10^{-4}$, $\beta_e = 10^{-5}$, $B_{z0} = 1$ and $A_{z0} = 1$.

4.2 Ion BGK Mode With Finite Electron Temperature

4.2.1 An ion case with a postive h_{0i}

In the second part of this chapter, the ion cases will be considered. Contrary to the electron BGK mode discussed in the previous sections, in the ion BGK mode the velocity distribution of electrons is set to be Boltzmann. The properties of ions are going to be studied. Following the similar logic, two realistic cases, one with a positive h_{0i} and one with a negative h_{0i} are introduced. For each of them the solutions to the system of equations, the interesting physical properties and the contour plots of the distribution functino in the velocity space will be plotted and analyzed.

What is shown in Figure 4.13 is a solution to the equation system while the value of h_{0e} is set to be zero and the value of $h_{0i} = 0.1$. Contrary to the electron cases discussed in the previous section where electrons are manipulated, we control ions in this case. In this specific case, ions are taken out of the center and background electrons are what remain in there. As a result, a negative potential appears in the center and tends to zero as the radial distance goes to infinity. The value of ξ_i which controls the vertical component of vector potential is set to be zero. Thus the value of A_z remains unchanged. The value of k_i that controls the azimuthal component of

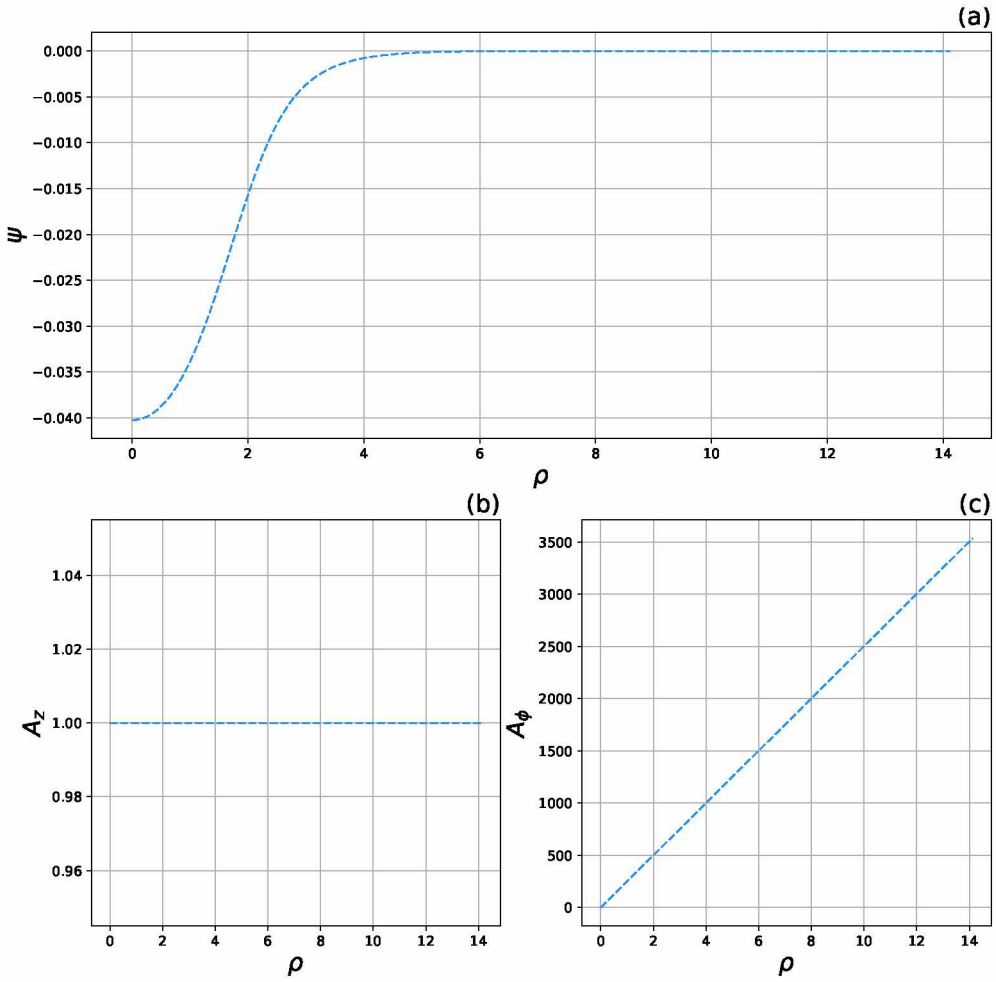

Figure 4.13: Numerical solution of (a) electric potential ψ, (b) $\hat{z}$ component of vector potential A_z, and (c) $\hat{\phi}$ component of vector potential A_ϕ with $h_{0e} = 0$, $k_e = 0$, $\xi_e = 0$, $h_{0i} = 0.1$, $k_i = 1.0$, $\xi_i = 0$, $\zeta \approx 5.46 \times 10^{-4}$, $\tau = \zeta$, $\beta_e = 10^{-5}$, $B_{z0} = 5 \times 10^2$ and $A_{z0} = 1$.

vector potential is set to be constant and thereby the A_ϕ value is positively related to the radial distance.

Figure 4.14 tells us more information about the physical properties of ions. Taking ions out of the center causes an ion "dent" in the center and a non-zero factor of angular momentum k_i drives the azimuthal flow velocity of ions. The majority of ions taken out are located at $\rho < 2.5$. A little further outwards at $\rho \sim 3$, a "bump" can be observed in part(b) of Figure 4.14. The negative electric potential also pushes the electrons in the center to move outward and thereby an electron "dent" appears in the center as well, but with a smaller magnitude.

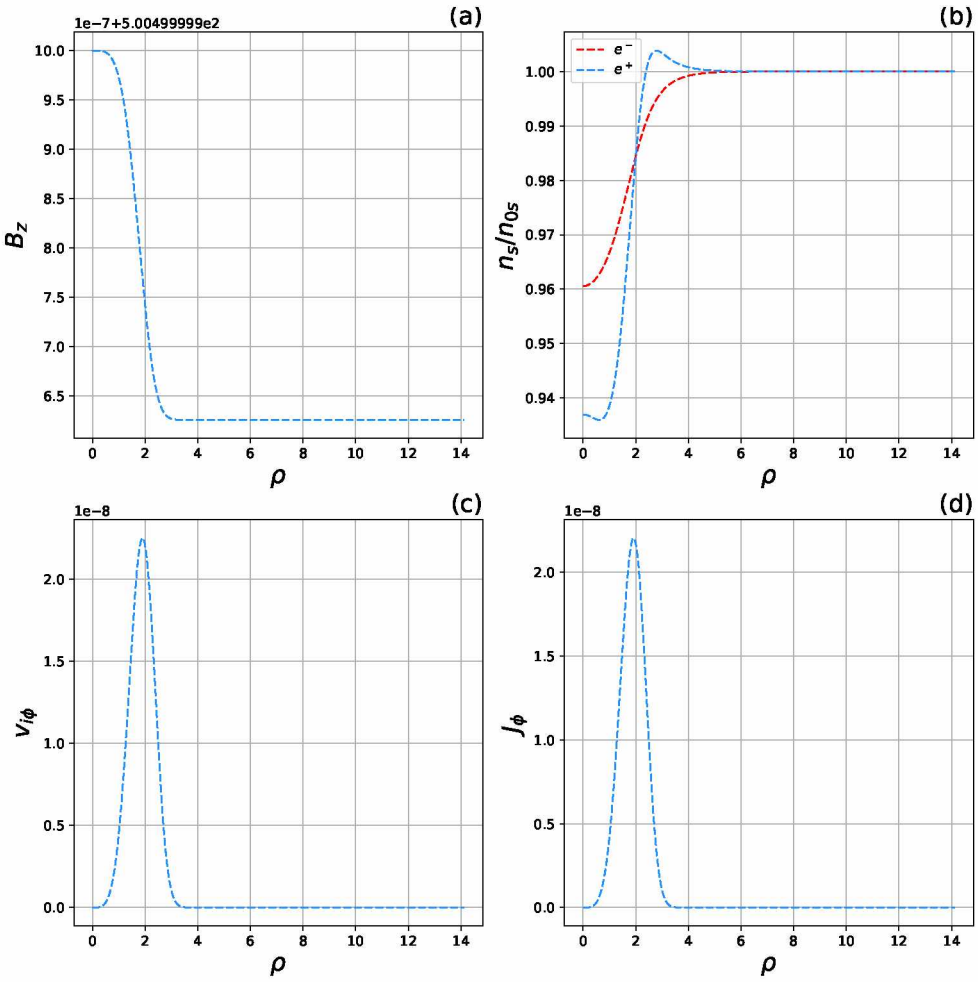

Figure 4.14: Numerical solution of (a) $\hat{z}$-component of magnetic field, (b) density ratio of ions and electrons, (c) $\ddot{\phi}$ component of ion velocity, and (d) $\ddot{\phi}$ component of current with $h_{0e} = 0$, $k_e = 0$, $\xi_e = 0$, $h_{0i} = 0.1$, $k_i = 1.0$, $\xi_i = 0$, $\zeta \approx 5.46 \times 10^{-4}$, $\tau = \zeta$, $\beta_e = 10^{-5}$, $B_{z0} = 5 \times 10^2$ and $A_{z0} = 1$.

Since the electron "dent" is not as deep as the ion "dent", the resulting electric potential is still negative. The rotation of ions can be observed from part (c) of Figure 4.14, and since electrons are not rotating around the center, the current is purely generated by the rotation of the ions. This relationship could be found by comparing Figure 4.14 part (c) and part(d). Finally, the mangetic bump associate with the vector potential A_ϕ is shown in part (a).

Up until now all the scenarios introduced in the ion BGK mode are similar to the explanation in the electron BGK mode. The velocity distribution function of ions, however, is somewhat different. Instead of having a "shrivelled" Boltzmann distribution, as demonstrated in part (b), the whole velocity distribution is shifted to the right. The shift is mainly within smaller

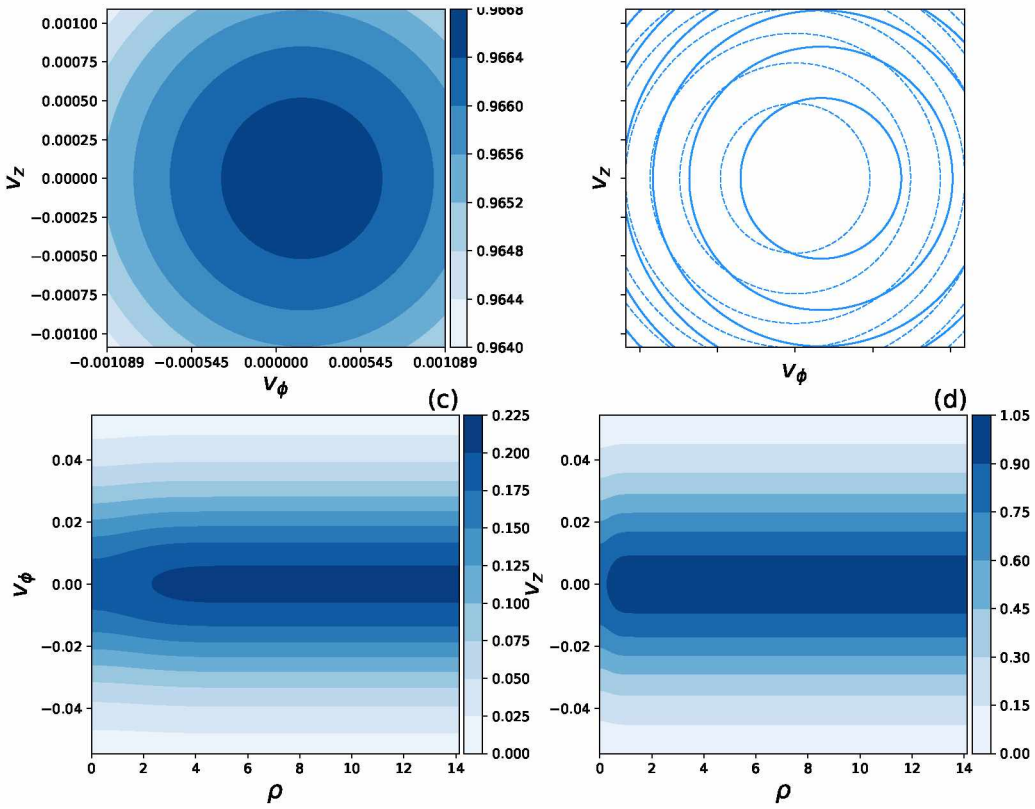

Figure 4.15: (a) Contour plots of v_z vs. v_ϕ at $\rho = 2.7$, (b) difference between (a) and the Boltzmann distribution function (represented by dashed lines), (c) contour plots of v_ϕ vs. ρ, and (d) contour plots of v_z vs. ρ.

normalized velocity so that the contours are plotted in an extremely small scale (part a and b), and is hardly recognizable from a larger scale (part c and d). Since the whole distribution shifts to the right, more ions possess a positive azimuthal velocity and form a local maximum of $v_{i\phi}$ which could be seen in part (c) of Figure 4.15. The peak of $v_{i\phi}$ from Figure 4.14(c) also mathces the location of the "nib" of the darkest blue area in Figure 4.15(c). Notice here the velocity distribution function of ions in this case, and the velocity distribution function discussed in the previous section are barely case studies and they may not possess any universalities. With a different parameter set the solution to the equations, the physical properties and the contour plots of velocity space could be very different.

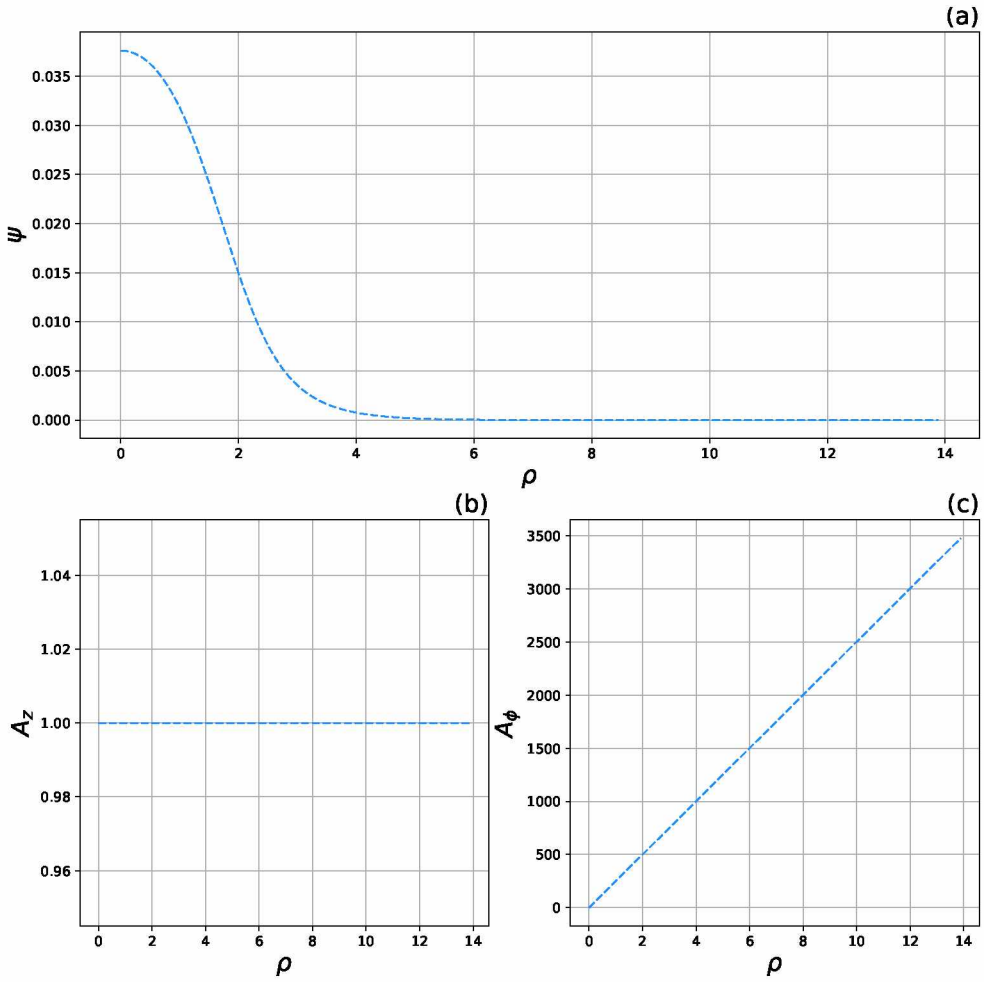

Figure 4.16: Numerical solution of (a) electric potential ψ, (b) $\hat{z}$ component of vector potential A_z, and (c) $\hat{\phi}$ component of vector potential A_ϕ with $h_{0e} = 0$, $k_e = 0$, $\xi_e = 0$, $h_{0i} = -0.1$, $k_i = 1.0$, $\xi_i = 0$, $\zeta \approx 5.46 \times 10^{-4}$, $\tau = \zeta$, $\beta_e = 10^{-5}$, $B_{z0} = 5 \times 10^2$ and $A_{z0} = 1$.

4.2.2 An ion case with a negative h_{0i}

In the case of negative h_{0i}, ions are put into the center. The electric potential in the central area would be positive. Similar to what are discussed in the previous sections, electric potential tends to zero as the radial distance goes to infinity. The $\hat{z}$ component of the vector potential remains unchanged and the $\hat{\phi}$ component of the vector potential is positively related to the radial distance ρ. The solutions are plotted in Figure 4.16.

The important physical properties are plotted in Figure 4.17. Part (a) shows a magnetic field hole caused by the rotation of ions. Part (b) indicates the normalized number density of electrons

and ions. A density bump of ions at the center and a density dent at around $\rho \approx 2$ could be easily observed. Meanwhile an electron bump at the center could also be observed. Part (c) and part (d) plots the azimuthal component of ion bulk velocity and the current density. Since the electron velocity distribution is assumed to Boltzmann, the current density is contributed only by the ion azimuthal velocity.

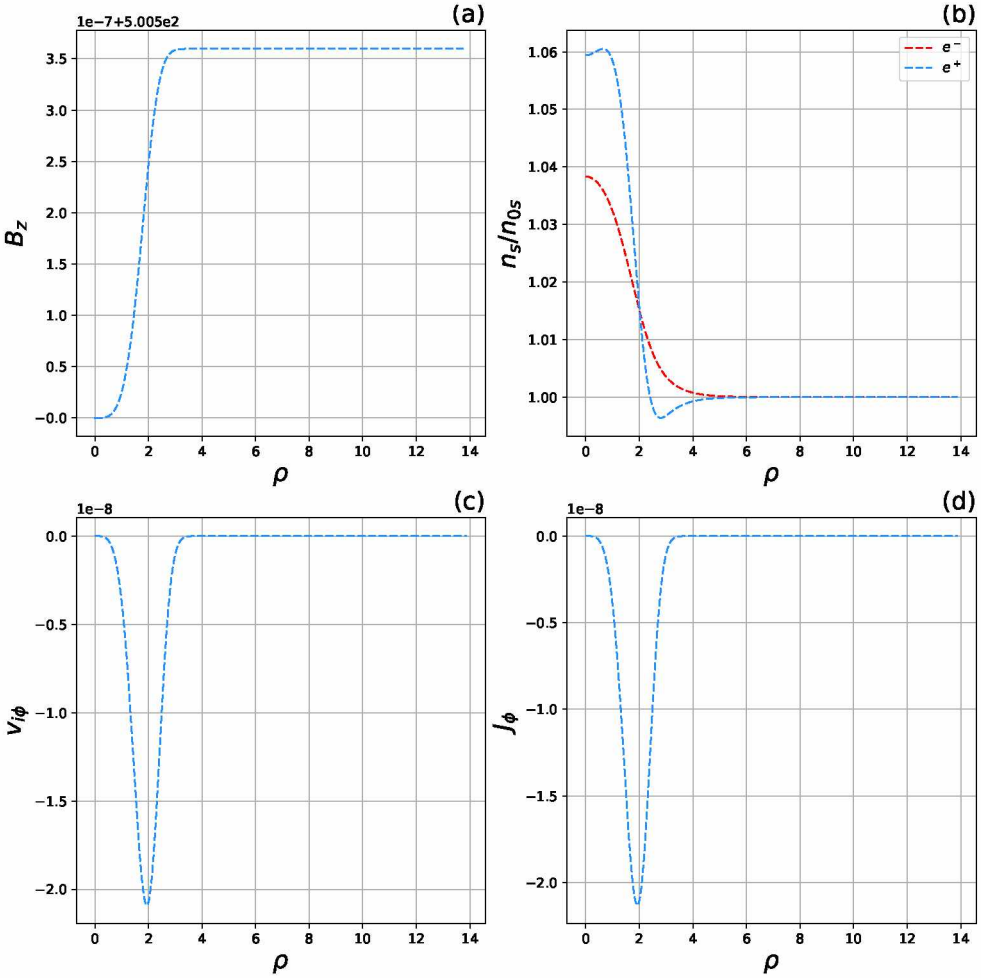

Figure 4.17: Numerical solution of (a) $\hat{z}$ component of magnetic field, (b) density ratio of ions, (c) $\hat{\phi}$ component of ion velocity, and (d) $\hat{\phi}$ component of current with $h_{0e} = 0$, $k_e = 0$, $\xi_e = 0$, $h_{0i} = -0.1$, $k_i = 1.0$, $\xi_i = 0$, $\zeta = 5,4 \times 10^{-4}$, $\tau = \zeta$, $\beta_e = 10^{-5}$, $B_{z0} = 5 \times 10^2$ and $A_{z0} = 1$.

The contour plots of this case are comparable to what we have seen in the previous section. In the positive h_{0i} case, the ion velocity distribution shifts to the right of the Boltzmann distribution. In this case where the h_{0i} is negative, the velocity distribution shifts to the left, causing a negative azimuthal ion bulk velocity. This is consistent with what is shown in Figure 4.17 part(c). The

location of minimum ion azimuthal bulk velocity shown in Figure 4.17 part(c) is also where the darkest blue region shrinks in Figure 4.18 part(c).

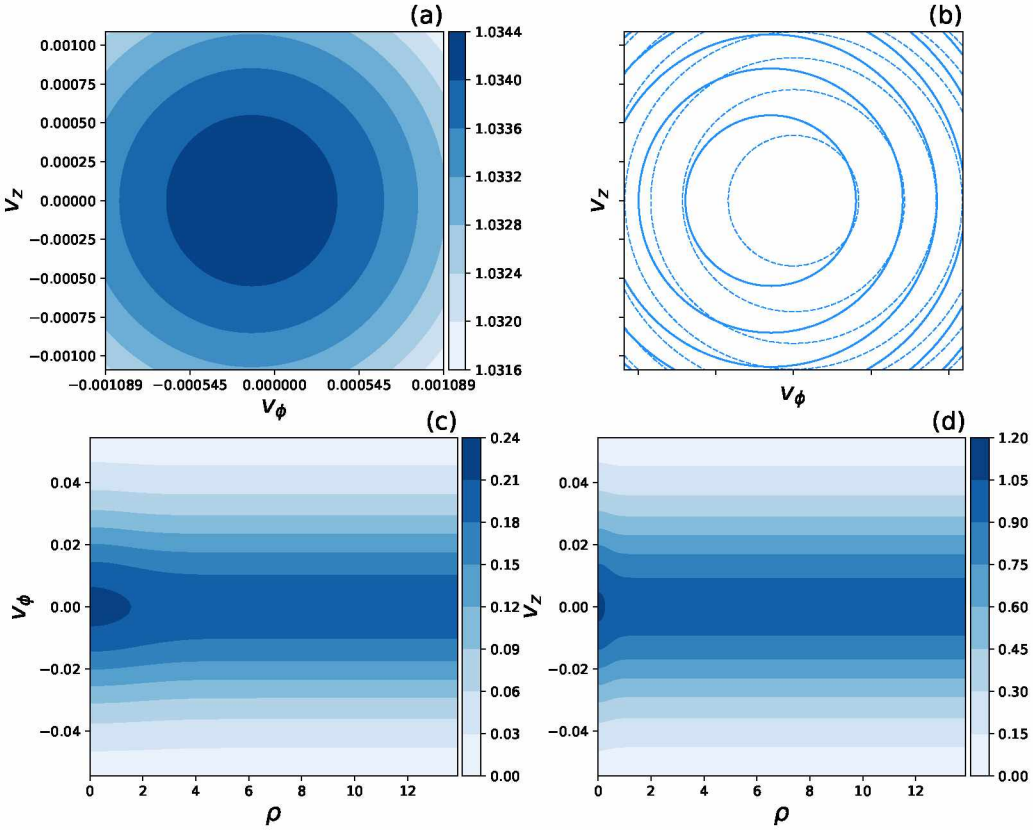

Figure 4.18: (a) Contour plot of the ion distribution function in v_z-v_ϕ space at $\rho = 2$, (b) difference between (a) and the Boltzmann distribution function (represented by dashed lines), (c) contour plot in v_ϕ-ρ space, and (d) contour plot in v_z-ρ space with $h_{0e} = 0$, $k_e = 0$, $\xi_e = 0$, $h_{0i} = -0.1$, $k_i = 1.0$, $\xi_i = 0$, $\zeta = 5{,}4 \times 10^{-4}$, $\tau = \zeta$, $\beta_e = 10^{-5}$, $B_{z0} = 5 \times 10^2$ and $A_{z0} = 1$.

4.2.3 Two parameter scans

Corresponding to the last subsection of 4.1, two parameter scans are going to be plotted in order to demonstrate the relationship between the initial electric potential ψ_0 and the values of h_{0i} and τ. Figure 4.19 indicates the change of initial electric potential with respect to the value of h_{0i}. As the absolute value of h_{0i} becomes closer to zero, the difference between the ion velocity distribution and the Boltzmann distribution is smaller. Accordingly, the electric potential "dent" or "bump" generated is less apparent. Therefore the absolute value of the electric potential $|\psi_0|$

is smaller. In contrast, if the absolute value of h_{0i} becomes larger, the electric potential "dent" or "bump" formed is more intense, and the absolute value of the initial electric potential is greater.

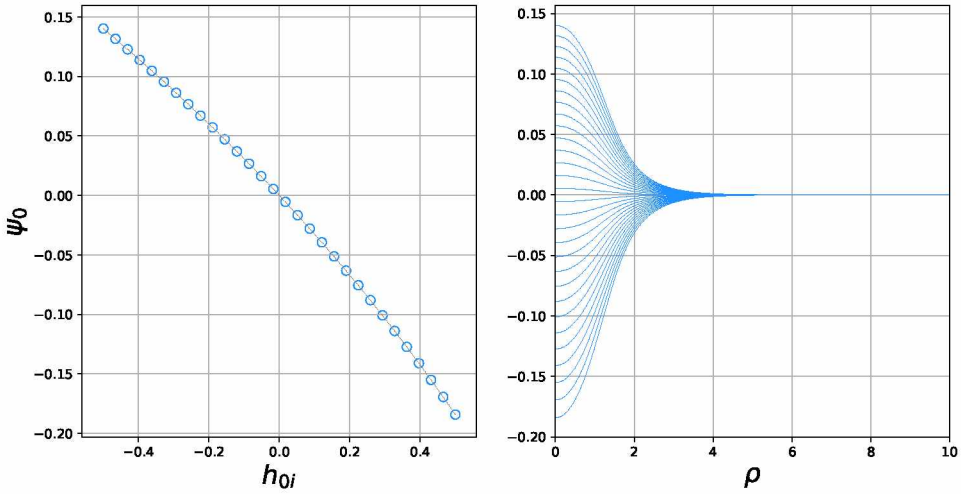

Figure 4.19: A parameter scan of h_{0i}: (a) Initial ψ vs. h_{0i} (plots on the left hand side), and (b) The corresponding solutions of ψ vs. ρ (plots on the right hand side).

The second parameter scan shown in Figure 4.20 and Figure 4.21 focuses on the relationship between the initial electric potential and the value of τ. This plot is comparable with Figure 4.11 and Figure 4.12. When the value of h_{0i} is a negative number, ions are added to the central region and the initial electric potential appears to be positive. When $h_{0i} > 0$, ions are taken out of the center and therefore the initial electric potential is negative. As the absolute value of τ increases, electron velocity decreases. Both ions and electrons are taken out of the cetner, the electric potential effect is then weakened by the electrons. Thus, the initial electric potential tends to zero as τ goes to infinity. When the absolute value of τ decreases, the electron velocity increases and could be seen as a uniform background. The effect caused by electrons is negligible. The electric potential effect is formed purely from taking ions out of the center. The initial electric potential tends to a certain value as τ decreases. These phenomena are shown in part(a) of both Figure 4.20 and Figure 4.21.

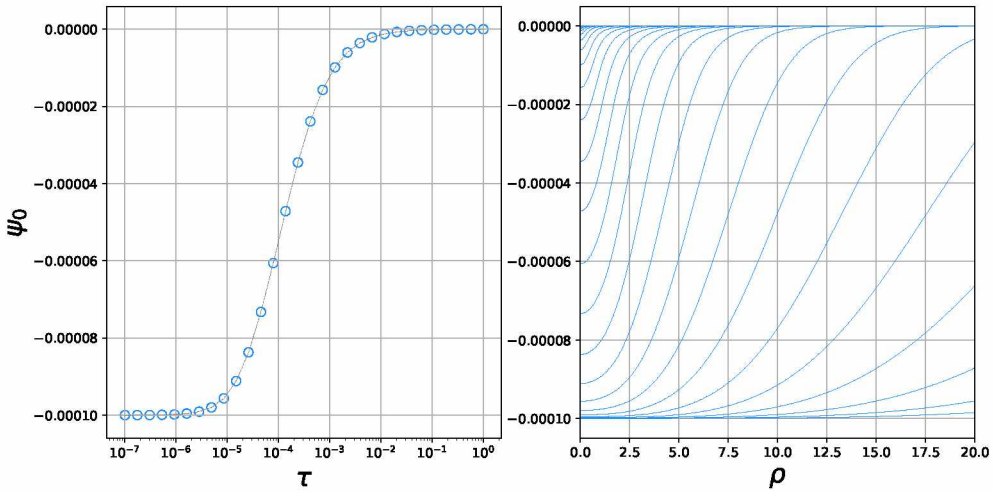

Figure 4.20: A parameter scan of τ when $h_{0i} = 0.1$: (a) The diagram of ψ_0 vs. τ, and (b) The corresponding ψ vs. ρ.

4.3 A Summary to Electron Cases and Ion Cases

Before moving onto more complex cases, let us summarize the four single case studies and the two parameter scans that are discussed in this chapter.

The most apparent phenomenon one can recognize is that if all the other parameters remain unchanged, both electron cases with positive h_{0e} and ion cases with negative h_{0i} can produce positive electric potential in the center, and both electron cases with negative h_{0e} and ion cases with postive h_{0i} can generate negative electric potential. The physical meaning behind it is that "taking away" electrons and "bringing in" ions form similar plsama structures, and "bringing in" electrons and "taking away" ions will have analogous influence on plasmas.

The next important conclusion that can be drawn is about the parameter τ. The four cases discussed so far have one common property: while one of the two types of plasma possesses non-Boltzmann distribution, the other type of plasama treated as a reference is always assumed to be Boltzmann. If the reference particle possesses extremely high velocity, it is barely affected by the electric potential. The corresponding physical effects, for example, the electric potential bump, the magnetic hole, or the number density hole generated through the non-Boltzmann particles are barely affected by the reference plasma and thereby reach their maximum possible values. When the reference particles have lower velocity relative the non-Boltzmann particles, they are

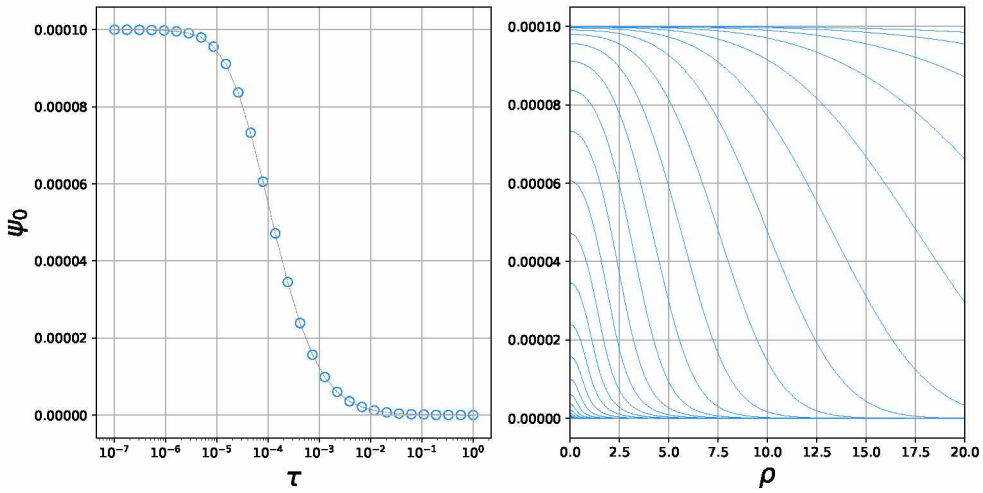

Figure 4.21: A parameter scan of τ by changing the value of v_i when (a) $h_{0i} = -0.1$ and (b) $h_{0i} = 0.1$.

affected by the electric potential and the physical effects created by the non-Boltzmann particles are weakened. As the velocity of the reference particles goes to zero, the physical structures reach their minimal possible values. The significance of this phenomenon is that within the range of τ ($\tau > 0$), the solution to the system of equations always exists.

4.4 Electron-Ion BGK Modes

The topic of this section focuses on the case when both electron and ion thermal velocity possess non-Boltzmann distributions. In the previous sections, the electron cases and ion cases are catogorized by the signs of h_{0e} and h_{0i}. For an electron-ion mode, a similar method of catogorization could be applied. Since both electrons and ions are involved in these cases, the conditions are slightly more complicated. There are totally four different conditions as shown in Figure 4.22: Condition when (1) $h_{0e} > 0$ and $h_{0i} > 0$, (2) $h_{0e} > 0$ and $h_{0i} < 0$, (3) $h_{0e} < 0$ and $h_{0i} > 0$, and (4) $h_{0e} < 0$ and $h_{0i} < 0$.

4.4.1 An electron-ion case when $h_{0e} > 0$ and $h_{0i} > 0$

The solution of the system of equations is shown in the Figure 4.23. Since h_{0e} is greater than zero, electrons are taken out of the central region, and because h_{0i} is also greater than zero, ions

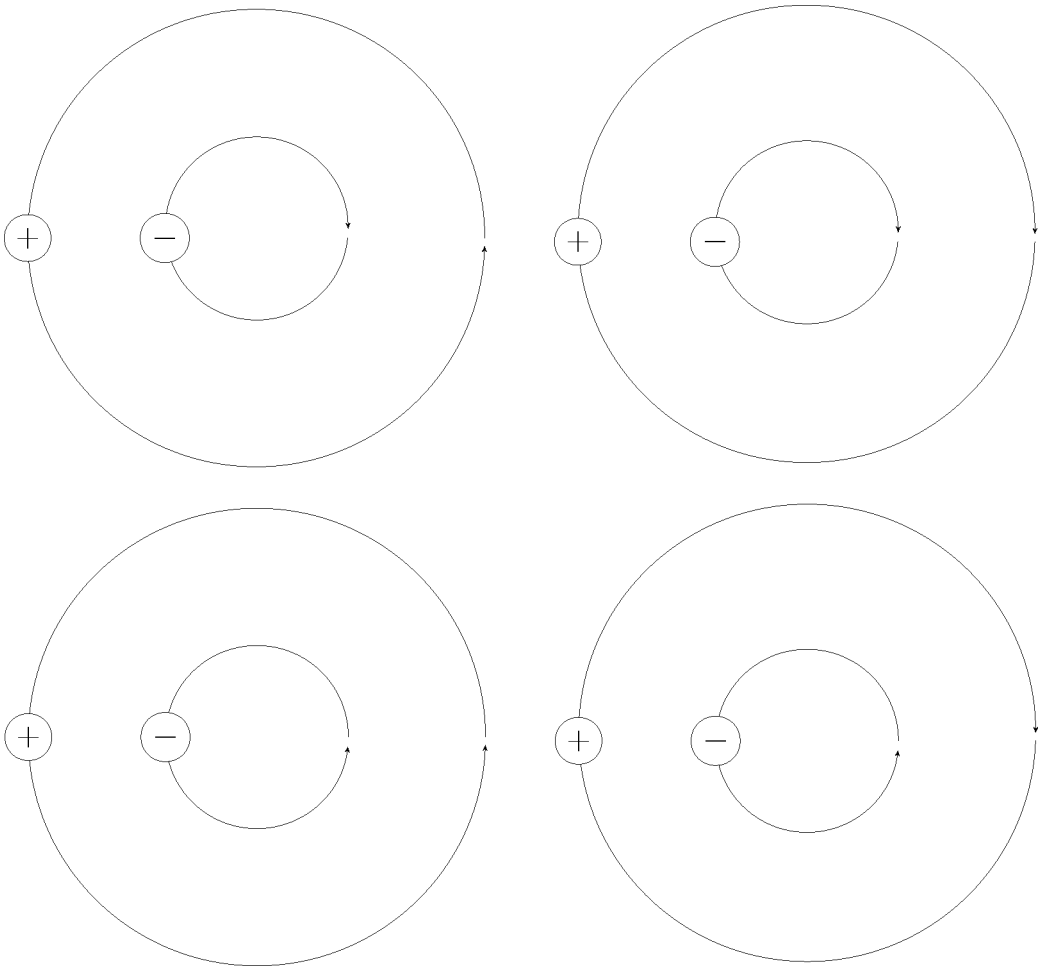

Figure 4.22: Four electron-ion cases discussed in the previous sections:
(a) Upper left diagram: $h_{0e} > 0$ and $h_{0i} > 0$;
(b) Upper right diagram: $h_{0e} > 0$ and $h_{0i} < 0$;
(c) Lower left diagram: $h_{0e} < 0$ and $h_{0i} > 0$;
(d) Lower right diagram: $h_{0e} < 0$ and $h_{0i} < 0$.

are taken out of the central region as well. The net electric potential depends on the type of plasma left in the central region. In this case shown in Figure 4.23, more electrons are taken out of the central region and thereby the net electric potential appears to be postive in the center.

The most significant difference between this electron-ion case and an electron case discussed in the Section 4.1 is that in the electron-ion case there is a potential dent at around $\rho = 2.5$. Clearly, the central region is dominated by the electron distribution function and at $\rho \approx 2.5$ the phenomenon is dominated by the ion distribution function.

Figure 4.24 shows the important physical properties under the same condition. A magnetic "bump" on top of a magnetic "bump" could be observed in part(a). The smaller bump is caused

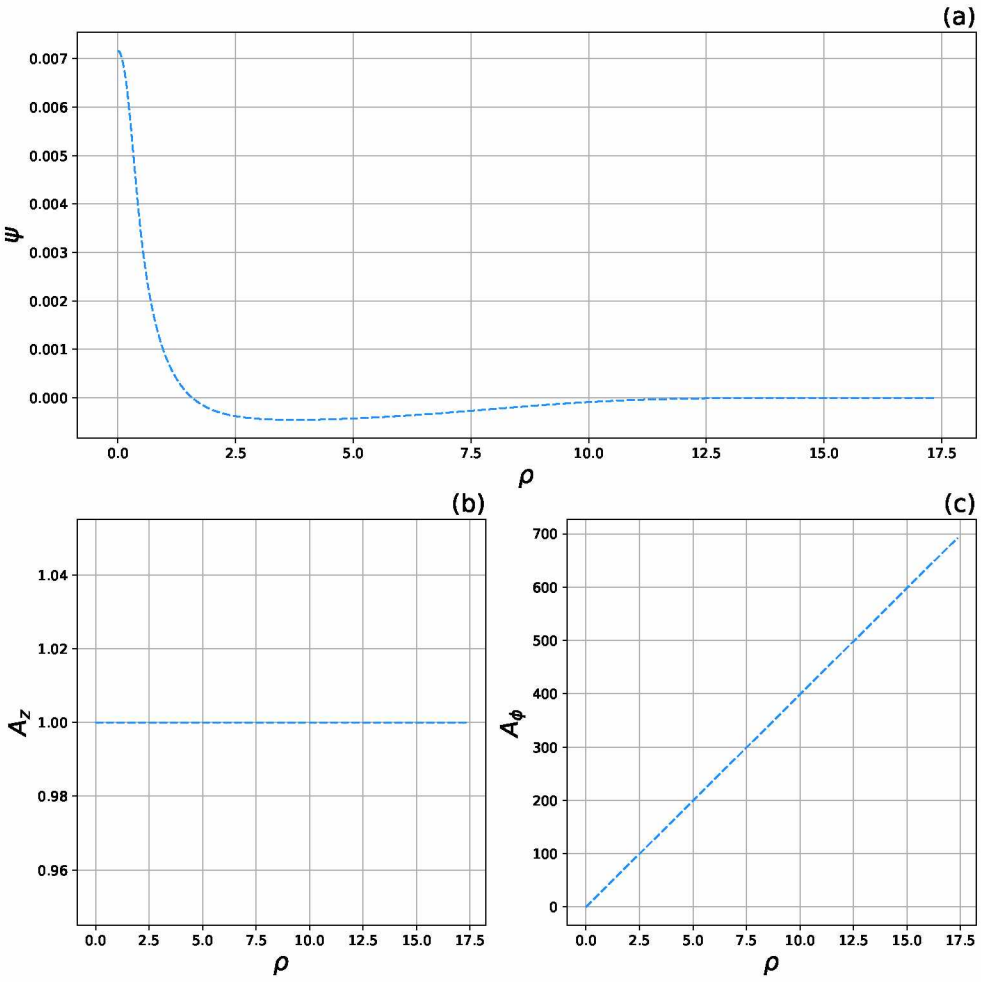

Figure 4.23: Numerical solution of (a) Electric potential ψ, (b) $\hat{z}$-component of vector potential A_z, and (c) $\hat{\phi}$-component of vector potential A_ϕ with $h_{0e} = 1 \times 10^{-1}$, $k_e = 1 \times 10^{-2}$, $\xi_e = 0$, $h_{0i} = 1 \times 10^{-3}$, $k_i = 1 \times 10^{-1}$, $\xi_i = 0$, $B_{z0} = 1$, and $A_{z0} = 1$

by the rotation of electrons at $\rho \approx 0.7$ and larger bump is generated by the rotation of ions at $\rho \approx 8.7$. Since the electrons rotates around the center counterclockwise and the ions rotates around the center clockwise (shown in part(c) and part(d)), both rotations create positive current and both of them cause magnetic bumps.

The case presented in this section is an example of an electron-ion case. From the plots demonstrated, electric potential is apparently affected by both the electrons and the ions. However, since the current created by ions is negligible compared to that of the electrons, the total current is still dominated by the electrons' rotation.

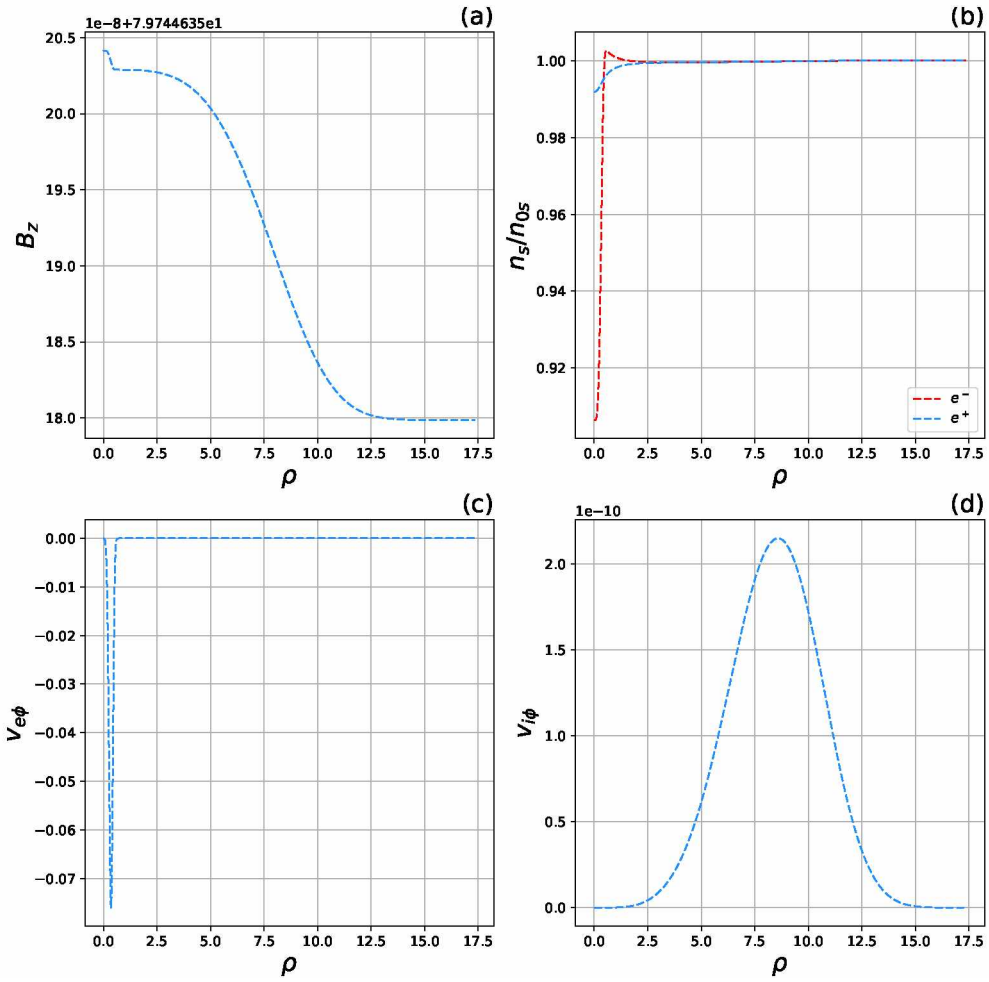

Figure 4.24: Numerical solution of (a) $\hat{z}$-component of magnetic field, (b) density ratio of electrons and ions, (c) $\hat{\phi}$ component of electron velocity, and (d) $\hat{\phi}$ component of current with $h_{0e} = 1 \times 10^{-1}$, $k_e = 1 \times 10^{-2}$, $\xi_e = 0$, $h_{0i} = 1 \times 10^{-3}$, $k_i = 1 \times 10^{-1}$, $\xi_i = 0$, $B_{z0} = 1$, and $A_{z0} = 1$.

4.4.2 An electron-ion case when $h_{0e} > 0$ and $h_{0i} < 0$

The second case we are introducing here is an electron-ion case when $h_{0e} > 0$ and $h_{0i} < 0$. This case corresponds to the scenario that electrons are "taken out of" the center and ions are "put into" the center. Therefore, the electric potential in the central area is enhanced by both electrons and ions. This phenomenon could be observed from part(a) of Figure 4.25.

Since electrons are taken out of the central area, they rotate around the center counter-clockwise, cause a positive current. A magnetic bump should be constructed (shown in Figure 4.26(c)). However, the ions are put into the center. Thus a weak negative current is formed at $\rho \approx 8.5$ (shown in Figure 4.26(d)). The overall magnetic field is a net effect of the two: it is a

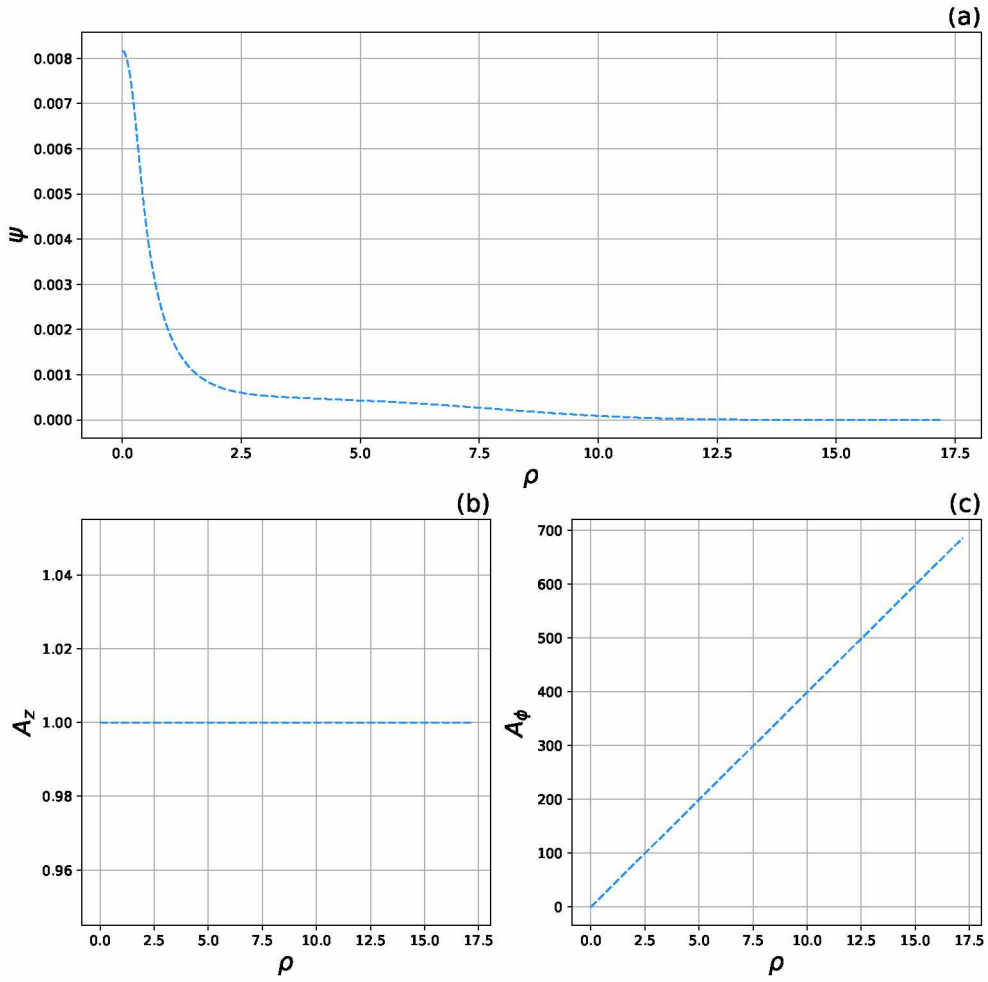

Figure 4.25: Numerical solution of (a) Electric potential ψ, (b) $\hat{z}$-component of vector potential A_z, and (c) $\hat{\phi}$-component of vector potential A_ϕ with $h_{0e} = 1 \times 10^{-1}$, $k_e = 1 \times 10^{-2}$, $\xi_e = 0$, $h_{0i} = -1 \times 10^{-3}$, $k_i = 1 \times 10^{-1}$, $\xi_i = 0$, $B_{z0} = 1$, and $A_{z0} = 1$.

magnetic hole dominated by the ions' rotation with a tiny, hardly seen magnetic "nib" caused by the electrons' rotation.

4.4.3 An electron-ion case when $h_{0e} < 0$ and $h_{0i} > 0$

The third case shown in Figure 4.27 is an "mirror" case to the second one. The electrons are "put into" the central area and the ions are "taken out of" the central area. Together an electric potential hole inside an electric potential hole is fromed and demonstrated in Figure 4.27(a).

Figure 4.28 demonstrates the $\hat{z}$-component of magnetic field, number densities of electrons and ions, and $\hat{\phi}$-component of electron and ion velocity. Contrary to the second case, both

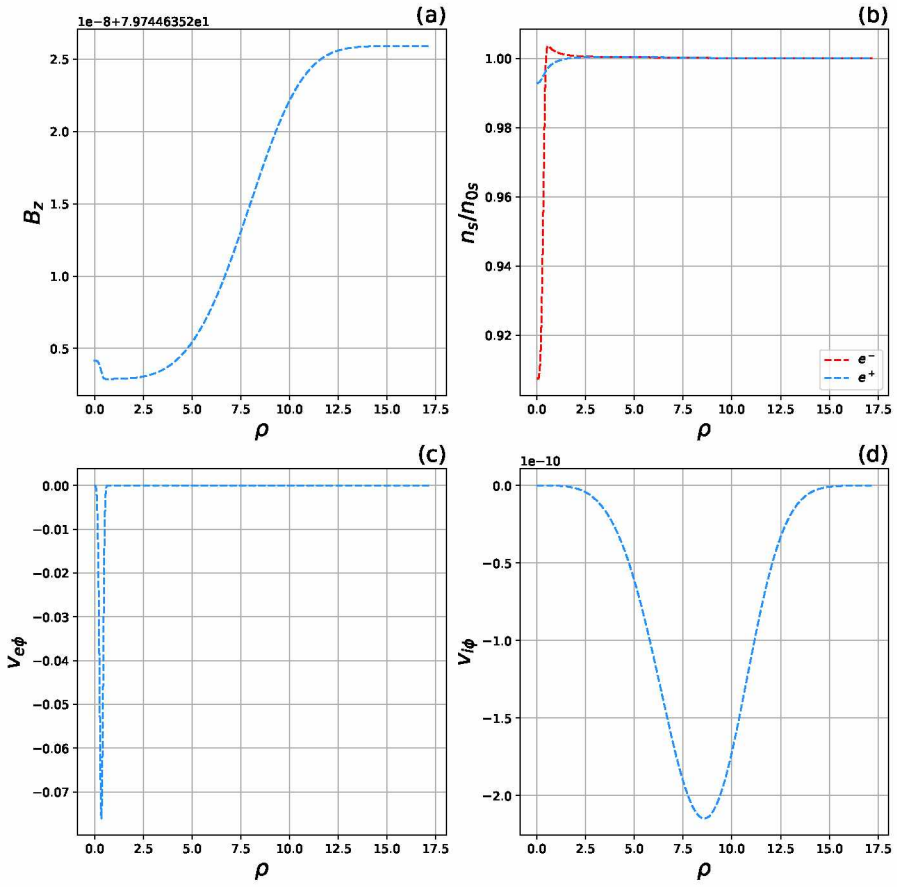

Figure 4.26: Numerical solution of (a) $\hat{z}$-component of magnetic field, (b) density ratio of electrons and ions, (c) $\hat{\phi}$ component of electron velocity, and (d) $\hat{\phi}$ component of current with $h_{0e} = 1 \times 10^{-1}$, $k_e = 1 \times 10^{-2}$, $\xi_e = 0$, $h_{0i} = -1 \times 10^{-3}$, $k_i = 1 \times 10^{-1}$, $\xi_i = 0$, $B_{z0} = 1$, and $A_{z0} = 1$.

electrons and ions rotate around the center clockwise. Therefore an negative current formed near the center and a weak positive current is generated at around $\rho = 10$ (Figure 4.28(c) and Figure 4.28(d)). The magnetic field shown in 4.28(a) indicates a tiny magnetic dent generated through the electrons' rotation on top of a dominating magnetic bump that is formed by the ions' rotation.

4.4.4 An electron-ion case when $h_{0e} < 0$ and $h_{0i} < 0$

The last case presented here is an electron-ion case when $h_{0e} < 0$ and $h_{0i} < 0$. Both electrons and ions are put into the central area. The net effect of electric potential dependes on the dominating particles. In the case plotted in Figure 4.29, more electrons are put into the central

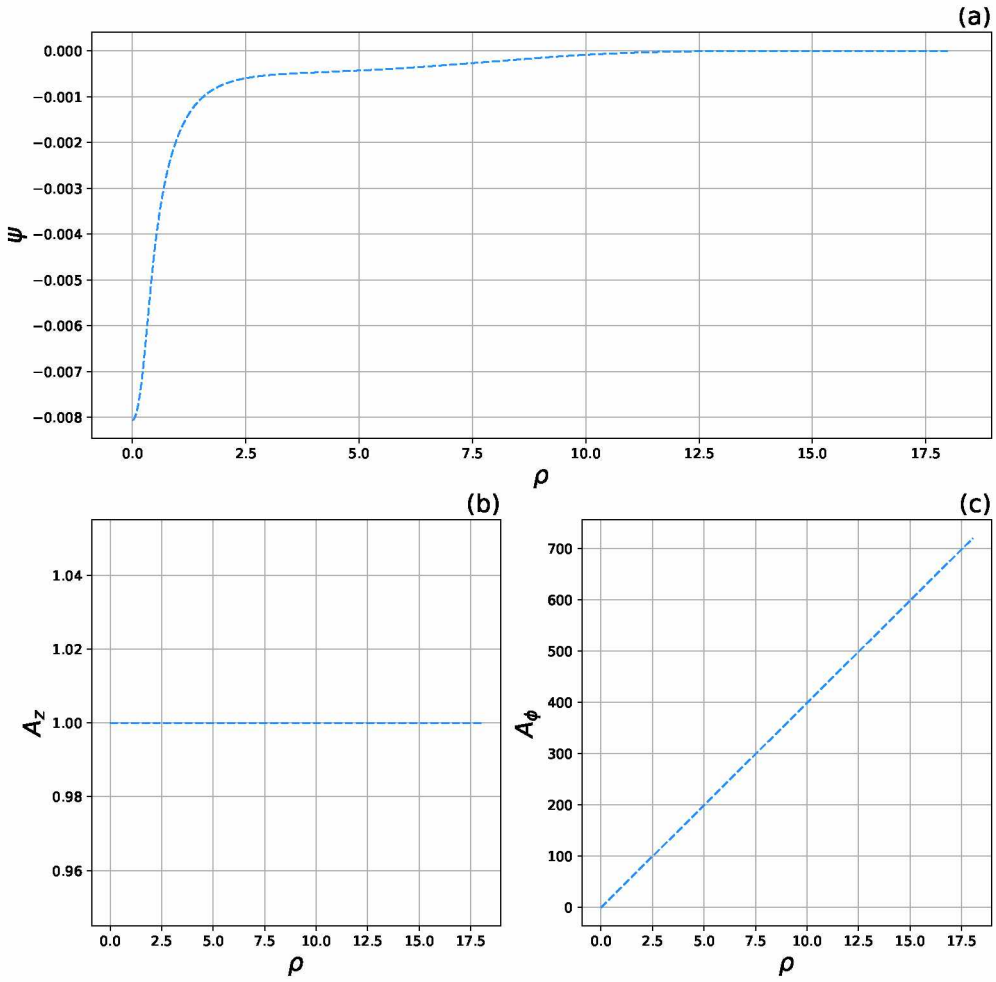

Figure 4.27: Numerical solution of (a) Electric potential ψ, (b) $\hat{z}$-component of vector potential A_z, and (c) $\hat{\phi}$-component of vector potential A_ϕ with $h_{0e} = -1 \times 10^{-1}$, $k_e = 1 \times 10^{-2}$, $\xi_e = 0$, $h_{0i} = 1 \times 10^{-3}$, $k_i = 1 \times 10^{-1}$, $\xi_i = 0$, $B_{z0} = 1$, and $A_{z0} = 1$.

region. Thus the electric potential at the center is negative. The electric potential is dominated by ion effects at $\rho \approx 2.5$ thereby a positive electric potential bump appears from $\rho \approx 2$ to $\rho \approx 12.5$.

The other physical properties are plotted in Figure 4.30. A positive electron velocity shown in Figure 4.30(c) and a negative ion velocity shown in Figure 4.30(d) forms two magnetic holes. Together a magnetic hole inside a magnetic hole is constructed and this phenomenon is plotted in Figure 4.30(a).

The physical pictures of the four cases discussed in this chapter are shown in Figure 4.22. The cases demonstrated here indicate that the numerical method developed in Chapter 3 is

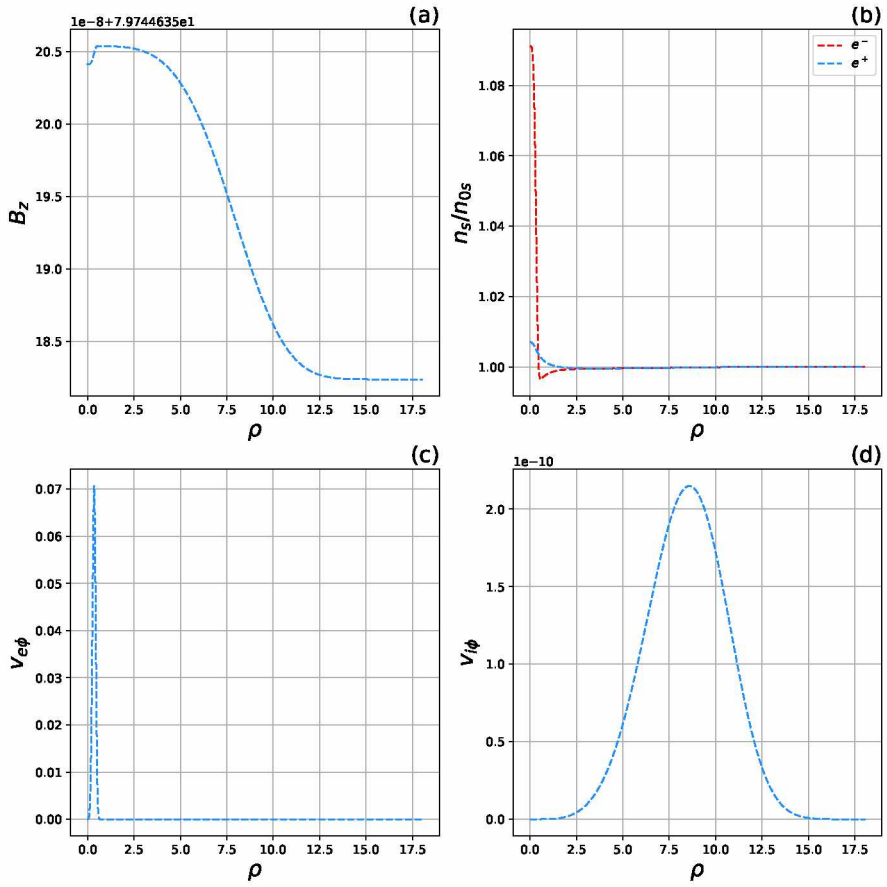

Figure 4.28: Numerical solution of (a) Electric potential ψ, (b) $\hat{z}$-component of vector potential A_z, and (c) $\hat{\phi}$-component of vector potential A_ϕ with $h_{0e} = -1 \times 10^{-1}$, $k_e = 1 \times 10^{-2}$, $\xi_e = 0$, $h_{0i} = 1 \times 10^{-3}$, $k_i = 1 \times 10^{-1}$, $\xi_i = 0$, $B_{z0} = 1$, and $A_{z0} = 1$.

capable of solving electron-ion cases. Although only four cases are selected and demonstrated, some conclusions could be drawn. From the figures plotted, the $\hat{z}$-component of magnetic field (B_z), the net electric potential (ψ) and current density (J) of an electron-ion case seem to have more complicated features, but they can qualitatively be regarded as superpositions of the corresponding electron case and ion case.

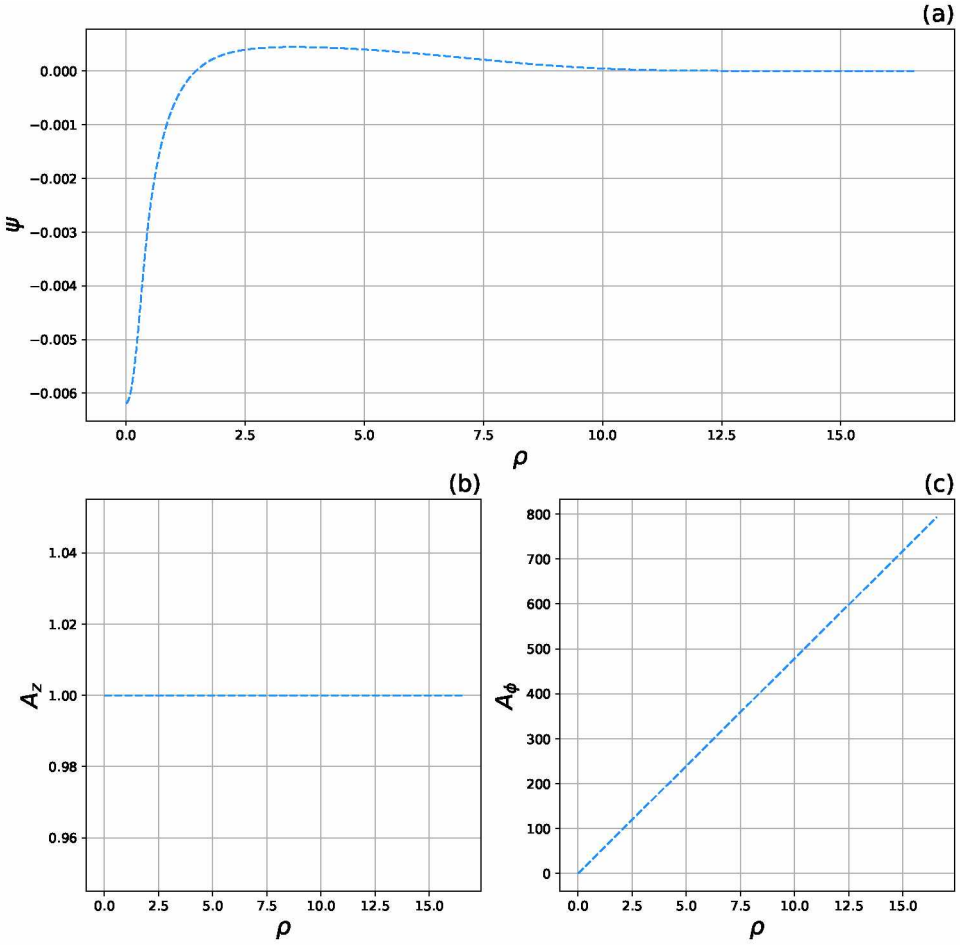

Figure 4.29: Numerical solution of (a) Electric potential ψ, (b) $\hat{z}$-component of vector potential A_z, and (c) $\hat{\phi}$-component of vector potential A_ϕ with $h_{0e} = -1 \times 10^{-1}$, $k_e = 1 \times 10^{-2}$, $\xi_e = 0$, $h_{0i} = -1 \times 10^{-3}$, $k_i = 1 \times 10^{-1}$, $\xi_i = 0$, $B_{z0} = 1$, and $A_{z0} = 1$.

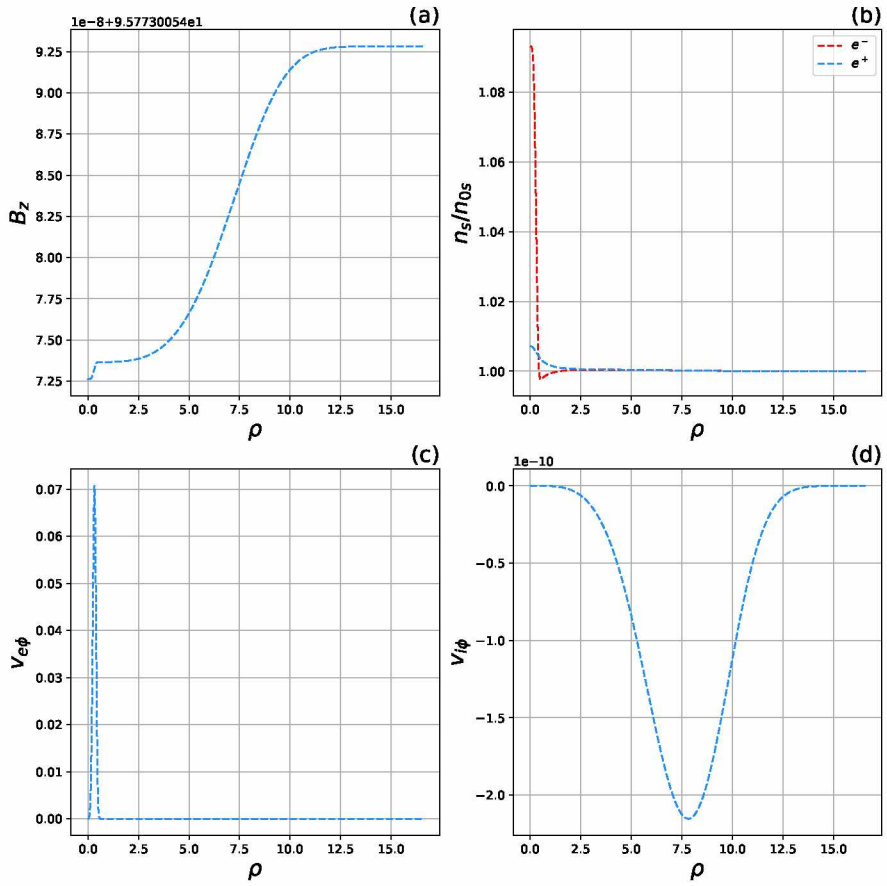

Figure 4.30: Numerical solution of (a) Electric potential ψ, (b) $\hat{z}$-component of vector potential A_z, and (c) $\hat{\phi}$-component of vector potential A_ϕ with $h_{0e} = -.5$, $k_e = 1$, $\xi_e = 0$, $h_{0i} = 0.1$, $k_i = 1$, $\xi_i = 0$.

Chapter 5

Conclusions

This thesis presented explicit construction of two-dimensional Bernstein-Greene-Kruskal modes in a magnetized plasma with kinetic effects from both electrons and ions. Three coupled second-order non-linear differential equations with respect to the electric potential (ψ), the $\hat{z}$-component and $\hat{\phi}$-component of the vector potential (A_z, A_ϕ) are formed by specifying the electron and ion velocity distributions. Both distributions satisfy the Steady-state Vlasov equation depend on the total energy, the $\hat{z}$-component of canonical momentum and angular momentum so that they. Along with the Poisson equation, and Ampère's Law, the Vlasov-Poisson-Ampère system is numerically solved by the BGK-2D simulator. The algorithm of the simulator is based on a shooting method with the set of ordinary differential equations integrated by the adaptive stepsize Runge Kutta method.

The numerical results demonstrated in Chapter 4 answer the two motivations that are brought up in the introduction of this thesis. In a previous study, it is proved that the electron 2D BGK modes exsit with uniform ion density. One situation this assumption is satisfied is when the ion thermal velocity is large. One of the motivations is whether the equation will have a solution when the thermal velocity ratio between ions and electrons is not large. The results in Section 4.1 show that the initial value of the electric potential depends on the choice of the ratio between the sqaure of ion thermal velocity and the electron thermal velocity (τ). As τ goes to positive infinity it tends to a constant value as in the case with a uniform ion density, and when τ approaches zero

it converges to zero. This property of ψ_0 indicates that solutions of the three coupled differential equations always exist no matter what value of τ is chosen. The other motivation asks whether the ions in the 2D ion BGK mode, a mode that the ion velocity distribution is non-Boltzmann and electron velocity distribution is Boltzmann, will behave similar to the electrons in the electron 2D BGK mode. The results in Section 4.2 show properties of the 2D ion BGK modes. Similar to the 2D electron BGK modes, the initial electric potential that depends on τ in an ion BGK mode also tends to a constant when τ goes to zero and zero if τ approaches infinity. Thus, if $\tau \neq 0$ solutions of the ion BGK mode always exist. Besides answering the two motivations mentioned before, four case studies are also presented in the numerical results. The case studies demonstrated in Section 4.3 show that the BGK-2D simulator introduced in Section 2.3 is capable of simulating not only the electron or ion BGK mode, but also the electron-ion BGK modes where both electrons and ions possess non-Boltzmann velocity distributions. The simulation results indicate four electron-ion 2D BGK cases. In these four cases the electric potential (ψ) and the $\hat{z}$-component of the magnetic field (B_z) of the system becomes qualitatively the superposition of ψ and B_z under the electron BGK mode and the ion BGK mode.

This thesis can be expanded in the future. First of all, one of the parameters that controls the $\hat{z}$ component of linear momentum (ξ) is never touched in this thesis. It will cause a non-zero $\hat{\phi}$ component of magnetic field. The properties under such cases require more investigations. Secondly, we can scan the electron-ion BGK modes with different parameters to discover whether the solutions of the 2D BGK always exist. Also, the 2D BGK modes discussed here is non-relativistic and thereby $\beta_e^2 = v_e^2/c^2$ is much less than one. For relativistic cases a modified system of Vlasov-Poisson-Ampère equations is required and the results under such cases are to be investigated.

Bibliography

[Balikhin et al., 2012] Balikhin, M. A., Sibeck, D. G., Runov, A., and Walker, S. N. (2012). Magnetic holes in the vicinity of dipolarization fronts: Mirror or tearing structures? *Journal of Geophysical Research: Space Physics*, 117(A8).

[Bernstein et al., 1957] Bernstein, I. B., Greene, J. M., and Kruskal, M. D. (1957). Exact nonlinear plasma oscillations. *Phys. Rev.*, 108:546–550.

[Cattell et al., 1999] Cattell, C. A., Dombeck, J., Wygant, J. R., Hudson, M. K., Mozer, F. S., Temerin, M. A., Peterson, W. K., Kletzing, C. A., Russell, C. T., and Pfaff, R. F. (1999). Comparisons of polar satellite observations of solitary wave velocities in the plasma sheet boundary and the high altitude cusp to those in the auroral zone. *Geophysical Research Letters*, 26(3):425–428.

[Chen, 2002] Chen, L.-J. (2002). *Bernstein-Greene-Kruskal electron solitary waves in collisionless plasmas*. PhD thesis, UNIVERSITY OF WASHINGTON.

[Chen and Parks, 2002] Chen, L.-J. and Parks, G. K. (2002). Bgk electron solitary waves in 3d magnetized plasma. *Geophysical Research Letters*, 29(9):45–1–45–4.

[Ergun et al., 1998] Ergun, R. E., Carlson, C. W., McFadden, J. P., Mozer, F. S., Muschietti, L., Roth, I., and Strangeway, R. J. (1998). Debye-scale plasma structures associated with magnetic-field-aligned electric fields. *Phys. Rev. Lett.*, 81:826–829.

[Franz et al., 1998] Franz, J. R., Kintner, P. M., and Pickett, J. S. (1998). Polar observations of coherent electric field structures. *Geophysical Research Letters*, 25(8):1277–1280.

[Franz et al., 2005] Franz, J. R., Kintner, P. M., Pickett, J. S., and Chen, L.-J. (2005). Properties of small-amplitude electron phase-space holes observed by polar. *Journal of Geophysical Research: Space Physics*, 110(A9).

[Fu et al., 2012] Fu, H. S., Khotyaintsev, Y. V., Vaivads, A., André, M., Sergeev, V. A., Huang, S. Y., Kronberg, E. A., and Daly, P. W. (2012). Pitch angle distribution of suprathermal electrons behind dipolarization fronts: A statistical overview. *Journal of Geophysical Research: Space Physics*, 117(A12).

[Ge et al., 2011] Ge, Y. S., McFadden, J. P., Raeder, J., Angelopoulos, V., Larson, D., and Constantinescu, O. D. (2011). Case studies of mirror-mode structures observed by themis in the near-earth tail during substorms. *Journal of Geophysical Research: Space Physics*, 116(A1).

[Gershman et al., 2016] Gershman, D. J., Dorelli, J. C., Viñas, A. F., Avanov, L. A., Gliese, U., Barrie, A. C., Coffey, V., Chandler, M., Dickson, C., MacDonald, E. A., Salo, C., Holland, M., Saito, Y., Sauvaud, J.-A., Lavraud, B., Paterson, W. R., Torbert, R., Chen, L.-J., Goodrich, K., Russell, C. T., Strangeway, R. J., Giles, B. L., Pollock, C. J., Moore, T. E., and Burch, J. L. (2016). Electron dynamics in a subproton-gyroscale magnetic hole. *Geophysical Research Letters*, 43(9):4112–4118.

[Goodrich et al., 2016] Goodrich, K. A., Ergun, R. E., Wilder, F. D., Burch, J., Torbert, R., Khotyaintsev, Y., Lindqvist, P.-A., Russell, C., Strangeway, R., Magnes, W., Gershman, D., Giles, B., Nakamura, R., Stawarz, J., Holmes, J., Sturner, A., and Malaspina, D. M. (2016). Mms multipoint electric field observations of small-scale magnetic holes. *Geophysical Research Letters*, 43(12):5953–5959.

[Gurnett and Bhattacharjee, 2017] Gurnett, D. A. and Bhattacharjee, A. (2017). *Introduction to Plasma Physics: With Space, Laboratory and Astrophysical Applications*. Cambridge University Press.

[Hutchinson, 2017] Hutchinson, I. H. (2017). Electron holes in phase space: What they are and why they matter. *Physics of Plasmas*, 24(5):055601.

[Ji et al., 2014] Ji, X.-F., Wang, X.-G., Sun, W.-J., Xiao, C.-J., Shi, Q.-Q., Liu, J., and Pu, Z.-Y. (2014). Emhd theory and observations of electron solitary waves in magnetotail plasmas. *Journal of Geophysical Research: Space Physics*, 119(6):4281–4289.

[Leubner, 2004] Leubner, M. P. (2004). Fundamental issues on kappa-distributions in space plasmas and interplanetary proton distributions. *Physics of Plasmas*, 11(4):1308–1316.

[Livadiotis and McComas, 2009] Livadiotis, G. and McComas, D. J. (2009). Beyond kappa distributions: Exploiting tsallis statistical mechanics in space plasmas. *Journal of Geophysical Research: Space Physics*, 114(A11).

[Ng, 2020] Ng, C. S. (2020). Kinetic flux ropes: Bernstein–greene–kruskal modes for the vlasov–poisson–ampère system. *Physics of Plasmas*, 27(2):022301.

[Ng and Bhattacharjee, 2005] Ng, C. S. and Bhattacharjee, A. (2005). Bernstein-greene-kruskal modes in a three-dimensional plasma. *Phys. Rev. Lett.*, 95:245004.

[Ng et al., 2006] Ng, C. S., Bhattacharjee, A., and Skiff, F. (2006). Weakly collisional landau damping and three-dimensional bernstein-greene-kruskal modes: New results on old problems. *Physics of Plasmas*, 13(5):055903.

[Nicholson, 1983] Nicholson, D. R. (1983). *Introduction to plasma theory*. John Wiley & Sons.

[Oppenheim et al., 1999] Oppenheim, M., Newman, D. L., and Goldman, M. V. (1999). Evolution of electron phase-space holes in a 2d magnetized plasma. *Phys. Rev. Lett.*, 83:2344–2347.

[Press et al., 1992] Press, W. H., Teukolsky, S. A., Vetterling, W. T., and Flannery, B. P. (1992). *Numerical Recipes in C*. Cambridge University Press, Cambridge, USA, second edition.

[Singh, 2000] Singh, N. (2000). Electron holes as a common feature of double-layer-driven plasma waves. *Geophysical Research Letters*, 27(7):927–930.

[Singh et al., 2000] Singh, N., Loo, S. M., Wells, B. E., and Deverapalli, C. (2000). Three-dimensional structure of electron holes driven by an electron beam. *Geophysical Research Letters*, 27(16):2469–2472.

[Sun et al., 2012] Sun, W. J., Shi, Q. Q., Fu, S. Y., Pu, Z. Y., Dunlop, M. W., Walsh, A. P., Zong, Q. G., Xiao, T., Tang, C. L., Reme, H., Carr, C., Lucek, E., and Fazakerley, A. (2012). Cluster and tc-1 observation of magnetic holes in the plasma sheet. *Annales Geophysicae*, 30(3):583–595.

[Sundberg et al., 2015] Sundberg, T., Burgess, D., and Haynes, C. T. (2015). Properties and origin of subproton-scale magnetic holes in the terrestrial plasma sheet. *Journal of Geophysical Research: Space Physics*, 120(4):2600–2615.

[Swanson, 2003] Swanson, D. G. (2003). *Plasma waves*. CRC Press.

[Vasyliunas, 1968] Vasyliunas, V. M. (1968). A survey of low-energy electrons in the evening sector of the magnetosphere with ogo 1 and ogo 3. *Journal of Geophysical Research (1896-1977)*, 73(9):2839–2884.

[Zhima et al., 2015] Zhima, Z., Cao, J., Fu, H., Liu, W., Chen, L., Dunlop, M., Zhang, X. M., and Shen, X. H. (2015). Whistler mode wave generation at the edges of a magnetic dip. *Journal of Geophysical Research: Space Physics*, 120(4):2469–2476.

Appendix Details of Integrations

In the appendix of this thesis we present the details of integration to compute the number density of electrons and ions in 2D BGK-mode. To compute the electron number density, we are going to integrate the following expressions

$$\begin{aligned}
\bar{n}_e &= \int d^3\bar{v}\left[\bar{f}_e\left(\frac{\bar{v}^2}{2} - \bar{\psi}, 2\bar{\rho}(\bar{v}_\phi - \bar{A}_\rho), \bar{v}_z - \bar{A}_z\right)\right] \\
&= \int d^3\bar{v}\left\{\frac{1}{(2\pi)^{3/2}}\exp(-\bar{w}_e)[1 - h_{0e}\exp(-\bar{k}_e\bar{l}_e^2 - \bar{\xi}_e\bar{p}_e^2)]\right\} \\
&= \frac{1}{(2\pi)^{3/2}}\int d^3\bar{v}\exp\left(-\frac{\bar{v}^2}{2} + \bar{\psi}\right)\left\{1 - h_{0e}\exp\left[-\bar{k}_e\left(2\bar{\rho}(\bar{v}_\phi - \bar{A}_\phi)\right)^2 - \bar{\xi}_e\left(\bar{v}_z - \bar{A}_z\right)^2\right]\right\}
\end{aligned} \tag{1}$$

where the first term is a Gaussian integral and it can be integrated through

$$\begin{aligned}
\bar{n}_{e1} &= \frac{1}{(2\pi)^{3/2}}\int d^3\bar{v}\exp\left(-\frac{\bar{v}^2}{2} + \bar{\psi}\right) = \frac{1}{(2\pi)^{3/2}}\int d^3\bar{v}\exp\left(-\frac{v^2}{2}\right)exp\left(\bar{\psi}\right) \\
&= \frac{1}{(2\pi)^{3/2}}exp(\bar{\psi})\int dv_x dv_y dv_z \exp\left(\frac{-\bar{v}_x^2 - \bar{v}_y^2 - \bar{v}_z^2}{2}\right) \\
&= \frac{1}{(2\pi)^{3/2}}exp(\bar{\psi})\left(\sqrt{2}\right)^3\left(\sqrt{\pi}\right)^3 = \exp(\bar{\psi}(\bar{\rho})).
\end{aligned} \tag{2}$$

The second term is a little bit more complicated,

$$\begin{aligned}
\bar{n}_{e2} &= -\frac{1}{(2\pi)^{3/2}} \int d^3v \exp\left(-\frac{\bar{v}^2}{2} + \bar{\psi} \right) \\
&\quad \cdot h_{0e} \exp\left[-\bar{k}_e \Big(2\bar{\rho}(\bar{v}_\phi - \bar{A}_\phi) \Big)^2 - \bar{\xi}_e (\bar{v}_z - \bar{A}_z)^2 \right] \\
&= -\frac{\exp(\bar{\psi}) h_{0e}}{(2\pi)^{3/2}} \int dv_\rho dv_\phi dv_z \exp\left(\frac{-\bar{v}_\rho^2 - \bar{v}_\phi^2 - \bar{v}_z^2}{2} \right) \\
&\quad \cdot \exp\left[-\bar{k}_e \Big(2\bar{\rho}(\bar{v}_\phi - \bar{A}_\phi) \Big)^2 \right] \exp\left[-\bar{\xi}_e (\bar{v}_z - \bar{A}_z)^2 \right] \\
&= -\frac{\exp(\bar{\psi}) h_{0e}}{(2\pi)^{3/2}} \left\{ \int_0^\infty d\bar{v}_\rho \exp\left(-\frac{\bar{v}_\rho^2}{2} \right) \right\} \\
&\quad \cdot \left\{ \int_0^{2\pi} dv_\phi \exp\left(-\frac{\bar{v}_\phi^2}{2} \right) \exp\left[-\bar{k}_e \Big(2\bar{\rho}(\bar{v}_\phi - \bar{A}_\phi(\bar{\rho})) \Big)^2 \right] \right\} \\
&\quad \cdot \left\{ \int_{-\infty}^\infty dv_z \exp\left(-\frac{\bar{v}_z^2}{2} \right) \exp\left[-\bar{\xi}_e (\bar{v}_z - \bar{A}_z)^2 \right] \right\}. \qquad (3)
\end{aligned}$$

The second term contains three integrals. With the identity of integral of exponential functions,

$$\int_{-\infty}^\infty \exp(-ax^2) \exp(-2bx) dx = \sqrt{\frac{\pi}{a}} \exp(b^2/a), \qquad (4)$$

we can compute these three integrals. The first integral is

$$\int_0^\infty d\bar{v}_\rho \exp\left(-\frac{\bar{v}_\rho^2}{2} \right) = \sqrt{2\pi}. \qquad (5)$$

The second integral is

$$\begin{aligned}
&\int_{-\infty}^{\infty} d\bar{v}_z \exp\Big(-\frac{\bar{v}_z^2}{2}\Big)\exp\Big[-\bar{\xi}_e(\bar{v}_z-\bar{A}_z)^2\Big]\\
&=\exp(-\bar{\xi}_e\bar{A}_z^2)\int_{-\infty}^{\infty} d\bar{v}_z \exp\Big[-\Big(\frac{1}{2}+\bar{\xi}_e\Big)\bar{v}_z^2-2(-\bar{\xi}_e\bar{A}_z)\bar{v}_z\Big]\\
&=\sqrt{\frac{2\pi}{1+2\bar{\xi}_e}}\exp\Big[\frac{2\bar{\xi}_e^2\bar{A}_z^2}{1+2\bar{\xi}_e}\Big]\exp\Big[-\bar{\xi}_e\bar{A}_z^2\Big]=\sqrt{\frac{2\pi}{1+2\bar{\xi}_e}}\exp\Big[-\frac{\bar{\xi}_e\bar{A}_z}{1+2\xi_e}\Big].
\end{aligned}\tag{6}$$

And the third integral is

$$\begin{aligned}
&\int_0^{\infty} d\bar{v}_\phi \exp\Big(-\frac{\bar{v}_\phi^2}{2}\Big)\exp\Big[-\bar{k}_e\Big(2\bar{\rho}(\bar{v}_\phi-\bar{A}_\phi(\bar{\rho}))\Big)^2\Big]\\
&=\int_0^{\infty} d\bar{v}_\phi \exp\Big[-\frac{1}{2}\bar{v}_\phi^2-4\bar{k}_e\bar{\rho}^2(\bar{v}_\phi^2+\bar{A}_\phi^2-2\bar{A}_\phi\bar{v}_\phi)\Big]\\
&=\exp(-4\bar{k}_e\bar{\rho}^2\bar{A}_\phi^2)\int_0^{\infty} d\bar{v}_\phi \exp\Big[-\frac{1}{2}\bar{v}_\phi^2-4\bar{k}_e\bar{\rho}^2\bar{v}_\phi^2+2(4\bar{k}_e\bar{\rho}^2\bar{A}_\phi)\bar{v}_\phi\Big]\\
&=\exp(-4\bar{k}_e\bar{\rho}^2\bar{A}_\phi^2)\int_0^{\infty} d\bar{v}_\phi \exp\Big[-\Big(\frac{1}{2}+4\bar{k}_e\bar{\rho}^2\Big)\bar{v}_\phi^2-2(-4\bar{k}_e\bar{\rho}^2\bar{A}_\phi)\bar{v}_\phi\Big]\\
&=\exp(-4\bar{k}_e\bar{\rho}^2\bar{A}_\phi^2)\sqrt{\frac{2\pi}{1+8\bar{k}_e\bar{\rho}^2}}\exp\Big[\frac{32\bar{k}_e^2\bar{\rho}^4\bar{A}_\phi^2}{1+8\bar{k}_e\bar{\rho}^2}\Big]=\sqrt{\frac{2\pi}{1+8\bar{k}_e\bar{\rho}^2}}\exp\Big[-\frac{4\bar{k}_e\bar{\rho}^2\bar{A}_\phi^2}{1+8\bar{k}_e\bar{\rho}^2}\Big].
\end{aligned}\tag{7}$$

Combine all the terms, the dimensionless electron number density is

$$\bar{n}_e=\exp(\bar{\psi}(\bar{\rho}))\Big[1-\frac{h_{0e}}{\sqrt{(1+8\bar{k}_e\bar{\rho}^2)(1+2\bar{\xi}_e)}}\exp\Big(-\frac{4\bar{k}_e\bar{\rho}^2\bar{A}_\phi^2}{1+8\bar{k}_e\bar{\rho}^2}-\frac{\bar{\xi}_e\bar{A}_z^2}{1+2\bar{\xi}_e}\Big)\Big].\tag{8}$$

Similarly, we can compute the dimensionless ion number density. It is

$$\bar{n}_i=\frac{n_i}{n_{0i}}=\exp\Big[-\frac{\zeta\bar{\psi}(\bar{\rho})}{\tau}\Big]\Big[1-\frac{h_{0i}}{\sqrt{(1+8\bar{k}_i\tau\bar{\rho}^2)(1+2\tau\bar{\xi}_i)}}\exp\Big(-\frac{4\bar{k}_i\bar{\rho}^2\zeta^2\bar{A}_\phi^2}{1+8\bar{k}_i\tau\bar{\rho}^2}-\frac{\bar{\xi}_i\zeta^2\bar{A}_z^2}{1+2\bar{\xi}_i\tau}\Big)\Big].\tag{9}$$